

Investigation of Lotsane Earth Fill Dam for Internal Defects Using Time-Lapse Electrical Resistivity Imaging and Frequency Domain Electromagnetic Methods.

By

Bokani Nthaba

Reg. No: 14100116

BSc (Applied Geophysics) (UB)

Earth and Environmental Science Department,

College of Science,

Botswana International University of Science and Technology (BIUST)

nthaba.bokani@studentmail.biust.ac.bw, +267 71630228, +267 74467025

A Thesis Submitted to the College of Science in Partial Fulfillment of the Requirements
for the Award of the Degree of Master of Science in Geology of BIUST

Supervisor(s): Prof. Elisha M. Shemang

Prof. Eliot A. Atekwana

Dr. Ame T. Selepeng

Earth and Environmental Science Department,

College of Science, BIUST

Fax: +267 4900102 Phone Number: (+267 4900117)

Signature: _____ Date: _____

March, 2017

DECLARATION AND COPYRIGHT

I, **Bokani Nthaba**, declare that this thesis is my own original work and that it has not been presented and will not be presented to any other university for a similar or any other degree award.

Signature 

This thesis is copyright material protected under the Berne Convention, the Copyright Act of 1999 and other international and national enactments, in that behalf, on intellectual property. It must not be reproduced by any means, in full or in part, except for short extracts in fair dealing; for researcher private study, critical scholarly review or discourse with an acknowledgement, without the written permission of the office of the Provost, on behalf of both the author and the BIUST.

CERTIFICATION

The undersigned certifies that they have read and hereby recommend for acceptance by the College of Science a thesis titled: *Investigation of Lotsane Earth Fill Dam for Internal Defects Using Time-Lapse Electrical Resistivity Imaging and Frequency Domain Electromagnetic Methods*, in fulfillment of the requirements for the degree of Master of Science in Geology of the BIUST.



Prof Elisha M Shemang
(Supervisor)
Date: March 2017

.....

Dr.
(Co-Supervisor)
Date:.....

.....

Dr.
(Co-Supervisor)
Date:

Acknowledgements

I am very thankful to my family and friends for the support and encouragement because without them I would not have pulled through what appeared to be a difficult passage.

I first met Prof. Elisha Shemang at the University of Botswana in 2010 when he introduced us to geology and then electrical geophysical methods the following year. We then reunited at BIUST in 2014 as his graduate student. The guidance and support he provided throughout my studies are of great value to my academic growth. He has been indeed a great mentor throughout this work and I am very grateful to him for giving me this opportunity.

Valuable contributions and guidance throughout this work have also been received from my co-supervisor, Prof. Eliot Atekwana. He was ever available from the start until the end of this thesis. His constructive criticism improved my work ethic and intellectual capacity, his genuinely passionate interest for research and graduate development is undoubted, and above all, his experience as a reviewer made working with him much easier. I am truly grateful to him.

Dr. Ame Selepeng joined BIUST when at least half the duration of my studies had elapsed, but his contributions to this work since then are priceless. With the experience he has in data acquisition and exploration in general a lot of things got simplified. Modeling failure scenarios had never crossed my mind until he mentioned and assisted me with it. With him it is never time until all the work is done, and his emphasis on the need to work hard could only make me a better person. I am particularly thankful to him.

My colleagues at the Earth and Environmental Science Department offered a lot of support and friendship, the technicians assisted on many occasions with the equipment and other logistics. I am therefore very much indebted to them all. BIUST has been a major financier of this work during its full duration. They provided all the logistics required for data acquisition and processing, hence the success of this work. I am equally grateful to the Department of Water Affairs under the Ministry of Minerals, Energy and Water Resources for granting me permission to conduct a study at Lotsane Dam.

“The failure of a dam is, in general, a complex process which normally begins with some abnormality in behavior (an initial fault) which is not detected. Consequent deterioration, often not observed, and then leads to further damage or even disaster. This is why inspection and monitoring of dams, as well as rapid data analyses and interpretation, can play a critical role in the field of dam safety.”

International Commission on Large Dams, 1987

Abstract

Internal erosion and development of seepage pathways is an ever present concern in earth fill dams, and are a major reason for many dam failures. Internal erosional progresses that are responsible for many dam failures are usually difficult to detect at their onset using the currently in-built monitoring systems that are installed during dam construction. Importantly, increased seepage in dams can only be observed after manifesting at the surface, at which time the integrity of the dam may have already been compromised. Therefore, there is need for improved monitoring in dams using methods that are able to detect defects at an earlier stage. The utility of the electrical resistivity imaging (ERI) and frequency domain electromagnetic (FDEM) methods in characterizing dam embankment conditions has been demonstrated and can be used to elucidate dam defects before they become disasters. Additionally, these methods can be employed on a monitoring basis to study changes that occur in dam embankments across time scales.

In this thesis, the ERI was used in conjunction with the FDEM profiling to investigate and locate possible zones of seepage and internal erosion within the Lotsane Dam. Firstly, data enhancement filters were applied to the aeromagnetic data to enhance shallow subsurface anomalies and highlight geological features such as dykes and faults in the study area. A two dimensional (2D) electrical resistivity profile of 1180 m long was established along the dam embankment and five time-lapse measurements were taken at approximately one and a half months interval over a one year period. The commercially available Geotomo Res2dinv software was used to analyze the resistivity data sets and to produce the pseudo sections. The 2D ERI sections were appraised by forward modeling and synthetic data inversion in order to gain confidence and avoid over/under interpretation of resistivity results. On the basis of interpretation of the resistivity data sets, two major zones were identified. The first is an upper conductive layer varying in thickness from 10 to 25 m with a resistivity range of 26-92 Ωm . Underlying this layer is a more resistive medium of 300-6000 Ωm , interpreted to be rocks of the crystalline basement. Additional to these two layers, there are two conductive zones that cut across the resistivity subsurface model and have been interpreted as fractures. The same anomalous zones were observed in the FDEM profiling data. A fault is also identified in both the resistivity and the aeromagnetic data. From this study it was

concluded that the Lotsane Dam may be at a risk of potential embankment failure due to the identified structural discontinuities, hence further work is needed to monitor the defective zones.

Key words: aeromagnetic method, electrical resistivity, embankment dam, internal erosion, inversion, Lotsane Dam, modeling, seepage, time-lapse.

Table of contents

1 Introduction	15
1.1 Research objective	17
1.2 Research scope	17
1.3 Research significance	18
2 Embankment dams	19
2.1 Earth fill embankment dams	19
2.2 Embankment dam safety	20
2.3 Current understanding of internal erosion and piping	21
2.3.1 How internal erosion develops	23
2.3.2 Parameters related to internal erosion	29
2.4 Examination of dams	29
2.4.1 In-built monitoring	29
2.4.2 Borehole methods	30
2.4.3 Non-destructive testing	30
2.5 Methods used in this study	30
3 Methods	32
3.1 Electrical resistivity imaging (ERI) method	32
3.1.1 Background	32
3.1.2 Theory	33
3.1.3 Resistivity of earth materials	35
3.1.4 Data acquisition	37
3.1.5 Instrumentation	38
3.1.5.1 Multi-electrode and multi-channel systems	39
3.1.6 Field procedure	40
3.1.7 Depth of investigation of multi-electrode resistivity imaging surveys	27
3.1.8 Data processing	42
3.1.8.1 Data quality control and noise	42
3.1.8.2 Pseudo sections	43
3.1.8.3 Inversion and forward modeling	45
3.1.8.3.1 Inversion	47
3.1.8.3.2 Time-lapse inversions	50
3.1.9 Data interpretation	51
3.1.10 2D resistivity modeling	52
3.1.10.1 Embankment dam modeling	55
3.2 Frequency domain electromagnetic (FDEM) method	56

3.2.1	Depth of penetration of EM fields.....	58
3.2.2	EM data inversion.....	58
4	Electrical resistivity imaging on embankment dams	60
4.1	Monitoring and inspection	60
4.2	Previous work	60
4.3	Resistivity variation in embankment dams	61
4.4	Internal erosion and resistivity properties of soils	62
5	Study site.....	65
5.1	Location and physiography.....	65
5.2	General geology of the catchment area.....	65
5.3	Hydrology	66
5.4	Hydrogeology	55
5.5	Description of embankment.....	55
5.5.1	Embankment materials	57
5.5.2	Internal zones of the dam embankment	57
5.5.3	Design and layout of the core zone and filters	58
5.5.4	Lotsane dam instrumentation	59
6	Data and methods.....	61
6.1	Datasets.....	61
6.1.1	Electrical resistivity imaging data	61
6.1.2	Frequency domain EM data acquisition	63
6.1.3	High resolution aeromagnetic data acquisition	64
6.2	Data processing and analysis	66
6.2.1	Resistivity data processing and analysis	66
6.2.1.1	Resistivity data processing.....	66
6.2.1.2	Time-lapse resistivity data inversion	68
6.2.1.3	Resistivity data analysis	74
6.2.1.3.1	Forward modeling.....	74
6.2.2	Frequency domain EM data processing	77
6.2.3	High resolution aeromagnetic data processing.....	88
7	Data interpretation and discussion	91
8	Conclusions and recommendations.....	105
9	References	107
APPENDIX A	120

List of tables

Table 2.1. Brief explanations of some key terms regarding the development of leakage and internal erosion in embankment dams (Modified from Sjö Dahl, 2006).....	9
Table 4.1. Typical ranges of electrical resistivity properties of common embankment dam construction materials based on various publications as referenced in the text.....	57

List of figures

Fig. 2.1: Cross-section of an earth fill embankment dam with a central, slightly inclined core, illustrating the principal zones and some details of the dam design (Adapted from Mori, 2009).	6
Fig. 2.2: Schematics of zones of the dam which are prone to internal erosion including (a) seepage through the embedded conduit in the dam (b) a hole in a pipe, leading to seepage along the walls of the pipe (c) seepage through the embankment (d) a gap between the embankment and the spillway wall, prone to internal erosion and a likely seepage pathway (e) a conduit with collars, with areas in between the collars and the conduit difficult to compact (f) areas below the embedded pipes, where compaction is particularly impossible (Modified from FEMA, 2005; 2008 and Fell et al., 2008).....	8
Fig. 2.3: Ordinary transverse differential settlement cracks across embankment zones (Modified from Mattsson et al., 2008).	11
Fig. 2.4: Longitudinal differential settlement cracks between embankment zones (Modified from Mattsson et al., 2008).	11
Fig. 2.5: Shows what happens when a concentrated leak discharges through the impervious dam core into the downstream filter (Modified from Sherard et al., 1984).....	12
Fig. 2.6: Illustration of internal erosion process by suffusion (Marot et al., 2007).	13
Fig. 2.7: Internal erosion initiated by backward erosion in the embankment (top) and in the foundation (bottom) (Modified from Fell et al., 2008).	14
Fig. 3.1: A piece of resistive material with electrical contacts on opposite ends (Modified from Sakindi, 2012).	20
Fig. 3.2: Resistivity of earth materials (Modified from Loke, 2004).	23
Fig. 3.3: Electrode configurations (a, b and c) commonly used in resistivity surveys and their descriptions using the a-spacing, s-spacing ($n*a$) and the n-factors.....	24
Fig. 3.4: Photographs showing the Iris system, comprising (a) the Syscal Pro switch unit, having the multi-core cable for controlling a set of electrodes connected in a line (b) the top part of the Syscal Pro unit, with the display screen at the center (c) the split-spread resistivity meter- electrodes arrangement, with the Syscal Pro unit at the middle (d) electrodes in the ground, connected to the multi-core cable.	26
Fig. 3.5: Sketch of a multi-electrode data collection system, where the markings on imaging cables indicate electrode positions (Modified from Overmeeren & Ritsema, 1988, as cited in Dahlin, 2001).	27
Fig. 3.6: Schematic showing how a pseudo section in a dipole-dipole array is constructed	30

Fig. 3.7: An example of a field data set with some bad data points (a) the apparent resistivity data in pseudosection form and (b) in profile form.....	31
Fig. 3.8: Schematic showing a flow chart of geophysical data inversion and forward modeling process, where the collected data (d) and the model (m) of a physical property are related by a mathematical function (G) (Modified from Pierce et al., 2012).....	32
Fig. 3.9: Schematic of a subsurface model divided in a number of cells.....	39
Fig. 3.10. Schematic diagram of the finite-difference or finite-element mesh used by the Res2dmod program (Adapted from Loke, 2002).	40
Fig. 3.11: A schematic diagram of Frequency Domain EM method (Grant & West, 1965, as cited in Reynolds, 2011).....	43
Fig. 5.1: A map showing the topography and the Lotsane embankment dam and settlement areas proximal to the dam (Modified from SMEC et al., 2012).	53
Fig. 5.2: The generalized geology of the Lotsane catchment based on Republic of Botswana Hydrogeological Reconnaissance map sheet 8 (Modified from SMEC et al., 2012).	54
Fig. 5.3: Crest settlement points on the downstream side of the dam embankment installed at 100 m intervals.	56
Fig. 5.4: A schematic of the cross section at chainage 1550 m (Fig. 5.3) and the general arrangement of the dam embankment zones, with a vertical upstream side of the slope and a slightly inclined downstream side (Modified from SMEC et al., 2012).	58
Fig. 5.5: Photographs of Lotsane Dam showing instrumentation installed during its construction for long term monitoring of the dam conditions: (a) reservoir level gauge installed for reservoir water level monitoring and can be read from the dam crest using a pair of binoculars, (b) survey monitoring point located at the downstream edge of the embankment, (c) location of the seepage weir in a concrete pit, (d) view of standpipe piezometers located at the downstream toe of the dam, (e) vibrating wire (VW) piezometers, (f) seepage pipe to monitor the flow rate and evidence of particle (soil) migration, (g) the dam embankment and the parapet wall, (h) view of the concrete pit where the V-Notch seepage weir is located and (i) the compartment in the seepage weir where the accumulation of fines are being monitored.	60
Fig. 6.1: Photographs showing a 2D resistivity data acquisition setup with 48 stainless steel electrodes planted into the ground (Lotsane Dam embankment) along a straight line, attached to a multi-core cable.	61
Fig. 6.2: Schematics showing an arrangement of the two segments and the station positions in multi-electrode resistivity measurements for a simple (standard) configuration (left) and a roll- along configuration (right) (Modified from Bernard et al., 2006).	62

Fig. 6.3: Photos showing the frequency domain electromagnetic equipment set: the Promis IP system consisting of (a) the transmitter loop/coil (b) the receiver console plus the sensor (c) the reference cable or the Tx-Rx link. r..... 63

Fig. 6.4: The total magnetic intensity (TMI) distribution map of Lotsane Dam area..... 65

Fig. 6.5: The subsurface resistivity inversion results of the field data, showing the measured and the calculated pseudo sections plus the resistivity inverse model, with an absolute error of 7.7 %.. 67

Fig. 6.6: (a) An inverse resistivity model from the initial dataset, acquired on the 27th October 2015 (b) the inverse resistivity model from the second dataset acquired on the 15th December 2015 (c) the difference model from the two datasets, showing the percentage change in model resistivity sections with an absolute error of 8.6%..... 69

Fig. 6.7: (a) Inverse resistivity model second dataset, acquired on the 15th December 2015, (b) the inverse resistivity model of the third dataset, acquired on the 5th March 2016, (c) the percentage change in model resistivity sections with an absolute error of 8.1 %.. 70

Fig. 6.8: (a) Inverse resistivity model third dataset, acquired on the 5th March 2016, (b) the inverse resistivity model of the fourth dataset, acquired on the 25th May 2016, (c) the percentage change in model resistivity sections with an absolute error of 8.5 %..... 71

Fig. 6.9: (a) Inverse resistivity model of the fourth dataset, acquired on the 25th May 2016, (b) the inverse resistivity model of the fifth dataset, acquired on the 19th August 2016, (c) the percentage change in model resistivity sections with an absolute error of 10.4 %.. 72

Fig. 6.10: (a) Inverse resistivity model of the fourth dataset, acquired on the 25th May 2016, (b) the inverse resistivity model of the fifth dataset, acquired on the 19th August 2016, (c) the percentage change in model resistivity sections with an absolute error of 12.3 %.. 73

Fig. 6.11: Forward model of the dam embankment. This model is made up of three layers of varying thicknesses and resistivity.. 74

Fig. 6.12: Image of (a) the forward model of the idealized subsurface condition, (b) the measured apparent resistivity pseudosection, (c) the calculated apparent resistivity pseudosection, and (d) the inverse model resistivity section..... 76

Fig. 6.13: (a) Profiles of the measured in-phase/real (solid black), computed in-phase (dotted black), measured quadrature/ imaginary (solid red) and the computed quadrature (dotted red) components of the secondary electromagnetic field expressed as percentage of the primary electromagnetic field (b) a two layered model showing resistivity distribution to a depth 60 m..... 78

Fig. 6.14: (a) Profiles of the measured in-phase/real (solid black), computed in-phase (dotted black), measured quadrature/ imaginary (solid red) and the computed quadrature (dotted red) components of the secondary electromagnetic field expressed as percentage of the primary electromagnetic field (b) a two layered model showing resistivity distribution to a depth 60 m..... 79

Fig. 6.15: (a) Profiles of the measured in-phase/real (solid black), computed in-phase (dotted black), measured quadrature/ imaginary (solid red) and the computed quadrature (dotted red) components of the secondary electromagnetic field expressed as percentage of the primary electromagnetic field (b) a two layered model showing resistivity distribution to a depth 60 m..... 80

Fig. 6.16: (a) Profiles of the measured in-phase/real (solid black), computed in-phase (dotted black), measured quadrature/ imaginary (solid red) and the computed quadrature (dotted red) components of the secondary electromagnetic field expressed as percentage of the primary electromagnetic field (b) a two layered model showing resistivity distribution to a depth 60 m..... 81

Fig. 6.17: (a) Profiles of the measured in-phase/real (solid black), computed in-phase (dotted black), measured quadrature/ imaginary (solid red) and the computed quadrature (dotted red) components of the secondary electromagnetic field expressed as percentage of the primary electromagnetic field (b) a two layered model showing resistivity distribution to a depth 60 m..... 82

Fig. 6.18: (a) Profiles of the measured in-phase/real (solid black), computed in-phase (dotted black), measured quadrature/ imaginary (solid red) and the computed quadrature (dotted red) components of the secondary electromagnetic field expressed as percentage of the primary electromagnetic field (b) a two layered model showing resistivity distribution to a depth 60 m..... 83

Fig. 6.19: (a) Profiles of the measured in-phase/real (solid black), computed in-phase (dotted black), measured quadrature/ imaginary (solid red) and the computed quadrature (dotted red) components of the secondary electromagnetic field expressed as percentage of the primary electromagnetic field (b) a two layered model showing resistivity distribution to a depth 60 m..... 84

Fig. 6.20: (a) Profiles of the measured in-phase/real (solid black), computed in-phase (dotted black), measured quadrature/ imaginary (solid red) and the computed quadrature (dotted red) components of the secondary electromagnetic field expressed as percentage of the primary electromagnetic field (b) a two layered model showing resistivity distribution to a depth 60 m..... 85

Fig. 6.21: (a) Profiles of the measured in-phase/real (solid black), computed in-phase (dotted black), measured quadrature/ imaginary (solid red) and the computed quadrature (dotted red) components of the secondary electromagnetic field expressed as percentage of the primary electromagnetic field (b) a two layered model showing resistivity distribution to a depth 60 m..... 86

Fig. 6.22: (a) Profiles of the measured in-phase/real (solid black), computed in-phase component (dotted black), measured quadrature/ imaginary (solid red) and the computed

quadrature (dotted red) components of the secondary electromagnetic field expressed as percentage of the primary electromagnetic field (b) a two layered model showing resistivity distribution to a depth 60 m.. 87

Fig. 6.23: A map showing the second vertical derivative filter applied to the residual aeromagnetic data..... 88

Fig. 6.24: A map showing an analytic signal filter applied to the residual aeromagnetic data..... 89

Fig. 6.25: A ternary image of the total magnetic intensity map, the second vertical derivative filtered map and the analytic signal filtered map. 90

Fig. 7.1: Images comprising the synthetic and measured data set results: (a) the forward model depicting two major layers with a vertical conductive structure embedded in a highly resistive medium; (b) the measured apparent resistivity pseudosection of the synthetic data set, (c) the calculated apparent resistivity pseudosection of the synthetic data set, (d) the inverse model resistivity section of the synthetic data, (e) the measured apparent pseudosection of the measured data, (f) the calculated apparent resistivity pseudosection of the measured data, and (g) the inverse model resistivity section of the measured data. 92

Fig. 7.2: The vertical resistivity cross section model on a satellite image of the dam embankment..... 93

Fig. 7.3: Resistivity inverse model of the Lotsane Dam embankment. 94

Fig. 7.4: The temporal differences in inverted resistivity sections 97

Fig. 7.5: An interpretation model of the FDEM data..... 100

Fig. 7.6: (a) An in-phase component of the secondary EM field, (b) the out-of-phase component of the secondary EM field measurements 102

Fig. 7.7: (a) The in-phase plots (b) the out-of-phase plots (from Palacky, 1991, as cited in Reynolds, 2011).. 103

Fig. 7.8: Schematic showing a comparison of results from (a) frequency domain electromagnetic data profiles (b) frequency domain electromagnetic data model (c) 2D dipole-dipole resistivity inverse model.. 104

Figure showing independent time-lapse inverse models of the resistivity datasets acquired from October 2016 to October 2017.. 120

1 Introduction

Normal seepage through earth fill dams is a planned and accepted process, and it is typically drained by designed zoned filters within the embankment and foundation (Farooq et al., 2014). However, internal erosion and the continuous development of seepage pathways is a major concern in earth fill dams, and are a reason for many dam failures (Higgins, 1983; Bolève et al., 2009). Beside internal erosion, the development of seepage pathways is often related to geological and tectonic factors such as presence of faults, fractures and cavities (Lin et al., 2013). The uncertain outcomes and timescales over which such defective zones may evolve to threaten the safety and integrity of earth fill dams and therefore mandates the need for continuous inspection of dams. Usually, dam safety inspection utilizes visual inspections supported by the limited dam instrumentation (Lin et al., 2013). However, internal erosion and seepage paths are often difficult to assess from visual inspection and can only be observed after manifesting on the surface, at which time the integrity of the dam may have already been compromised.

Furthermore, dam instrumentation installed for dam condition monitoring is often not sufficient to effectively detect the earliest onset of internal erosion. This is mainly because dam instrumentations only provide sparse sampling of subsurface hydraulic conditions, and are limited to monitoring of seepage flow from the dam drainage system, displacements and pore water pressure within the dam embankment and foundation at discrete points of measurement (Sheffer, 2002; Lin et al., 2013). If founded on faulted and highly fractured basement rock, earth dams are at risk of hazards associated with faults because large fault displacements can result in uncontrolled leakage from dams (McMorran & Hull, n.d.). Fractures are also known to be preferential leakage pathways and their identification in dams is vital (Robert et al., 2012). As such, earth fill dams need periodic inspection and monitoring to detect anomalous conditions in the embankment and foundation materials (Jansen et al., 1983; Johansson & Dahlin, 1996; Osazuwa & Chii, 2010).

Geophysical techniques have demonstrated their utility in investigating dam conditions, and have been used to characterize preferential seepage pathways and internal defects in dam embankments and foundations (AlSaigh et al., 1994; Panthulu et al., 2001; Rozycki et al., 2006; Bolève et al., 2009). One of the advantages of using geophysical

techniques for dam embankments assessment is that they are non-invasive, hence do not contribute to enhancing dam failure processes. Nevertheless, most geophysical techniques do not directly detect the desired targets; they exploit the physical properties of the subsurface such as electrical resistivity, dielectric constant and magnetic susceptibility (Farooq et al., 2014).

The electrical resistivity and electromagnetic techniques have successfully been used to characterize dam embankment conditions and can be used to detect defects before visual evidence. Indeed, several researchers have applied electrical resistivity imaging to map internal erosion and preferential seepage pathways in dams, as well as to characterize bedrock conditions (e.g., Chen et al., 1996; Ranage et al., 1998; Osazuwa & Chinedu, 2008). Investigation results suggested that the applicability and efficiency of the electrical resistivity imaging in characterizing dam conditions is due to a strong contrast in electrical resistivities between the embankment and foundation materials, and between the compromised zones and the surrounding materials in dams. The electrical resistivity imaging is sensitive to changes in soil moisture conditions that are a result of anomalous seepage in dams and is also sensitive to the loss of fines due to internal erosion in the dam material (Panthulu et al., 2001; Sjö Dahl et al., 2006). A pathway can be conductive because of the high pore fluid and clay content (Revil & Cathles, 1999, as cited in Ikard et al., 2014). To study the subsurface resistivity changes with time, repeated 2D resistivity measurements are acquired over the same line, in the context of time-lapse measurements (Loke, 1999; Tsourlos, 2003; Karaoulis et al., 2010). Time-lapse resistivity measurements have been used successfully by several researchers to study the subsurface resistivity changes in dam embankments (e.g., Dahlin & Johansson, 1995; Johansson & Dahlin, 1996; Panthulu et al., 2001; Kim et al., 2004; Song et al., 2005; Panthulu et al., 2007). An advantage of time-lapse electrical resistivity measurements is their improved discrimination derived from interpretation of electrical resistivity data with respect to the initial data sets. This approach focuses the difference between the data sets on the actual change in the resistivity model and suppresses artifacts due to the resistivity structure (Loke, 1999).

The frequency domain electromagnetic (FDEM) method is used to measure the conductivity differences of earth materials (Brosten et al., 2005). In the case of dam investigations, possible seepage pathways can be located through the identification of

high or low conductivity anomalies. Anomalous zones that are fluid-filled and/or clay-filled tend to produce high conductivities and those filled with air can give low conductivity anomalies (Brosten et al., 2005). The FDEM method is also efficient in identification of fractures in the basement rock (Telford et al., 1990; Reynolds, 2011). However, just like the resistivity method (the reciprocal of conductivity), conductivity measurements can be affected by factors such as porosity, degree of pore saturation and pore fluid temperature. High-resolution aeromagnetic data is useful in locating regional structures such as faults and dykes. Therefore, the aim of this study was to use the electrical resistivity imaging method in conjunction with the FDEM method and high resolution aeromagnetic data to assess dam embankment condition of the Lotsane Dam.

1.1 Research objective

The objective of this study was to detect and locate probable weak zones that may be susceptible to seepage and internal erosion within the Lotsane Dam embankment.

To meet the research objective, a time-lapse electrical resistivity imaging of the Lotsane Dam embankment was conducted along a fixed profile. Thereafter, a frequency domain electromagnetic survey along a single profile on the embankment was also carried out. Further, high resolution aeromagnetic data of the Lotsane Dam vicinity were processed in order to map basement structures in the area. Finally, data visualization elements were undertaken to identify areas of data anomalies that are consistent with structural defects in the dam.

1.2 Research scope

The current work was focused on the use of the electrical resistivity and FDEM methods with the intent to assess the structure and to evaluate probable seepage pathways as potential defects in the embankment and the foundation at the Lotsane earth- fill dam. High resolution aeromagnetic data were also considered. Numerical modeling was a critical component of this study during data processing and interpretation.

1.3 Research significance

The importance of this study is twofold. Firstly, timely inspections of Lotsane Dam would warrant its safety and appropriate maintenance measures. Visual inspection for assessing the dam's integrity is not sufficient as it only applies to problems that have surface manifestations. For instance, development of hidden defects such as internal erosion, piping and preferential seepage paths usually cannot be detected by visual inspection until they have progressed to the surface at which time the integrity of the dam may already have been lost. Geophysical studies have demonstrated the utility of electrical methods to characterize dam embankment conditions and can be used to determine defects before surface manifestation. Secondly, the socioeconomic impacts that dams have upon communities who depend on them for safe, reliable supply of fresh water is important. This study therefore helps to expand the scope of monitoring and safety assurance measures employed by owners and operators of the Lotsane Dam to safeguard the dam's structural integrity and ensure operational lifespan.

2 Embankment dams

A dam is a water retaining structure designed to trap water behind an embankment, and is amongst the oldest man made constructions (Johansson, 1997; Case, 2012). Understanding how embankment dams are designed and constructed enables a dam examiner to determine deficiencies in the dam. Some types of embankment dams are more susceptible than others to failure. Therefore, a brief discussion of embankment dams, their designs and construction characteristics usually precedes the discussion of embankment investigations. Fell et al. (1992) have provided detailed descriptions on embankment dams. A description of the earth embankment dams presented in this thesis is not specific to any part of the world, but the general details of earth fill embankment dams.

2.1 Earth fill embankment dams

Dams which are made primarily from natural materials excavated at the dam site are referred to as embankment dams or fill-type dams (Narita, 2000; Ersayın, 2006). Embankment dams are classified into two main categories based on materials used for construction e.g., soil or crushed rocks. Thus, dams constructed from uniformly compacted soil into relatively thin layers at controlled moisture content are called earth fill embankment dams (Narita, 2000; Ambikaipahan, 2011) (Figure 2,1). In contrast, dams which are constructed from crushed rocks are called rock fill dams (Charles, 1993; Narita, 2000; Ersayın, 2006; Sjö Dahl, 2006; Novák et al., 2007; Cyganiewicz et al., 2007).

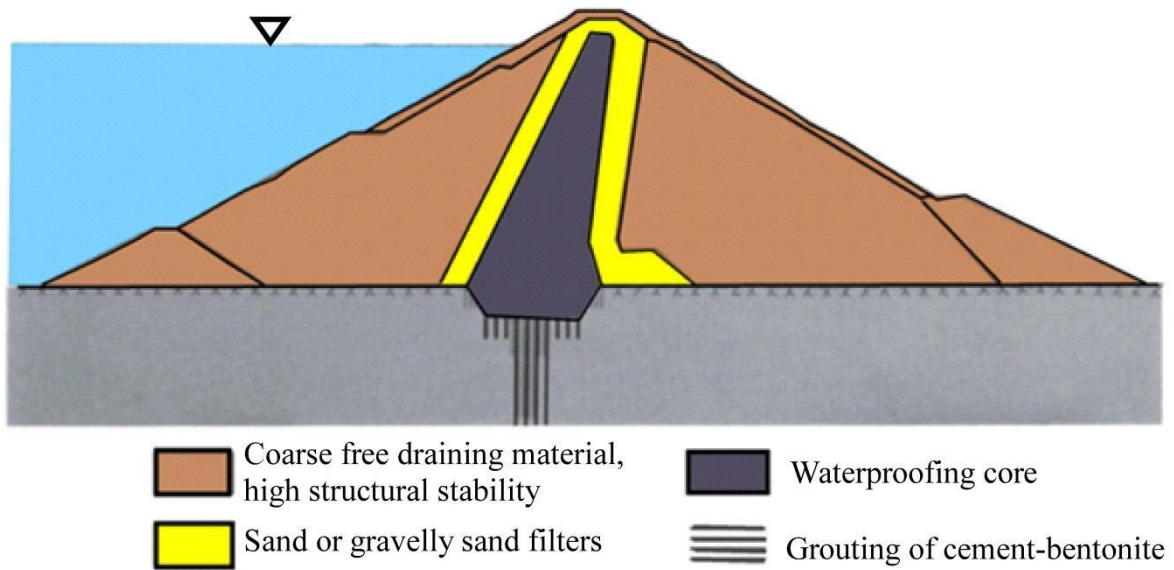


Fig. 2.1: Cross-section of an earth fill embankment dam with a central slightly inclined core, illustrating the principal zones and some details of the dam design (Adapted from Mori, 2009).

The core is a low permeability zone of the dam embankment and consists of fine grained soils, such as clays, clayey sands and silty sands. The zone's function is to control seepage flow through the dam (Fell et al., 1992; Sheffer, 2002; Mori, 2009). The role of filters is to prevent seepage induced loss of fines from the core (Mori, 2009). Filters can be placed in one or more zones, with a gradual increase in grain size from the core outwardly. Fine filters are typically sand or gravelly sand and coarse filters are usually gravelly sand or sandy gravel (Fell et al., 1992). The support fill consists of coarse free draining material, commonly crushed rock which adds stability to the dam (Sjodahl, 2006; Mori, 2009).

2.2 Embankment dam safety

There are more than 25000 large embankment dams world-wide, excluding those in China, where it is estimated that an additional 20000 more exist (ICOLD, 1995). The failure of a large modern dam with a large reservoir can potentially cause a lot of damage to property and considerable loss of life (ICOLD, 1987; Ersayın, 2006). According to the statistics of large dam failure summarized by ICOLD (1987), more earth embankment dams fail as compared to concrete dams (Sjödahl, 2006). Considerable attention must therefore be paid to earth embankment dam safety.

Most failures occur very early in the life of an earth embankment dam, particularly during the initial filling of the reservoir (Sjödahl, 2006). According to Forster et al. (2000a), around two thirds of all earthen dam failures are related to internal erosion occurring during the first five years of operation. Unlike overtopping scenarios, which are much easier to notice and monitor, internal erosion monitoring is a far more complex task, and an appropriate inspection scheme for regular observation of earth dams' performance is important (ICOLD, 1987; Johansson, 1997).

2.3 Current understanding of internal erosion and piping

A large portion of knowledge about problems associated with internal erosion comes from the studies of former dam incidents. Internal erosion in earthen dams washes out fine-grained particles from the filling material and results when seepage forces induce a migration of fine particles from the core out through the filter in the direction of flow (Johansson, 1997; Sheffer, 2002; Rönnqvist, 2010; Chang & Zhang, 2013). Removal of fine-grained particles by erosion and deposition of coarser-grained particles in the eroded zone increases the porosity and permeability of the core, in the process affecting the stability of the embankment and ultimately leading to failure of the dam (Sheffer, 2002; Rönnqvist, 2010; Braithwaite, 2013; Ikard, 2013). Internal erosion causes approximately 46% of all documented dam failures, ranked second only to overtopping, which is estimated to be causing roughly 48% of all documented dam failures (Forster et al., 2000a, b; ; Forster et al., 2002; Ikard, 2013).

There are zones in embankment dams particularly prone to internal erosion. They include areas around embedded structures such as conduits (Fig. 2.2 (a-c, e-h)), areas along spillway walls (Fig. 2.2 (d)), drains such as toe drains, stilling basin underdrains, etc., thus making erosion difficult to detect until it has progressed enough to be visible or detected by measurements (Sjödahl, 2006). Areas around and adjacent to conduits are especially susceptible to piping because of the difficulty in properly compacting the fill around conduits (Jansen, 1983). This tendency of internal erosion to concentrate adjacent to different kinds of installations within the embankment makes it difficult for dam instrumentation to detect erosion processes (Mattsson et al., 2008). High seepage rates resulting from increased porosity and permeability may be observed at the dam

toe, either in the form of clear or muddy water, but giving no indication of the source or location of leakage (Sherard et al., 1963; Sheffer, 2002).

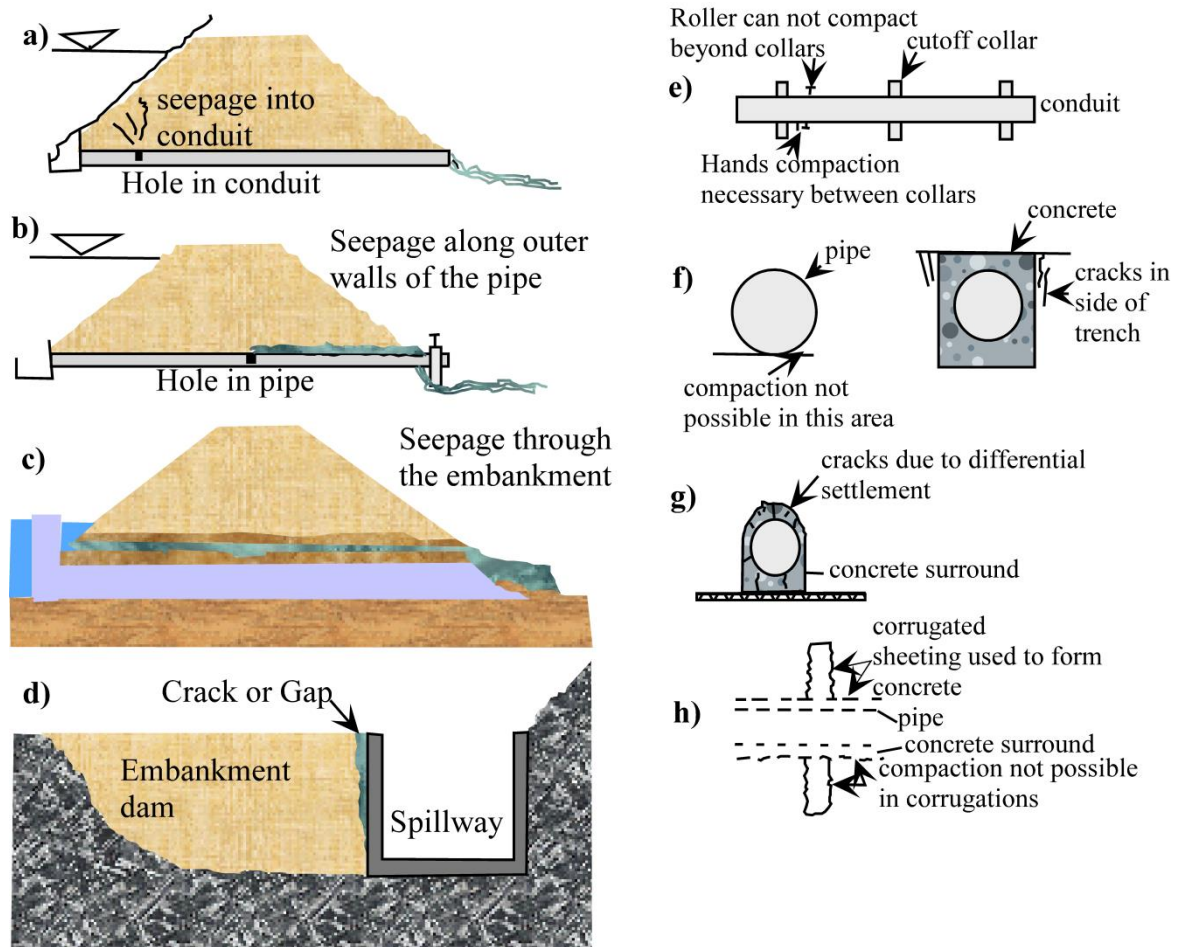


Fig. 2.2: Schematics of zones of the dam which are prone to internal erosion including (a) seepage through the embedded conduit in the dam (b) a hole in a pipe, leading to seepage along the walls of the pipe (c) seepage through the embankment (d) a gap between the embankment and the spillway wall, prone to internal erosion and a likely seepage pathway (e) a conduit with collars, with areas in between the collars and the conduit difficult to compact (f) areas below the embedded pipes, where compaction is particularly impossible. Also shown is a trench with side cracks, likely to be preferential seepage pathways (g) cracks due to differential settlement on the concrete that surrounds the pipes (h) pipes surrounded by concrete and corrugations, also contributing areas not possible to compact, hence prone to internal (Modified from FEMA, 2005; 2008 and Fell et al., 2008).

2.3.1 How internal erosion develops

By definition, internal erosion occurs when particles within an embankment or its foundation are carried downstream by seepage flow (Vazquez, 2014). For internal erosion to occur, a soil particle should become detached from the fill material and become transported through sufficiently large voids and constrictions (Rönnqvist, 2010). The seepage force acting upwards decreases the effective weight of the fill material, and thus the stability of the embankment, therefore detachment and transport of fill material require an upward acting force against the inter-granular forces, as well as drag forces relative to the buoyancy weight of the grain (Masannat, 1980; Rönnqvist, 2010). The continued detachment and transport of fill material (internal erosion progression) may lead to the development of piping.

Terzaghi et al. (1996) characterized types of piping causing embankment dam failures into subsurface erosion and heave. Subsurface erosion is a process starting at the discharge point of the water seeping through the non-homogeneous material of the dam foundation from the upstream side to the downstream side, and proceeds progressively backwards in the upstream direction towards the dam body along zones of high permeability (Masannat, 1980). When the seepage force becomes equal to, or exceeds the effective weight of the fill material, the fill material loses its strength and piping erosion of the fill material may take place along a developing erosional channel (Masannat, 1980; Sjö Dahl, 2006), a process referred to as ‘piping due to heave’, also known as hydraulic fracturing when it occurs in dam cores (Sherard, 1986). Table 2.1 shows brief explanations of some of the key terminology for internal erosion.

Table 2.1. Brief explanations of some key terms regarding the development of leakage and internal erosion in embankment dams (Modified from Sjö Dahl, 2006).

TERM	EXPLANATION
Piping	A form of internal erosion that results in the formation of a continuous tunnel through the embankment or foundation, regardless of the cause of initiation.
Suffusion	Suffusion is a form of selective erosion, where the fine particles in the fill material are removed leaving behind coarser particles. It is also referred to as internal instability, and fill materials which are

susceptible to suffusion are said to be internally unstable.

- Internal erosion Fill material particles within an embankment dam or its foundation are carried downstream by seepage flow.
- Backward erosion In backward erosion, piping starts at the interface between the core and the filter or between the fine- and coarse filter. The erosion propagates backwards, towards the upstream side of the dam into the core. Fines from the back of the forming tunnel are constantly suspended in the seepage, thus creating a backward enlargement of the tunnel. As the formed tunnel grows in width and height, the erosion is accelerated.
- Concentrated leak A concentrated leak may occur when there is a crack forming in the core between the up-, and down-stream side, or from hydraulic fractures, poorly compacted weak zones or other causes. Cracks can form if the core material is very stiff and the dam is subjected to movement. Cracks can also form due to differential settlement and the fact that the stiffness of the core may vary from point to point.
- Hydraulic fracture Hydraulic fracturing may occur due to various reasons in the low permeability zone when the seepage pore pressure equals the total stress acting on the fill material. This may cause opening of fractures or creation of new fractures leading to concentrated leaks.
-

The generally accepted phases of internal erosion studied in a refined model by Wan & Fell (2004) are as follows: initiation, continuation, progression and a breach phase (Fell et al., 2003; Wan & Fell, 2004; Fell & Fry, 2007; Mattsson et al., 2008). Below are the descriptions of these four phases of development:

Phase I. Initiation of erosion: Internal erosion may initiate for a number of reasons, but is generally due to erodibility of the material used (Höeg, 2002; Garner & Fannin, 2010). This is primarily influenced by the material's grading, but also by causes connected to defects arising from construction or design: e.g., segregation, low effective stresses due to arching and cracks (Fig. 2.3), filter and core incompatibility, etc. (Nilsson & Rönqvist, 2004; Garner & Fannin, 2010). Initiation processes of internal erosion inside an embankment dam are grouped as: concentrated leak, suffusion and backward erosion (and/ or piping) (Marot et al., 2007).

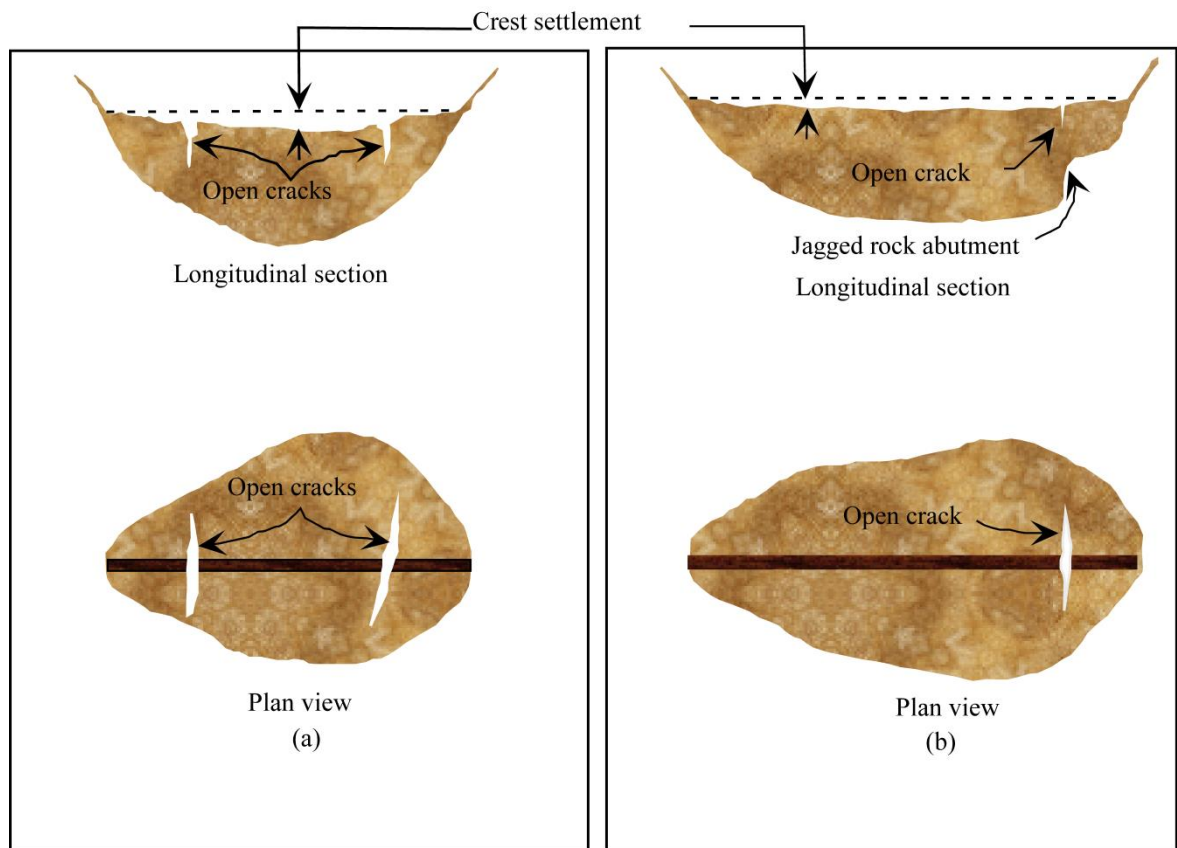


Fig. 2.3: Ordinary transverse differential settlement cracks across embankment zones. If transverse cracks extend into the core below the reservoir level they are especially dangerous because they could create a path for concentrated seepage through the core. The presence of transverse cracking indicates differential settlement within the embankment or underlying foundation (Modified from Mattsson et al., 2008).

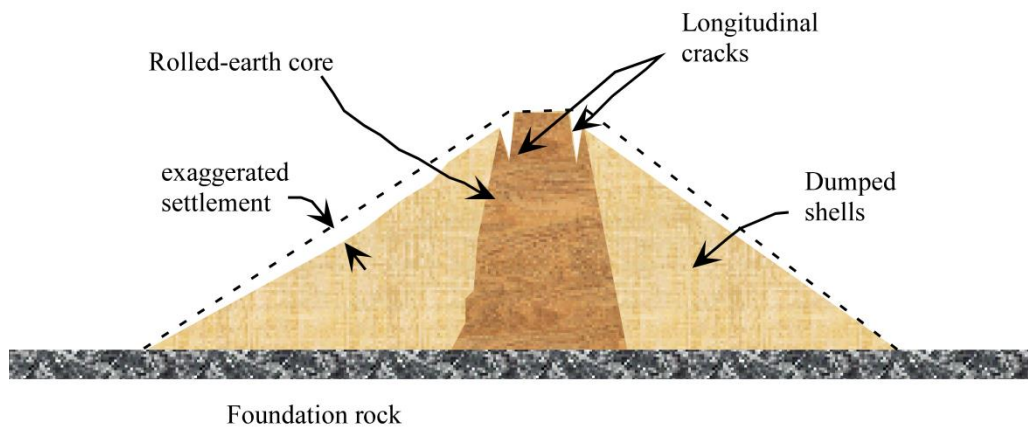


Fig. 2.4: Longitudinal differential settlement cracks between embankment zones. Longitudinal cracking usually occurs in a direction roughly parallel to the length of the dam embankment mainly as an indication of uneven settlement between adjacent embankment zones of differing compressibility, or due to tension from excessive settlement and lateral spread of the embankment (Modified from Mattsson et al., 2008).

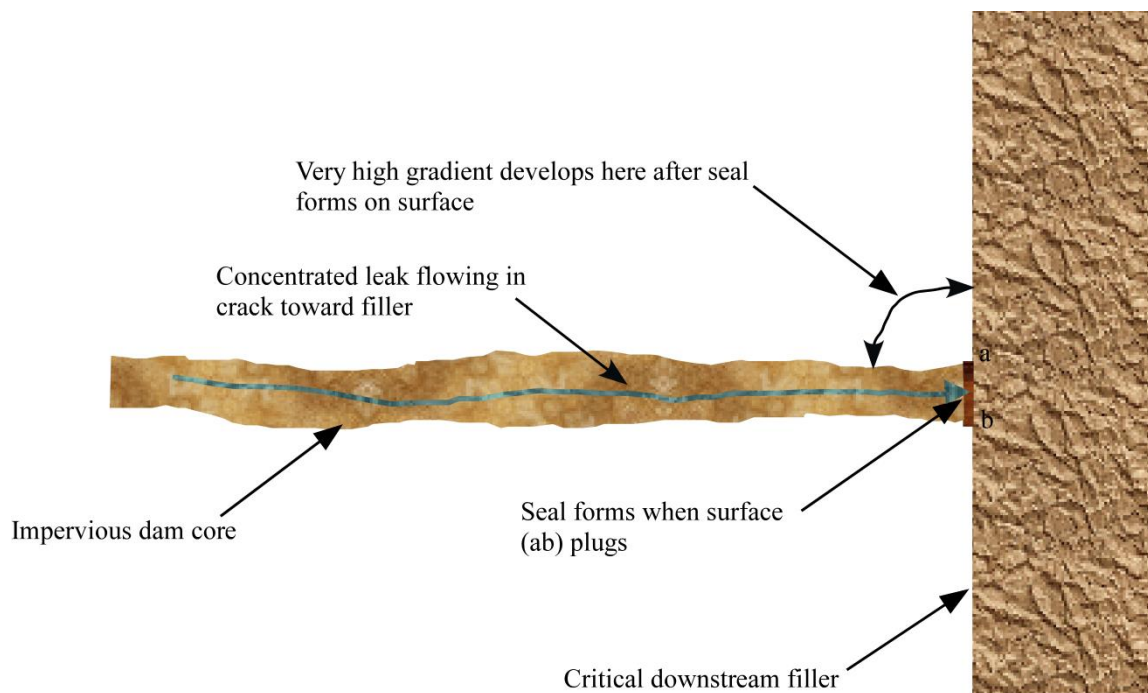


Fig. 2.5: Shows what happens when a concentrated leak discharges through the impervious dam core into the downstream filter. If the leak carries eroded particles of the core material that seals the filter face (ab), the water pressure in the leakage channel sharply rises and approaches the reservoir head. This creates a high seepage gradient through a short distance in the core to the adjacent portion of the filter (Modified from Sherard et al., 1984).

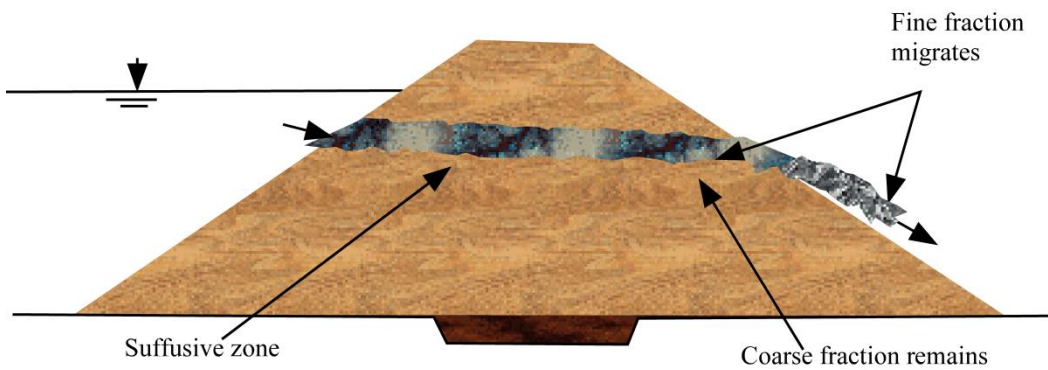


Fig. 2.6. Illustration of internal erosion process by suffusion. Fine-grained particles are eroded from a fill material composed of coarser particles, leaving behind coarser particles, a process which is very slow in its development and time dependent (Marot et al., 2007).

Phase II. Continuation of erosion: The initiation may discontinue if a filter function exist within the embankment material (i.e., self-filtering ability) or if the downstream interfacing material (usually the filter) is adequately graded in relation to its base i.e. the core (Rönnqvist, 2010). However, if the filter is incompatible to the core (i.e., too coarsely graded to function as a filter) erosion may continue; depending on the extent to which the filter is sealed by the eroded core material, Foster & Fell (1999, 2001) sub-grouped the continuation phase into the following conceptual levels:

- i) No-erosion (filter seals with no erosion of core),
- ii) Some erosion,
- iii) Excessive erosion (filter seals only after excessive erosion of the core), and
- iv) Continuing erosion (filter too coarse to allow the eroded particles from the core to seal the filter, which allows unrestricted erosion of the core).

When the volume of the eroded fine-grained material is larger than the volume of the coarser particles' void spaces, a progressive collapse may result (Sherard, 1992). Thus, sinkholes on the surface of dams (or other clear signs of internal erosion) are possible manifestations of continuous internal erosion (Rönnqvist, 2010). Whether internal erosion continues or self-healing occurs depends on the exit conditions for seepage flow (Sjödahl, 2006). In dams with central cores, the exit point for internal erosion in the core is the filter (Sjödahl, 2006; Mattsson et al., 2008; Rönnqvist, 2010). Adequate filters may effectively halt the internal erosion process by trapping the core material. According to

Forster & Fell (2001), very coarse filters or free surfaces result in continuation of the process.

Phase III. Progression to form a pipe: If initiation of erosion is due to a concentrated leak, the progression depends on the geometrical shape of the leak and the erodibility of the material (Sjödahl, 2006; Flores-Berrones & Lopez-Acosta, 2011). Progression to form a pipe depends mainly on how well the filter functions when the process is initiated by backward erosion, and in the case of initiation by suffusion, it is highly likely that at the end of the suffusion process the remaining material be eroded by backward erosion, hence forming a pipe (Sjödahl, 2006).

Phase IV. Formation of a breach: If internal erosion progresses to form a pipe as described in phase III, structural damages within the dam embankment may occur, and ultimately lead to dam failure. According to Sjödahl (2006), it is also worth mentioning that if the internal erosion was initiated by suffusion, breaching may occur without a preceding formation of a pipe. Figure 2.7 is an illustration of these four phases of internal erosion development, examples from the backward erosion scenario.

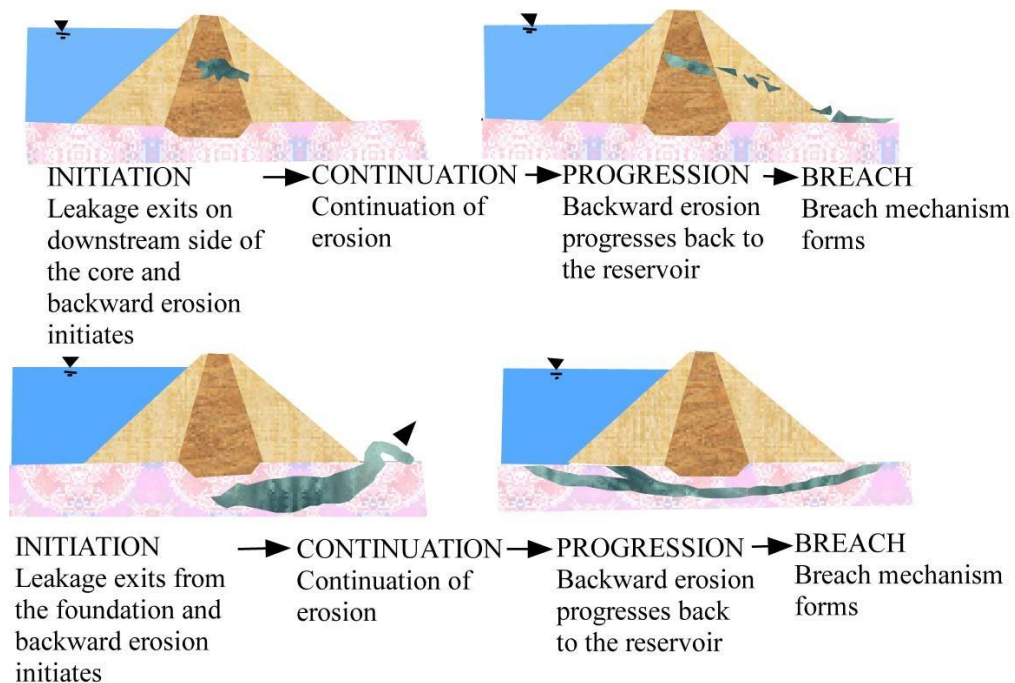


Fig. 2.7: Internal erosion initiated by backward erosion in the embankment (top) and in the foundation (bottom). Seepage detaches fine-grained particles at the exit point, and then transports these particles downstream as erosion gradually progresses upstream towards the source of water (Modified from Fell et al., 2008).

2.3.2 Parameters related to internal erosion

Parameters indicating internal erosion have been examined by Johansson et al. (1995) and Johansson (1997). Initially, internal erosion results in an increased porosity due to the transportation and loss of fines (Johansson, 1997; Scheuermann & Kiefer, 2010; Ke & Takahashi, 2012a, b). This affects a number of measurable parameters, such as density, seepage flow, hydraulic conductivity, temperature, seismic velocity, dielectricity and resistivity. Porosity changes may also have secondary impacts on some parameters. Resistivity for example is affected by both loss of fines and increased seepage.

2.4 Examination of dams

Examining the performance of dams to assure that possible failures are avoided or adequate warning time of potential or forthcoming failures is an essential part of dam safety program (Federal Energy Regulatory Commission, 2005). Measurements in dams are carried out either for continuous monitoring or for special inspections. Conventional methods have been studied by Nilsson (1995) and “New methods” by Johansson et al. (1995). Different methods have therefore been presented and evaluated in order to find their most appropriate application.

Application of some methods is best when the equipment is installed during the construction of the dam. Others can be applied after the dam has commenced operation, with or without the need for drilling (Johansson, 1997). Monitoring and inspection methods are therefore classified as: built-in monitoring, borehole methods and non-destructive testing methods.

2.4.1 In-built monitoring

In-built monitoring systems are the most common systems for monitoring of embankments and are usually installed in dams during construction phases (Johansson, 1997). They include, amongst others, crest settlements and horizontal movement points for measuring the crest and internal movements, survey monitoring points (SMPs) for monitoring surface movements of the embankment and piezometers for monitoring pore water pressures. Installing the monitoring systems for long term monitoring and

distributing these systems into several sections provides information about the temporal and spatial distribution of changes in the dam due to deterioration or aging of the dam, hence increasing the efficiency of the systems (Jansen, 1989; Johansson, 1997).

2.4.2 Borehole methods

Boreholes are drilled using low pressure drilling methods to avoid hydraulic fracturing of the core, and are useful for geophysical methods such as borehole radar and sonic cross-hole (Johansson, 1997). Both methods use tomographic analysis to give information about the conditions in the dam between the boreholes. Borehole radar and sonic cross-hole methods are mainly used for single examinations, but can also detect changes which have occurred between measurements. Standpipes for measuring water levels are also installed in boreholes.

2.4.3 Non-destructive testing

Ground penetrating radar measures the differences in electrical conductivities or radio wave velocities in the soil. Measurements are made by moving antennas along the dam embankment. Repeated measurements are possible, but the method is not suitable for regular monitoring (Johansson, 1997). The electrical resistivity method is performed by a pair of current electrodes and another pair of potential electrodes driven sufficiently into the ground for good contact along the dam embankment. The electrical resistivity properties of the ground depend mainly on water content, water quality and grain size. Different rates of leakage through the embankment causes anomalies in the streaming-potential (Johansson, 1997), and these variations can be used to infer or detect leakage in the embankment using the self-potential (SP) method. Both electrical resistivity and SP methods are suitable for regular monitoring.

2.5 Methods used in this study

The electrical resistivity imaging method was used to investigate the resistivity structure of Lotsane Dam embankment and the foundation. The FDEM method was also used in conjunction with the resistivity method. Additionally, high resolution

aeromagnetic data were used to investigate the presence of geologic structures in the study area.

3 Methods

3.1 Electrical resistivity imaging (ERI) method

The electrical resistivity imaging method is a non-invasive geophysical technique used for investigating subsurface conditions (e.g., Loke, 1999; Ogungbe et al., 2010; Oyedele et al., 2013). It is based on the principle that the distribution of electrical potential in the ground around a current-carrying electrode depends on the electrical resistivity of soils and rocks (Wightman et al., 2003; Ibeneme et al., 2013; Jika & Mamah, 2014). The applications of ERI method have developed rapidly during the last decade or two.

The usual practice is to apply an electrical direct current (DC) between a pair of electrodes implanted in the ground and to measure the potential difference between the other pair of electrodes that do not carry current (Kearey et al., 2002; Reynolds, 2011; Nordiana et al., 2012; Ibeneme et al., 2013; Opeyemi, 2013). Usually, the potential electrodes are in line between the current electrodes, but in principle, they can be located anywhere (Jika & Mamah, 2014). Detailed description of the method is given in other publications (e.g., Telford et al., 1990; Parasnis, 1997; Reynolds, 1997).

3.1.1 Background

Electrical resistivity imaging (ERI) has played an important role in addressing a wide variety of hydrogeological, environmental and geotechnical and engineering problems (Panthulu et al., 2001; Gardi, 2014). A more accurate model of the subsurface is a two-dimensional (2D) one where the resistivity changes in the vertical direction, as well as laterally along the survey line (Loke, 2007). Direct current resistivity methods have frequently been considered to give poor resolution and to generate major uncertainties (Loke et al., 2013), and were hardly used in geological engineering projects, which often require more accurate subsurface models. However, the development of modern multichannel and multi-electrode systems and the advancements in resistivity inversion routines have improved the resolution of DC resistivity survey significantly over the last two decades, and are now widely used in geotechnical, hydrogeological, environmental and mining applications (Aizebeokhai et al., 2010; Loke et al., 2013; Zarroca et al., 2015). Dahlin & Johansson (1995), Johansson & Dahlin

(1996) and Panthulu et al. (2001) have successfully used electrical resistivity methods to characterize the subsurface conditions in embankment dams. On the other hand, Osazuwa & Chinedu (2008) had earlier used this method to investigate and map the high permeability zones beneath an earthen dam in the Zaria area, Nigeria. Other previous uses of ERI, as reported by Smith & Sjogren (2006) include: mapping of bedrock channels by Chen et al. (1996), Ramage et al. (1998) and Gilson et al. (2000); archaeological surveys (Noel & Xu, 1991); mapping of subsurface pipes (Vickery & Hobbs, 2002); remediation site analysis and mapping (Bentley & Gharibi, 2004).

3.1.2 Theory

Electrical resistivity is a measure of the difficulty in passing an electric current through a volume of material (soils or rocks) with a given length and cross-sectional area (Smith & Ward, 1990; Reynolds, 1997; Loke, 2001; Kearey et al., 2002; Denchik & Chapellier, 2005; Sjogren, 2006; Gardi, 2014). Electrical resistivity is a function of various material properties such as the mineral and fluid content, porosity and degree of water saturation (Johansson, 1997; Loke, 1999; Smith & Sjogren, 2006; Khalil & Santos, 2009).

The resistivity imaging technique is based on Ohm’s law (equation 3.1), which states that the electrical current (I, measured in Amperes) in a material is directly proportional to the potential difference (ΔV , measured in Volts) across it (Loke, 2001; Kearey et al., 2002; Milson, 2003; Aizebeokhai, 2010; Sakindi, 2012; Abdelwahab, 2013).

$$R = \frac{V}{I} \dots\dots\dots (3.1)$$

However, the resistance (R) is also directly proportional to the length of the conducting material, L, and inversely proportional to the cross-sectional area (Fig. 3.1), A (equation 3.2), with the constant of proportionality being the resistivity.

$$R = \rho \frac{L}{A} \dots\dots\dots (3.2)$$

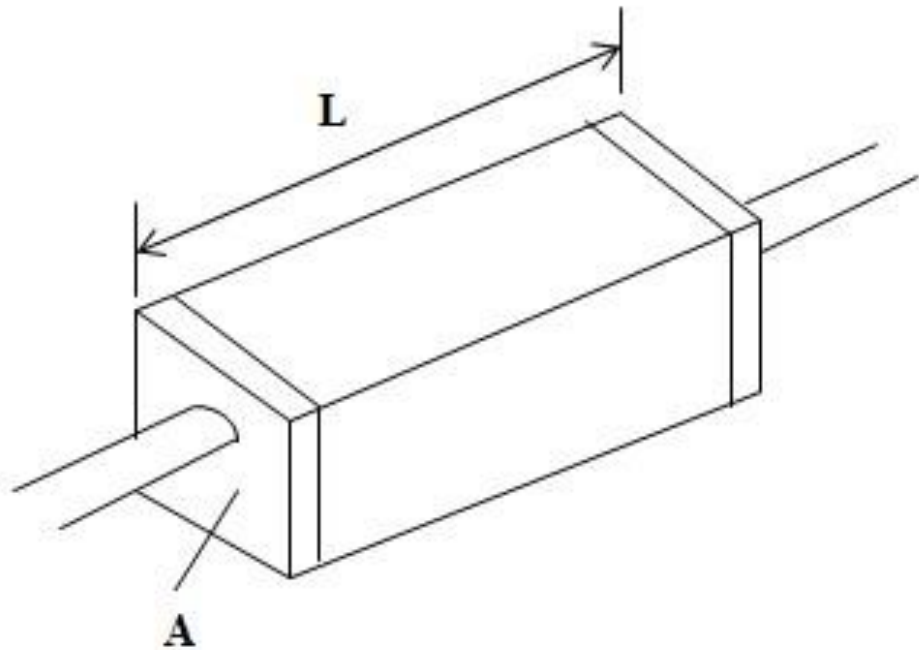


Fig. 3.1: A piece of resistive material with electrical contacts on opposite ends (Modified from Sakindi, 2012).

Combining equations 3.1 and 3.2 to solve for resistivity and introducing a geometric factor (K) results in another expression (equation 3.3). The geometric factor incorporates from each current electrode to each potential electrode, and the half space (Loke, 2001; Milson, 2003; Aizebeokhai, 2010).

$$\frac{V}{I} = \rho \frac{L}{A}, \therefore \rho = \frac{AV}{LI} = K \frac{V}{I} \dots\dots\dots (3.3)$$

The measured resistivity would be the same as the true resistivity for homogeneous subsurface distribution, but it is never the case in practical measurements (Sjödahl, 2006). Therefore, the measurements are given as apparent resistivity (ρ_a) as shown in equation 3.4, defined as the resistivity of an electrically homogeneous and isotropic half-space that would yield the measured relationship between the applied current and the potential difference for a particular arrangement and spacing of electrodes (Loke, 1999, 2001; Wightman et al., 2003; Aizebeokhai, 2010; Ibeneme, 2013).

$$\rho_a = K \frac{\Delta V}{I}, \dots\dots\dots (3.4)$$

Equations giving the apparent resistivity in terms of applied current, distribution of potential, and arrangement of electrodes can be arrived at through an examination of the potential distribution due to a single current electrode, and have been discussed in detail by a number of authors (e.g., Telford et al., 1990; Reynolds, 1997; Kearey et al., 2002; Ibeneme et al., 2013).

3.1.3 Resistivity of earth materials

The success of the resistivity method in delineating subsurface materials depends on, among other factors, horizontal resolution, vertical resolution and signal-to-noise ratios. These factors are site specific and depend on the conditions for the survey. Above all, the fundamental condition that needs to be met for the resistivity method to be useful is that there should be physical property contrast between subsurface materials to be delineated (Loke, 2004; Sjödaahl, 2006). Therefore, prior knowledge of the properties of the materials at the site being investigated is necessary when using the resistivity method.

The resistivity of some common soils and rocks vary within a wide range (Fig. 3.2) and these differences form the basis of resistivity imaging survey (Keller & Frischknecht, 1966; Telford et al., 1990; Sjödaahl, 2006). As shown in Figure 3.2, the overlap in resistivity between the different types of earth materials is apparent because the resistivity of a particular rock or soil sample depends on a number of factors. As such, measured resistivity values should only be attributed to a specific material category after gathering additional information about the conditions of the ground under investigation.

Electrical conduction in earth materials is either electronic or electrolytic. In electronic conduction, the flow of electric current is via free electrons (Loke, 2004) and is important when conductive materials are present, such as sulphides and graphites in mineral surveys (Kearey et al., 2002). In electrolytic conduction, the flow of electric current is through the movement of ions in fluids contained in the material. In the case of environmental surveys, the most common soil and rock forming minerals are insulators when in a dry state (Kearey et al., 2002), thus the amount and properties of the saturating fluids

largely determine the resistivity. As such, electrolytic conduction of current flow in such surveys is the more common mechanism (Loke, 2004; Sjödaahl, 2006).

Igneous and metamorphic rocks usually have high resistivity values (Loke, 2004). Their resistivity depends on the degree of fracturing and the number of fractures filled with fluids. Fractures, faults, shear zones constitute dominating current paths, whereas solid rocks are normally considered as poor conductors, unless they have significant metallic content (Loke, 2004). Thus, a given rock type can have a large range of resistivity values, from about 1000 to 10 000 000 Ω.m depending on whether it is wet or dry (Loke, 2004). This is an important characteristic in the detection of fracture zones and other weathering features.

Sedimentary rocks on the other hand usually have higher water content because of their high levels of porosity. Porosity is the major control of the resistivity of rocks, and resistivity generally increases as porosity decreases (Kearey et al., 2002). Therefore, sedimentary rocks have low resistivity values compared to igneous and metamorphic rocks (Loke, 2004). The resistivity values range from 10 to about 10 000 Ω.m, with most values below 1000 Ω.m. Beside porosity, the resistivity of rocks also depend on the total dissolved solids (TDS) content in the pore fluids.

Unconsolidated sediments generally have resistivity values ranging from about 10 to less than 1000 Ω.m. Electric current conduction in these sediments are concentrated to the pore spaces that are fluid filled, and is also dependent the clay content (Telford et al., 1990; Loke, 2004; Sjödaahl, 2006). Clayey soils normally have very low resistivity values. Similarly, ground water has low resistivity values, ranging from 10 to 100 Ω.m depending on the concentration of the total dissolved solids. The very low resistivity of sea water (about 0.2 Ω.m) is due to its relatively high salt concentration (Loke, 2004).

A number of equations have been used in different models to describe the relationship between the resistivity of porous rocks and the fluid saturation factor. One equation is the Archie's law (equation 3.5), applicable to certain types of rocks and sediments, in particular, those that have low clay content.

$$\rho = a\rho_w\phi^{-m} \dots\dots\dots (3.5)$$

Where ρ , is the rock resistivity, ρ_w is the fluid resistivity, ϕ is the fraction of rock filled with water, while a and m are two empirical parameters (Keller & Frischknecht, 1966). Sjö Dahl (2006) gives a detailed discussion of Archie's law, while de Lima & Sharma (1990) deals in details with other equations for sediments with significant clay content.

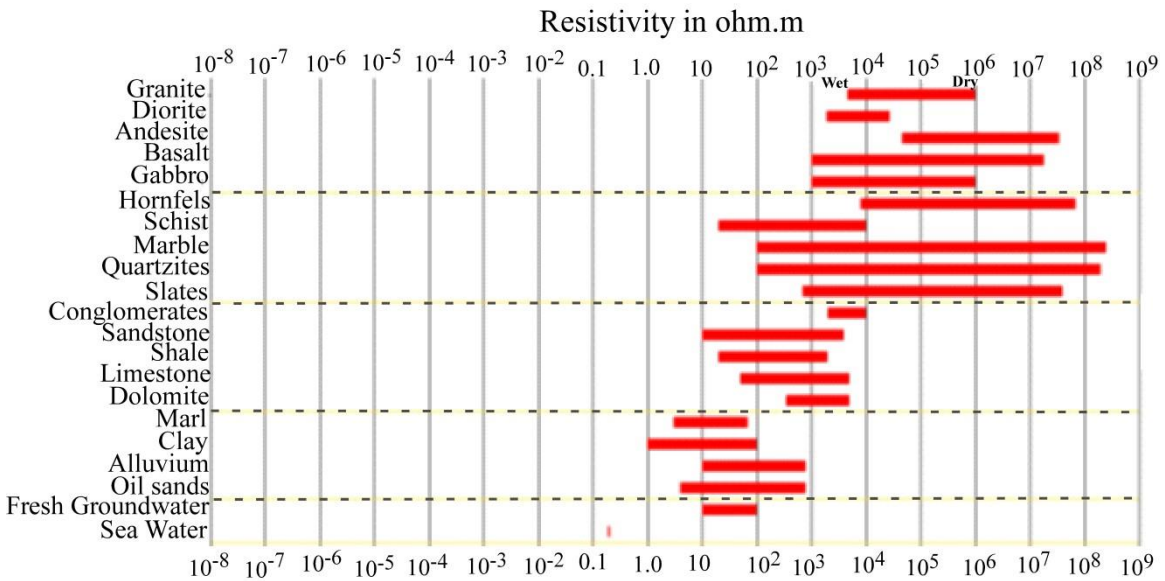


Fig. 3.2: Resistivity of earth materials (Modified from Loke, 2004).

3.1.4 Data acquisition

Four electrodes are generally placed at arbitrary locations; however, a number of electrode configurations are commonly used for resistivity data acquisition. The types of electrode arrays that are most commonly used (Schlumberger, Wenner, and dipole-dipole) are shown in Figure 3.3. The choice of a particular array depends on a number of factors, which include the geological structures to be delineated, subsurface heterogeneities, resistivity meter sensitivity, the background noise level and electromagnetic coupling (Aizebeokhai, 2010). Sensitivity of the array to vertical and lateral variations in the resistivity of the subsurface, the depth of investigation, the horizontal data coverage and signal strength, are some of the factors to be considered in the choice of the array. For instance, the Wenner array is generally good in resolving vertical changes (i.e., horizontal structures), but relatively poor in detecting horizontal changes (Loke, 2001; Maganti, 2008; Marchetti & Settini, 2010; Alwan, 2012). The

dipole-dipole array is sensitive to horizontal changes in resistivity, but relatively insensitive to vertical changes in the resistivity, hence making it suitable for imaging vertical structures such as dykes and cavities in the subsurface, but relatively poor for horizontal structures such as sills or sedimentary layers (Loke, 2001).

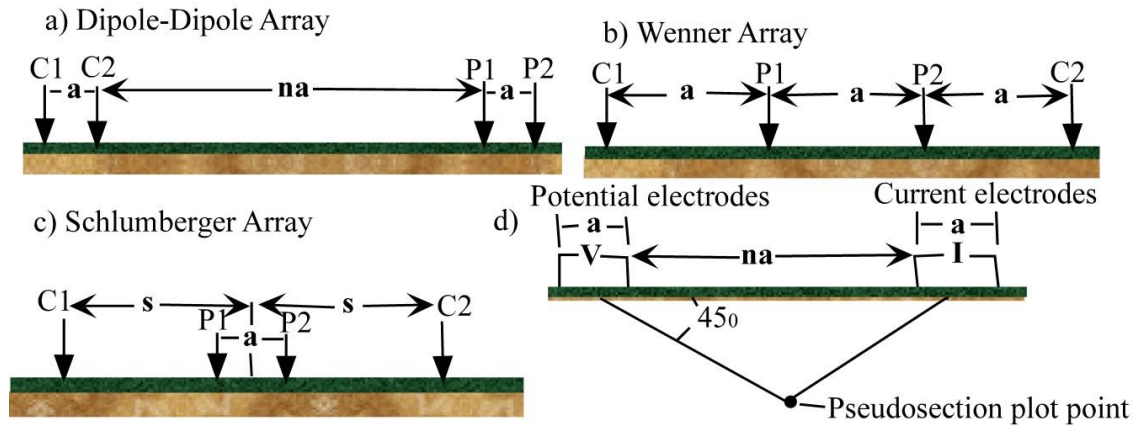


Fig. 3.3: Electrode configurations (a, b and c) commonly used in resistivity surveys and their descriptions using the a -spacing, s -spacing ($n*a$) and the n -factors. The a -spacing represents the separation distance between the electrodes, and is usually kept fixed at the smallest unit electrode spacing for the first measurements and the n -factor is constantly increased in order to increase the depth of investigation for the Dipole-Dipole array. The Wenner array represents a special case of the Schlumberger array when $n=1$. Bottom right; (d) is a sketch showing the pseudo section plotting point for the dipole-dipole array, at the intersection of two lines starting from the mid-point of the dipole pairs, with a 45° angle to the horizontal.

3.1.5 Instrumentation

The basic parts of an electrical resistivity measurement system include a power source, meters for measuring current and voltage, cables, reels, various connectors and electrodes. Current electrodes used with alternating current (or commutated direct current) instruments are commonly stakes of bronze, aluminum, copper, or steel, about 50 cm in length, which must be driven several centimeters into the ground to make good electrical contact (Robinson & Coruh, 1988; Telford et al., 1990; Loke et al., 2011). Very dry conditions leading to high contact resistance between the ground and the electrodes can be improved by moistening the ground around the electrodes with salty water. Direct Current resistivity meters include a DC ammeter sensitive to currents ranging from 2 mA to 500 mA (Robinson & Coruh, 1988; Telford et al., 1990; Loke et

al., 2011), depending on electrode spread, type of ground and power used, and a high impedance (1 M Ω or greater) DC voltmeter sensitive to potential differences ranging from 10 mV to perhaps 20 V (Robinson & Coruh, 1988; Telford et al., 1990). Insulated connecting wires of low-resistance used for connecting electrodes in the current and potential circuits, are wound on portable reels (Robinson & Coruh, 1988; Telford et al., 1990).

3.1.5.1 Multi-electrode and multi-channel systems

The multi-electrode and multichannel acquisition systems consist of multichannel transmitters and receivers that enable them to carry out a series of measurements simultaneously, thereby increasing the data acquisition speed (Aizebeokhai, 2010; Loke, 2011). These systems also comprise of a large number of electrodes, 24 or more, connected to a multi-core cable (Griffiths & Barker, 1993; Loke, 1999; Bernard et al., 2006; Loke, 2011; Loke et al., 2011), and a resistivity meter with the relays located internally, which ensure the switching of the electrodes according to a sequence of readings predefined and stored in the internal memory of the equipment (Loke, 1999; Bernard et al., 2006; Loke, 2011). Two or more components of the multi-electrode systems are usually housed in the same box to make the systems more compact and portable, with the multi-core cable attached to an internal electronic switching unit (Loke, 1999; Aizebeokhai, 2010; Loke, 2011).

A typical multi-electrode and multichannel system is the Iris system, shown in Figure 3.4. This system comprises the Syscal Pro resistivity/IP unit. The Syscal Pro is a ten-channel reception multi-electrode resistivity meter that uses a command file to acquire measurements from pre-determined current electrode and potential electrode configurations. With the Iris Syscal Pro system, resistivity measurements can be obtained simultaneously for a single pair of current electrodes. This makes the acquisition more efficient.

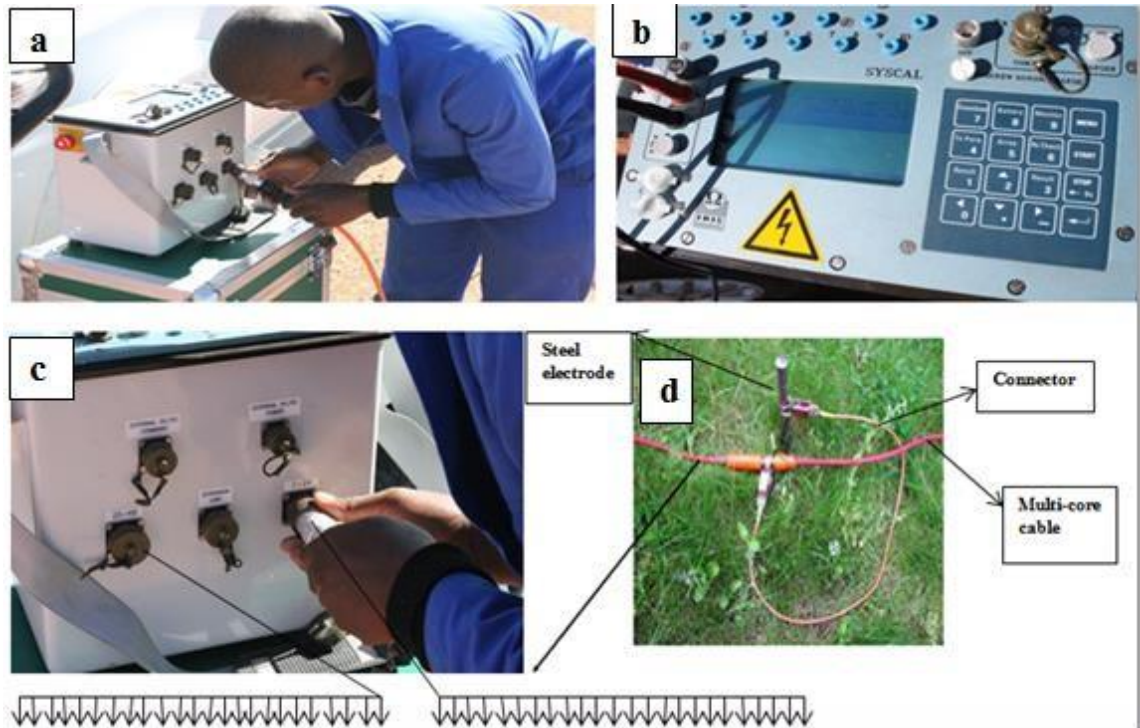


Fig. 3.4: Photographs showing the Iris system, comprising (a) the Syscal Pro switch unit, having the multi-core cable for controlling a set of electrodes connected in a line (b) the top part of the Syscal Pro unit, with the display screen at the center (c) the split-spread resistivity meter-electrodes arrangement, with the Syscal Pro unit at the middle (d) electrodes in the ground, connected to the multi-core cable.

3.1.6 Field procedure

In field surveys, the cables are rolled out along the survey line(s) as pre-designed by the field crew and the electrodes are connected to the cables via electrode take-outs (Loke et al., 2011). The acquisition system then automatically checks the electrode contacts (contact resistance) and scans through a pre-defined measurement protocol (Dahlin, 2001). Two-dimensional (2D) electrical resistivity imaging involves the measurements of apparent resistivity from electrodes placed along a line using a range of different electrode separations and midpoints. The procedure is repeated for a number of combinations of current and potential electrode positions as defined by the survey configuration.

If the surveyed profile to measure is longer than the spread, the area covered by the survey can then be extended along the profile using the roll-along technique (Dahlin,

2001; Bernard et al., 2006). This can be achieved by moving the cables past one end of the line, for example, shifting a quarter or half of the total layout length after completing a sequence of measurements (Fig. 3.5). The resistivity of the 2D model is assumed to vary both vertically and laterally along the survey line but constant in the direction perpendicular to the survey line (Loke et al., 2011).

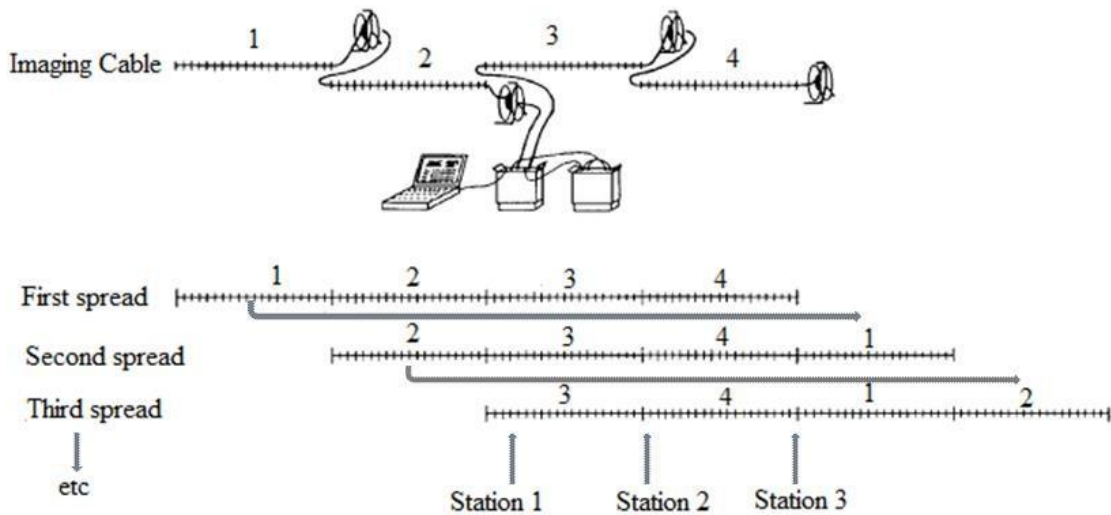


Fig. 3.5: Sketch of a multi-electrode data collection system, where the markings on imaging cables indicate electrode positions. This figure also shows how imaging cables are moved when using a roll-along technique (Modified from Overmeeren & Ritsema, 1988, as cited in Dahlin, 2001). Total layout length is 480 m when using 48 electrodes with 10 m electrode spacing.

3.1.7 Depth of investigation of multi-electrode resistivity imaging surveys

The total length of imaging cables is the product of the electrode spacing and the number of electrodes, for example, 48 electrodes at 5 m and 10 m spacing would give a total cable length of 240 m and 480 m, respectively, which determines the maximum depth of investigation. For the three commonly used arrays: the Schlumberger, Wenner and the dipole- dipole, the maximum depth of investigation is of the order of 0.2 times the total spread (Bernard, 2003). Each of the electrode configurations used in resistivity surveys features various benefits and limitations in terms of vertical penetration, lateral resolution and field set-up, but all follow the same general rules that: the longer the length of the current line, the deeper the penetration of the current and; the farther the potential receiving electrodes from the current transmitting electrodes, the more representative the potential of the resistivity of deep layers (Kearey et al., 2002;

Bernard, 2003; Bernard et al., 2006). The depth on investigation also depends on the measurability of the potential at the potential electrodes. For deep investigation depths, the electrodes have to be far away from each other, the K coefficient has thus an important value, and the potential signal becomes small, possibly difficult to measure.

3.1.8 Data processing

The large amount of data from resistivity measurements acquired by the use of multi-electrode ERI systems requires automated data handling and processing in order to obtain true resistivity of the subsurface. The steps in search of the true subsurface resistivity model include data quality control and noise reduction, creation of pseudo sections, inversion and modeling of data.

3.1.8.1 Data quality control and noise reduction

The quality of the field data is an important factor in production of the resistivity model that closely resembles the subsurface (Loke et al., 2000). Large variations in adjacent data points in a pseudo section are often a sign of poor data quality in the measurements, and can always be eliminated from data base before proceeding to the next step of achieving a final subsurface resistivity model. These bad data points usually result from instrumentation errors, shorting of the cables in wet conditions, operator mistakes during data acquisition or failure in the switching unit (Sjödahl, 2006). If the field data are of poor quality, with unusually high or low resistivity values, the pseudo section needs to be examined for spots of relatively low or high values; they likely represent bad data points. The Geotomo Res2dinv program can be used to plot the data in profile form, which helps identify the bad data points, and remove them from the data set manually (Loke, 2000).

Noise sources that have been observed at dam sites are steel sheet walls, metal objects, grounding cables, concrete structures and metal pipes for instrumentation (Sjödahl, 2006). These noise sources usually do not vary with time, therefore can be minimized by using monitoring systems to carry out time-lapse resistivity measurements, or by using permanently installed electrodes to eliminate errors associated with misplacement of electrodes over time. Additionally, assuring good grounding conditions minimizes

the effects from noise since poor grounding conditions would lead to high electrode contact resistance values; hence the lower current transmission levels (Sjödahl, 2006). Lower current levels give smaller potential readings and lower signals-to-noise ratios.

3.1.8.2 Pseudo sections

A conventional way of displaying apparent resistivity data from a 2D imaging survey is to plot them using the pseudo section contouring method, where the electrode separation or effective depth of penetration is used for depth (Loke, 1999; Sjödahl, 2006). The distance along the survey line is given on the x-axis and the y-axis represents the pseudo depth (Fig. 3.6). The horizontal location of the data point is at the midpoint of the two pairs of electrodes being used, and in case of the dipole-dipole electrodes array, the vertical location of the plotting point is at the intersection of two lines starting from the current electrode and potential electrode dipole pairs, with a 45° angle to the horizontal (Loke, 1999). However, this is merely a plotting convention, and does not mean that the depth of investigation is given by the intersection point of the two 45° angle lines.

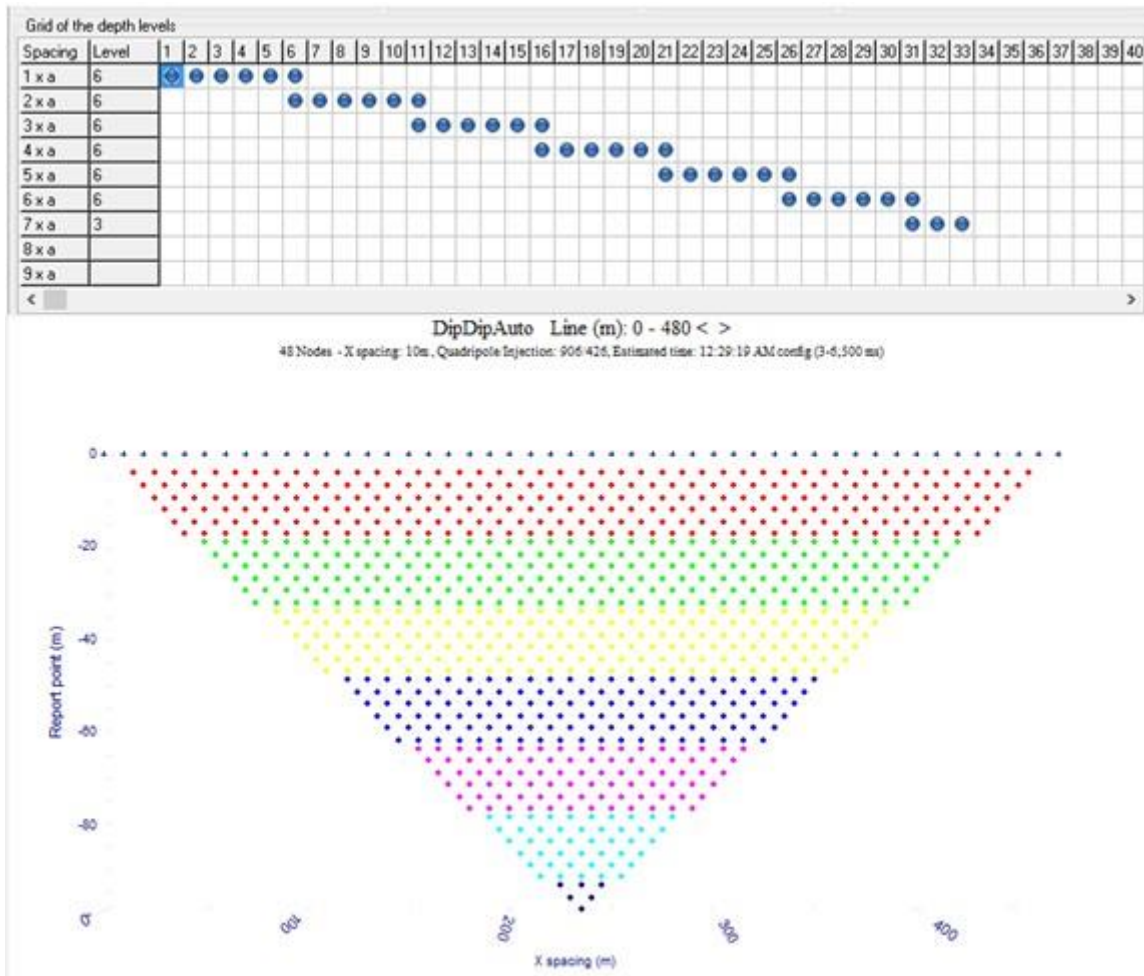


Fig. 3.6: Schematic diagram of a pseudo section in a dipole-dipole array. The lower part of the figure, on the x-axis is the distance along the survey line for a standard compute sequence, and on the y-axis are the depth levels, relative to the investigation depth. The increasing of the distance between the current and potential electrode pairs allows for reaching deeper investigation depth. The first line of crosses on the x-axis represents the electrode positions, and the dots that lie below them symbolize the data pots, each plotted between two pairs of electrodes. The top part of Figure 3.6 shows how the software creates sequences (Electre Pro) allowing only up to 9 different spacings in the sequence. In this case a is the x-grid spacing, and can be doubled or tripled for higher values of depth levels, generally from a depth level of 6 or 8.

The pseudo sections give approximate picture of the true subsurface resistivity distribution, and it differs from the true resistivity model of the subsurface because it is made from apparent resistivity data (Loke, 1999; Sjödaahl, 2006), hence the need for inverse modeling. The pseudo section is made to present observed (raw) data, and helps in rapid assessment of the quality of data (Fig. 3.7a). Alternatively, apparent resistivity

data can be presented in profile form, making it even much easier to edit/remove any bad data points (Fig. 3.7b).

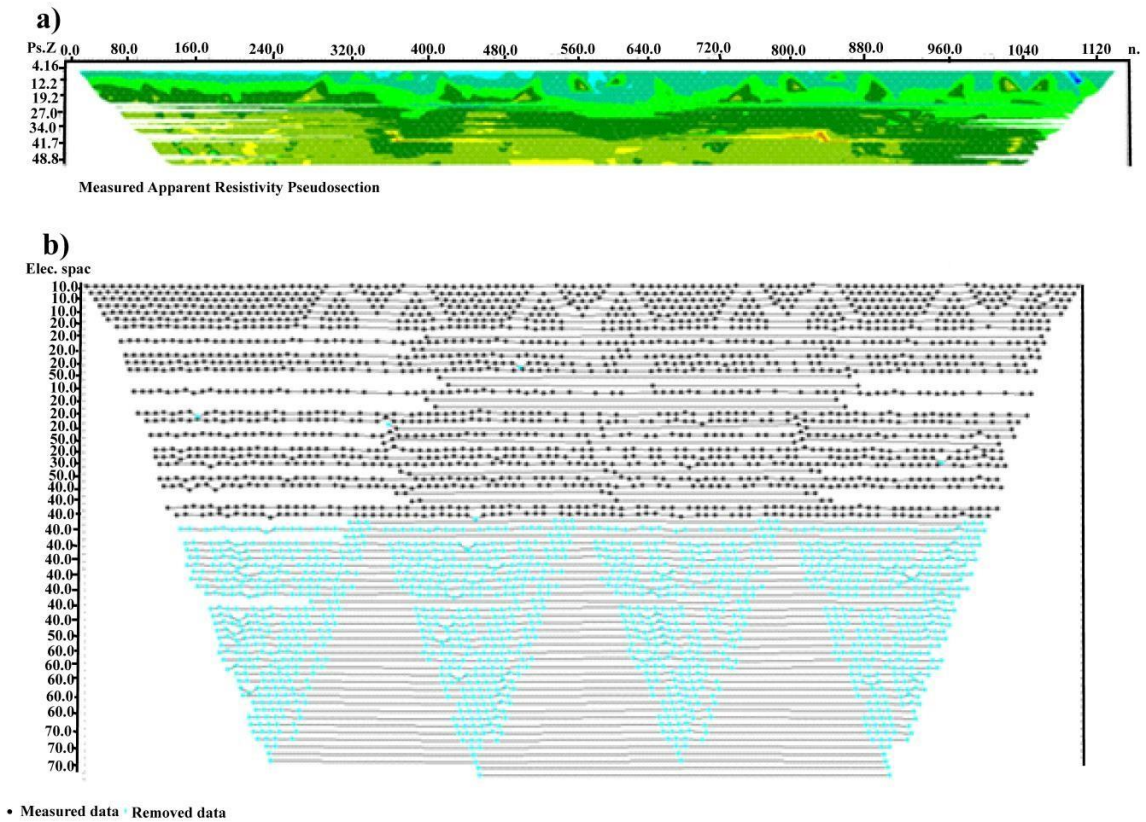


Fig. 3.7: An example of a field data set with some bad data points (a) the apparent resistivity data in pseudosection form and (b) in profile form. The black dots represent the measured data while the blue dots represent removed data points.

3.1.8.3 Inversion and forward modeling

In inverse and forward problems, there is a mathematical relationship that links the measured quantities to the quantities of interest (Ganse, 2008). Figure 3.8 illustrates briefly the relationship between data and a model, as well as inversion and forward modeling. The inversion process generates a generic model while the forward modeling process calculates a synthetic data set. The observed and calculated data sets are compared for equivalency. If the observed data and the calculated synthetic data sets do not agree, the model is altered and another forward model is performed. Each time a new synthetic data set is calculated and compared to an observed data set, a process known as iteration of the inversion.

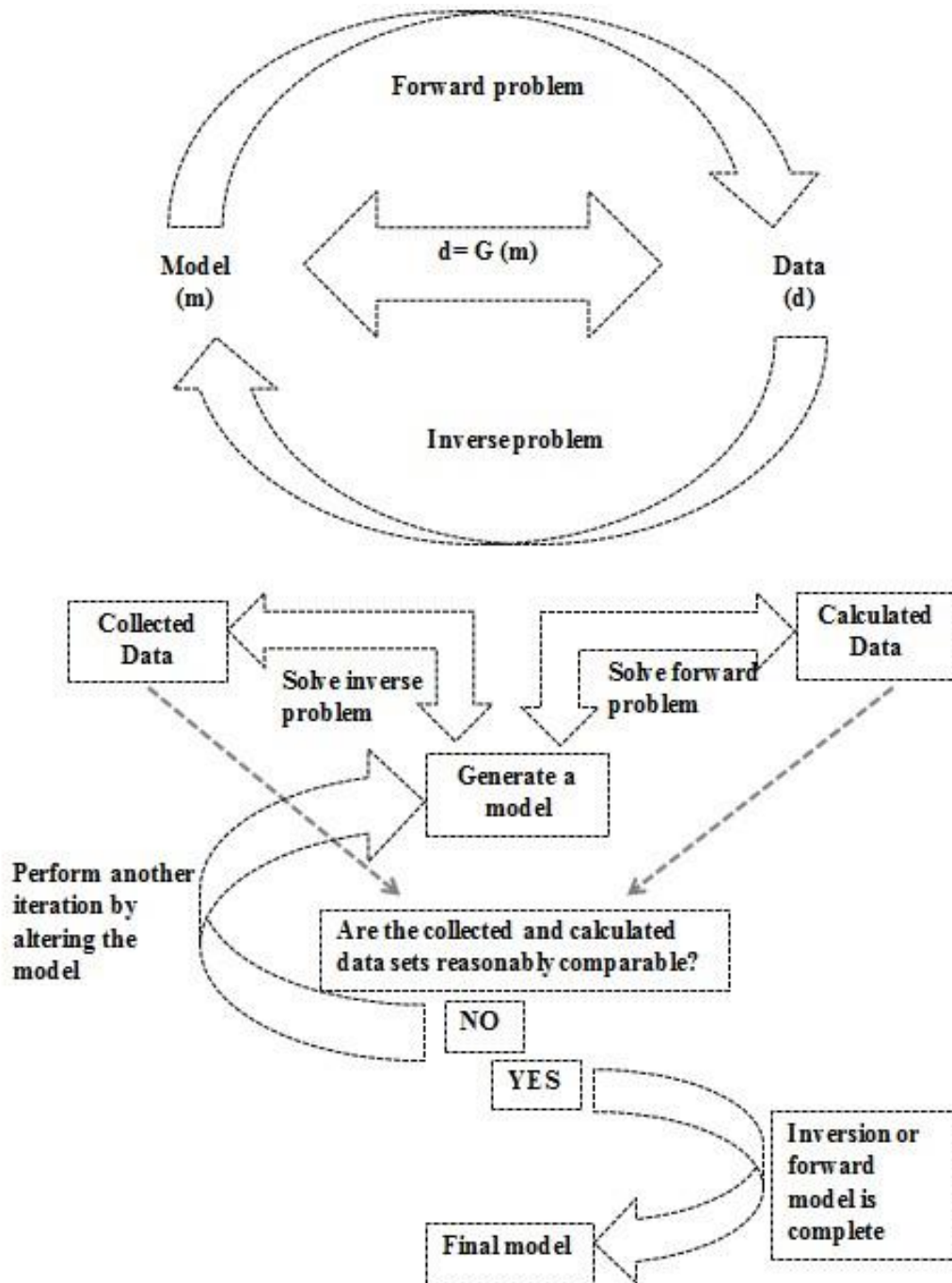


Fig. 3.8: Schematic showing a flow chart of geophysical data inversion and forward modeling process, where the collected data (d) and the model (m) of a physical property are related by a mathematical function (G). Using a model to calculate a synthetic data set is known as solving a forward problem and using collected data set to generate a model is known as solving an inverse problem (Modified from Pierce et al., 2012).

3.1.8.3.1 Inversion

In the case of the ERI geophysical method, an inversion of measured apparent resistivity values creates a model of earth resistivity, and a method of calculating the resistivity values from a certain measurement configuration is pivotal in the inversion process (Sjödahl, 2006). The calculation of resistivity values to produce an earth model is referred to as forward modeling. In 2D forward modeling the subsurface resistivity distribution is given by a 2D model with an infinite extension in the third direction (Sjödahl, 2006). However, it is important to realize that the current electrodes are usually modeled as 3D sources; otherwise they would be mistakenly described as line electrodes. Therefore, 2.5D is occasionally used for this kind of modeling.

In an inhomogeneous ground, forward modeling seeks to find a solution to the current flow equations for a given resistivity distribution and current source configuration (Sjödahl, 2006). The solution comprises the potential field in the 2D section of interest, from which the apparent resistivity values can be computed from the potential electrodes with ease. The flow of current in the subsurface is governed by Ohm's law (equation 3.6)

$$\mathbf{J}=\sigma\mathbf{E}.....(3.6)$$

Where \mathbf{J} represents the current density, σ is the electrical conductivity, and \mathbf{E} is the electric field. The electric field is the gradient of a scalar potential V , given in equation 3.7.

$$\mathbf{E}=-\nabla V.....(3.7)$$

When there are no sources and sinks, the divergence of the current density goes to zero (equation 3.8)

$$\nabla\mathbf{J}=0(3.8)$$

Combining equation 3.6 and equation 3.7 give rise to equation 3.9.

$$\mathbf{J} = -\sigma \nabla V \dots\dots\dots (3.9).$$

Rewriting equations 3.8 and 3.9 give rise to equation 3.10.

$$\nabla(-\sigma \nabla V) = 0 \dots\dots\dots (3.10).$$

Equation 3.10 represents Poisson's equation when there is no source term (Sjödahl, 2006). When there is a point source (current electrode), a Dirac delta function and a point current, I , can be used to describe the divergence of the current density (Coggon, 1971), as shown in equation 3.11.

$$\nabla \mathbf{J} = I \delta(\mathbf{r} - \mathbf{r}_s) \dots\dots\dots (3.11).$$

Where, I , represents the current intensity at \mathbf{r}_s . The electrical flow in inhomogeneous ground is therefore governed by equation 3.12, which is a result of the modification on Poisson's equation using the above given description of point sources.

$$\nabla(-\sigma \nabla V) = I \delta(\mathbf{r} - \mathbf{r}_s) \dots\dots\dots (3.12)$$

In case of 2.5D approximation, the potential is given in 3D because of the 3D point source, but the resistivity is constant in the strike direction, or the y-direction that is perpendicular to the layout orientation. This enables calculations to be simplified into pseudo-2D by placing the source at $y=0$ and applying the Fourier cosine transform with respect to the y-coordinate (Coggon, 1971; Bing & Greenhalgh, 1999; Sjödahl, 2006).

The Poisson's equation (equation 3.12) for full 3D or the Fourier transformed equation for 2D is then solved numerically by partitioning the subsurface into a number of finite elements and solved by matrix inversion techniques (Sjödahl, 2006). The commonly used numerical methods are the finite element and the finite difference methods. The Res2dinv software used for the inversion of the embankment dam measurements in this thesis has an

option of choosing between these two methods. However, the finite element method was preferred due to its flexibility in arranging the cells in datasets with topography.

The inversion routine uses a homogeneous starting model of the subsurface with logarithmic averages of the measured apparent resistivity values (Loke & Barker, 1995). In the inversion routine, the subsurface is divided into a large number of rectangular cells and the optimization method of the user's preference seeks to determine the resistivity distribution of the cells that minimizes the difference between the calculated and measured apparent resistivity values (Loke et al., 2003; Sjö Dahl, 2006; Ganse, 2008). Equation 3.13 is solved in the inversion procedure.

$$(\mathbf{J}_i^T \mathbf{R}_d \mathbf{J}_i + \lambda_i \mathbf{W}^T \mathbf{R}_m \mathbf{W}) \Delta \mathbf{r}_i = \mathbf{J}_i^T \mathbf{R}_d \mathbf{g}_i - \lambda_i \mathbf{W}^T \mathbf{R}_m \mathbf{W} \mathbf{r}_{i-1} \dots \dots \dots (3.13).$$

Where \mathbf{g}_i is the data misfit vector containing the difference between the logarithms of the calculated and the apparent resistivity values, \mathbf{J} is the Jacobian matrix of partial derivatives, $\Delta \mathbf{r}_i$ is the change in the model parameters for the i^{th} iteration and \mathbf{r}_{i-1} is the model parameters vector for the previous iteration, containing the logarithm of the model resistivity values and \mathbf{W} is a first-order roughness filter (deGroot-Hedlin & Constable, 1990). The damping factor determines the relative importance given to minimizing the model roughness and the data misfit (Sjö Dahl, 2006). \mathbf{R}_d and \mathbf{R}_m are weighting matrices introduced to modify the weights given to the different elements of the data misfit and model roughness vectors. The L_1 - or L_2 -norms can be used to minimize the data misfit and the model roughness by adjusting the form of these weighting matrices. A detailed description of the inversion process is given in Farquharson & Oldenburg (1998); Loke & Dahlin (2002); Loke et al. (2003).

According to a description given by Loke et al. (2003), the L_1 -norm minimizes the sum of the absolute values of the data misfit, whereas the L_2 -norm minimizes the sum of the squares of the data misfit. In this thesis, L_1 -norm optimization was chosen for the inversion of embankment dam time-lapse datasets. This optimization method does not only perform well with noisy data, but also produces models with regions that are blocky with sharper boundaries between the dam zones (Claerbout & Muir, 1973). Sharper boundaries between dam zones probably relates to measurements acquired on

embankment dams, where there is usually large resistivity contrast between different materials that make up the embankment, as well as between the embankment and the foundation materials (e.g., between the clay core and the igneous/or metamorphic rock foundation).

3.1.8.3.2 Time-lapse inversions

Time-lapse inversions seek to link inversions of different data sets acquired at different time periods. A smoothness constraint is applied in both the spatial and temporal variation between data sets, and focuses the difference between the data sets on the actual change in the model and suppresses artifacts due to the resistivity structure (Loke, 2001; Sjö Dahl, 2006; Hayley et al., 2011). Time-lapse inversion also takes into account the fact that in many cases the changes in the resistivity occur in limited areas of the subsurface while the rest of the subsurface has insignificant changes. Thus the modifications in the optimization equation (equation 3.13) are such that the difference in the logarithm of the model resistivity values of the initial and the subsequent datasets is reduced (Sjö Dahl, 2006). Equation 3.14 is the modified optimization equation.

$$(\mathbf{J}_i^T \mathbf{R}_d \mathbf{J}_i + \lambda_i \mathbf{W}^T \mathbf{R}_m \mathbf{W}) \delta \mathbf{m}_i^k = \mathbf{J}_i^T \mathbf{R}_d \mathbf{g}_i - \lambda_i \mathbf{W}^T \mathbf{R}_m \mathbf{W} \mathbf{m}_{i-1}^k - \beta_i \lambda_i \mathbf{V}^T \mathbf{R}_t \mathbf{V} (\mathbf{m}_{i-1}^k - \mathbf{m}_{i-1}^0). \quad (3.14)$$

Where \mathbf{m}_{i-1}^0 and \mathbf{m}_{i-1}^k are the model parameter vectors for the initial dataset and k^{th} time dataset. The additional term $\beta_i \lambda_i \mathbf{V}^T \mathbf{R}_t \mathbf{V} (\mathbf{m}_{i-1}^k - \mathbf{m}_{i-1}^0)$, on the right hand side of equation 3.14 constrains the change in the model for the k^{th} time dataset in way that minimizes the difference between the model resistivity values for the k^{th} time dataset model and that of the initial time dataset i.e. when used as the reference model (Sjö Dahl, 2006). β is the relative weight given to the cross-model constraint and \mathbf{V} is the cross-model weighting matrix that is to be introduced in the differences in the model resistivity values. As an example, a study by Lines & Treitel (1984) shows that if a simple damped cross-model constraint is used, the \mathbf{V} is the identity matrix \mathbf{I} . \mathbf{R}_t is the weighting matrix used to modify the weights given to the different elements of the model difference vector such that the L_1 - or L_2 -norm can be used (Farquharson & Oldenburg, 1998). If it is known that there are gradual changes with time in the model resistivity

values, then the L_2 -norm constraint can be used. On the other hand, the L_1 -norm is more appropriate if the abrupt changes in relation to the monitoring interval are expected. The resistivity varies in a cyclic manner over a year in embankment dams, therefore the reference dataset can be chosen as either the initial or the median dataset when evaluating datasets from different time steps in dams over the entire selected period (Sjödahl, 2006).

An approach of inverting the ratio of initial and subsequent datasets proposed by Daily et al. (1992) is useful in highlighting areas of electrical resistivity change in a model. LaBrecque & Yang (2001) successfully developed a difference approach which minimizes the misfit between the difference in two datasets and the difference between two model responses. A considerable amount of work has been done by several researchers in inversions of later time datasets using an initial dataset inversion result as a reference model (e.g., Loke, 2001; Oldenborger et al., 2007; Milner et al., 2008; Kim & Cho, 2011). In this thesis, inversions of the different data sets were carried out simultaneously, with the initial dataset result used as a reference model.

3.1.9 Data interpretation

Having shown in section 3.1.3 that different materials may have similar resistivity values, there is always an element of uncertainty in interpreting resistivity data by attributing the resistivity values to specific types of materials. However, interpretation of resistivity data can be more reliable only after evaluating detailed information about the distribution of materials in the area under investigation.

Interpretation of the final resistivity model is based on understanding and knowledge of the factors associated with the resistivity measurements. The factors that may affect the final inverted resistivity model of the subsurface are:

- ❖ Resolution at the side of the model: there are usually less data points at the sides of the final model, and the model may be affected by boundary conditions and the weight assigned to the side blocks during inversion. This problem can be overcome by having the survey line extended beyond the area of interest so as to cover more ground than actually desired in the final earth model. However,

increasing the survey line always proves to be challenge on embankment dams because most embankments connect to a spillway at one end and a concrete structure at the other end.

- ❖ Ambiguity: resistivity data interpretation suffers from non-uniqueness arising from the problems of equivalence and this is usually exemplified for a case of a homogeneous earth with a high resistive layer embedded in it (Kearey et al., 2002; Sjödaahl, 2006). In the aforementioned situation, the high resistive layer with a given resistivity and thickness may produce the same result as a layer with twice the resistivity and half the thickness (Telford, 1990).
- ❖ High-resistive/high-conductive top layer: a highly resistive top layer makes it difficult to get enough current deeper into the ground. Alternatively, if the top most layer is of high conductivity the current is likely to be channeled in this layer and have difficulties in reaching the underlying structures (Sjödaahl, 2006). These cases can give very small potential readings and as a result, low signal-to-noise ratios.

3.1.10 2D resistivity modeling

In the forward modeling problem, the subsurface resistivity distribution is specified in order to compute the apparent resistivity values that would be measured by a survey over the idealized structures. A forward modeling subroutine is necessary to calculate the synthetic apparent resistivity values for the subsequent model produced by the inversion routine and compared to the measured values for equivalency (to see whether it agrees with the measured). In engineering and environmental surveys, the finite-difference and the finite-element techniques are usually used to calculate the apparent resistivity values for a specified model since the subsurface can have an arbitrary resistivity distribution (Loke, 2001). These methods subdivide the subsurface into a large number of cells, with different resistivity values (Fig. 3.9).

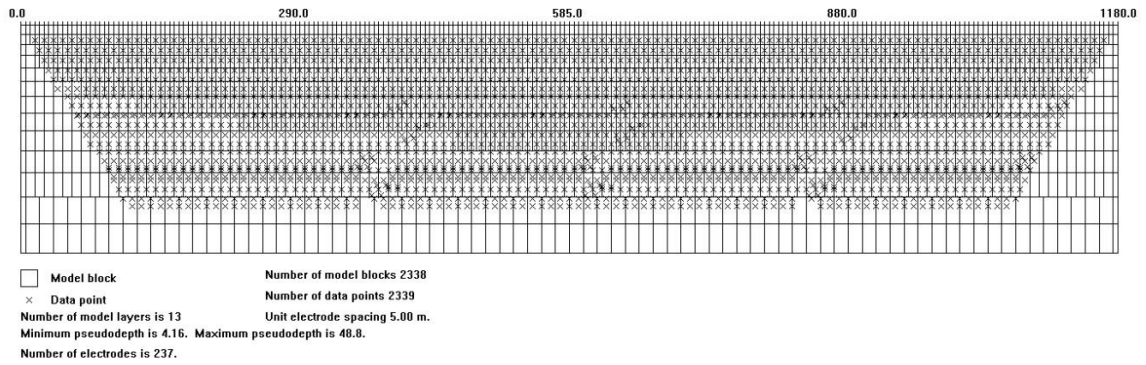


Fig. 3.9: Schematic of a subsurface model divided into a number of cells. The crosses within the cells represent apparent resistivity values of those cells.

The Res2dmod software has both the options of a finite-difference and finite-element methods. With this software, just like in Res2dinv, the subsurface is divided into a large number of rectangular cells and the resistivity values of the individual cells are specified based on the structure desired by the user. The finite-difference technique is based on a method described by Dey & Morrison (1979), with a modification by Loke (1994) on the discretization by area method. This method basically determines the potential at the nodes of the rectangular mesh that consists of L nodes in the horizontal direction and M nodes in the vertical direction (Fig. 3.10). The finite-element method uses the standard first-order triangular elements (Silvester & Ferrari, 1990).

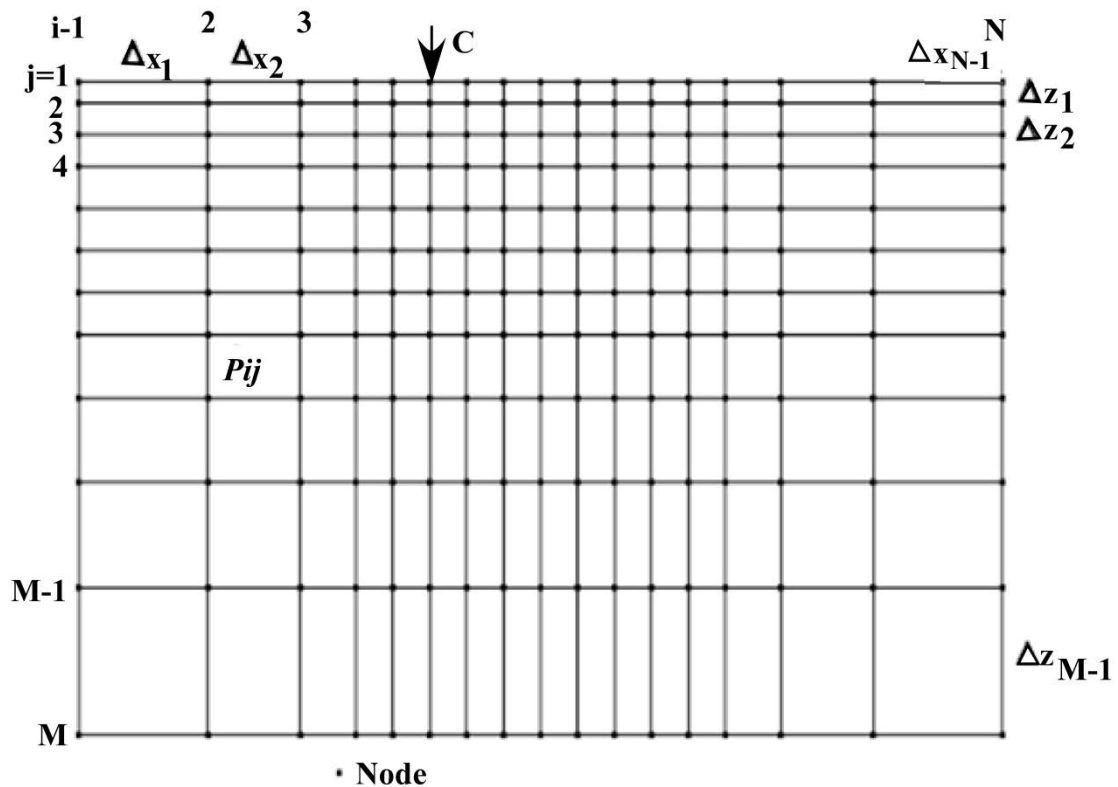


Fig. 3.10: Schematic diagram of the finite-difference or finite-element mesh used by the Res2dmod program (Adapted from Loke, 2002).

While the main focus is on the inversion of field data, the forward modeling technique of 2D resistivity imaging data comes in handy when designing the survey and is also useful during the interpretation stage. In designing the survey, it is understood that different arrays can give different responses to the same structures being investigated (i.e., the arrays sensitivity to structures differ). In theory, from the sensitivity sections we get an idea of the type of array that would give a good response over particular structures (e.g., vertical fracture zone, cavities, etc.). Therefore, forward modeling increases our understanding of the resolution of the method in specific situations. Usually, some information about the shape and size of expected targets is known prior to the field survey. Trying different arrays digitally on a computer before the actual field survey can therefore help in avoiding the use of an array that is not adequately suited for the detection of the structures of interest.

A number of researchers have demonstrated the utility of the forward modeling technique in interpreting of results from case studies using both finite-difference (Mufti, 1976; Dey & Morrison, 1979a, 1979b; Fox et al., 1980) and finite-element method (e.g.,

Pridmore et al., 1981; Queralt et al., 1991; Susaki, 1994; Bing & Greenhalgh, 2001). In forward modeling, a synthetic model over the subsurface resistivity values is created and then a 2D resistivity survey is simulated on this synthetic model (Sjödahl, 2006). Artificial/Gaussian noise can be added to see the effects of random noise in the dataset. The response of each simulated structure is computed, giving a full set of synthetic apparent resistivity values similar to what would be obtained from the actual field data acquisition (Sjödahl, 2006). Forward modeling may be used to validate or nullify the interpretations made based on the measured data. Additionally, forward modeling can be used to estimate the effect of perturbations in the subsurface with time, hence the idea behind the anomaly effect, AE (equation 3.15).

$$AE = \frac{\rho_a(\text{model2}) - \rho_a(\text{model1})}{\rho_a(\text{model1})} \times 100 \dots\dots\dots(3.15)$$

Resistivity anomalies are usually deviations from a smoothly varying background. In modeling, anomaly effect is the percentage change from the comparison of a reference model (model1) and a new model (model2). In addition, evaluation of modeling results can be done on inverted data. The resistivity model can be examined from the synthetic dataset and compared to a real field data model if the objective was to simulate a field situation.

3.1.10.1 Embankment dam modeling

Resistivity modeling in embankment dams can be used to evaluate the effects of different scenarios that commonly occur on dams. Internal erosion and leakage scenarios in dams lead to material changes in some parts of the dam and in the process affecting the resistivity of those materials. Furthermore, seepage increase in compromised zones affects the temperature distribution inside the dam embankment, and as a result, the resistivity in these compromised zones is affected (Sjödahl et al., 2008). Therefore, anomaly effect, calculated for different leakage and internal erosion scenarios may be useful in interpretation of the field data. For situations such as internal erosion within the dam embankment and leakage through the embankment dam cores, modeling can be used to optimize resistivity measurements on embankment dams by:

- ❖ Comparing different electrode configurations on a given survey profile. Different configurations respond differently to dam defects and other factors, therefore, modeling may assist in choosing the most suitable array for the survey.
- ❖ Comparing different positions of survey profiles on embankment dams, there are only three locations in which the survey profiles can be positioned. The upstream and downstream sides of the embankment, which are usually made up of rock fragments, and the third and most realistic survey profile location-the embankment surface directly above the embankment core, usually filled with just the riprap material. Modeling can be used to find the optimal location on the dam surface for embankment dams using surface electrodes (Sjödahl, 2006).

All these measurements are site-specific as the outcome will heavily depend on the actual resistivity model of the subsurface. For an earth-fill embankment dam, the resistivity model is constructed such that it resembles a cross-sectional drawing of the dam under investigation. Different embankment zones are made of different materials and will have different resistivity values. Information about construction materials used is very useful when assigning resistivity values in modeling.

3.2 Frequency domain electromagnetic (FDEM) method

Frequency domain electromagnetic methods utilize the response of the ground to the propagation of electromagnetic fields (Kearey et al., 2002). Many electromagnetic methods developed over the years make use of different transmitters/ receivers, configurations and concepts but the basic physics behind them remains the same (Letellier, 2012). A typical FDEM field set system consists of an electromagnetic loop transmitter and a loop receiver (Figure 3.11), where the transmitter generates a primary electromagnetic field that propagates above and below the ground (Kearey et al., 2002; Brosten et al., 2005). When the primary EM field encounters a conductive material within the subsurface, alternating currents (eddy currents) occur. The subsurface then responds by generating the secondary electromagnetic fields which are detected by the receiver coil through the process of electromagnetic induction. The principles of EM induction as described by Maxwell's equations has been well understood and applied to the EM methods in geophysical prospecting by several authors (e.g., Cantwell, 1960; Grant & West, 1965, as cited in Oskooi, 2004).

Frequency domain electromagnetic methods are used to provide spatially continuous information about the subsurface electrical conductivity variability (Brosten et al., 2005; Minsley, 2012). The FDEM data are mostly presented as apparent resistivity (or conductivity). In the case of dam investigations, possible seepage paths can be located through the identification of high or low conductivity anomalies, where fluid-filled or clay-filled features tend to produce high conductivity anomalies and those filled with air can give low conductivity anomalies (Brosten et al., 2005). EM measurements can also be used to infer subsurface soil types (Dunbar et al., 2003). However, just like the resistivity method (the reciprocal of conductivity), conductivity measurements can also be affected by factors such as porosity, degree of saturation and temperature.

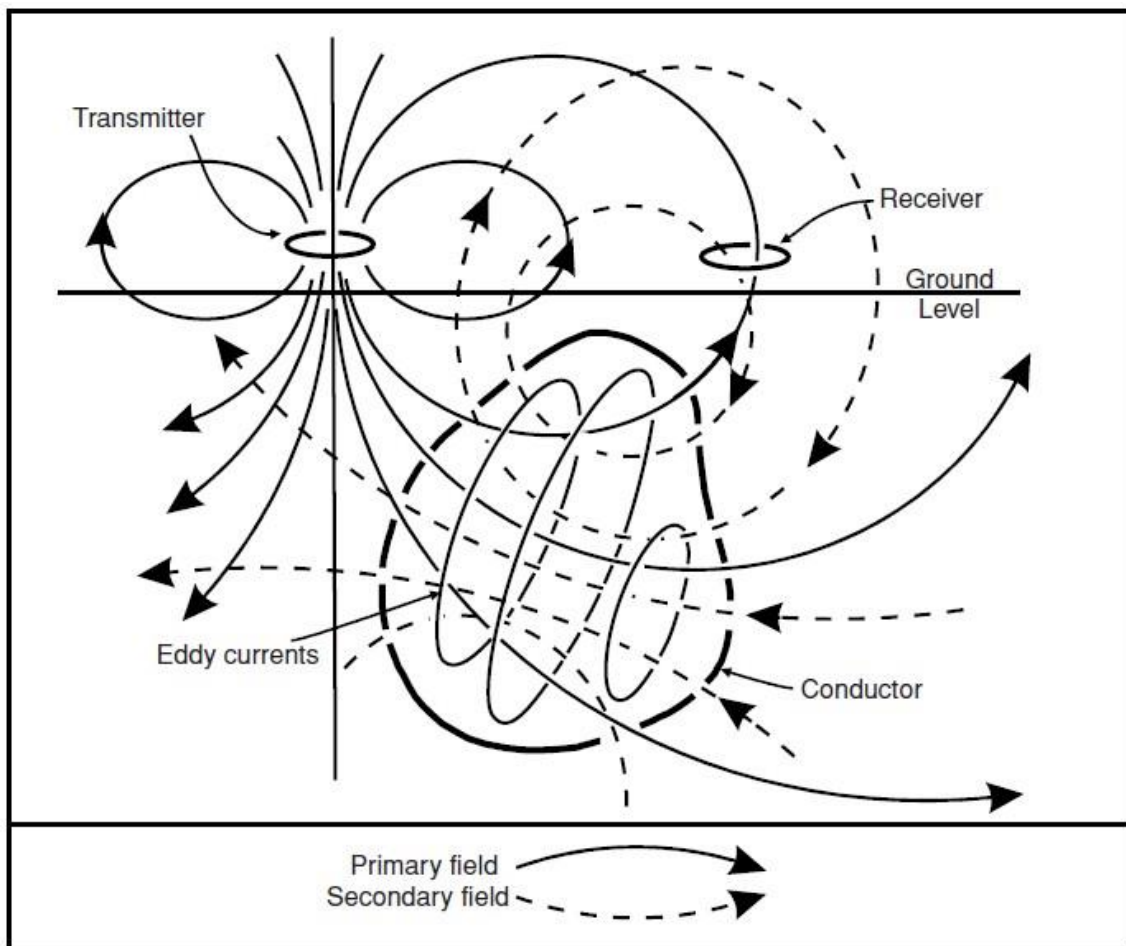


Fig. 3.11: A schematic diagram of frequency domain EM method (Grant & West, 1965, as cited in Reynolds, 2011). Solid lines represent the primary field induced at the transmitter, with the unmodified primary field traveling directly to the receiver via the reference cable and the modified field propagating below the ground to reach the subsurface conductor. The dashed lines represent the secondary field induced at the subsurface conductor by the eddy currents.

3.2.1 Depth of penetration of EM fields

In frequency EM systems, the separation distance between the transmitter (Tx) and the receiver (Rx) is fixed while frequencies are varied (parametric sounding). The depth of penetration (equation 3.16) of plane waves through an isotropic earth depends on the frequency (f) of the waves and resistivity (ρ) of the earth, and is defined by a term skin-depth (δ) such that:

$$\delta = \sqrt{2\rho/\omega\mu} \dots\dots\dots (3.16).$$

Where $\omega=2\pi f$ and μ (Henry/m) is the magnetic permeability of the medium for a homogeneous half-space model. Skin-depth is referred to as the depth at which the amplitude of the EM field is reduced by a factor of e^{-1} compared to its surface amplitude A_0 (Kearey et al., 2002; Letellier, 2012). Multi-frequency EM systems have no direct relationship between the coil separation and the depth of investigation; instead, the depth of investigation is more a function of frequency (Letellier, 2012). Different frequencies can penetrate the ground at different depths and conductivity can then be measured down to the depth of investigation of each frequency. Based on equation 3.16, investigating deeper structural features requires lower frequencies, and for a primary field of a given frequency the induced EM field penetrates to a larger depth in a more resistive medium (Oskooi, 2004).

3.2.2 EM data inversion

Over the years, FDEM measurements relied mostly on anomaly identification through signatures and interpretation done qualitatively (Brosten et al., 2005). Such interpretations were based on the nature of the secondary field components relative to each other. A large ratio of Re/Im indicates a better conductor (Kearey et al., 2002). The vertical model profiles generally have the in-phase and quadrature signals being zero far from the conductor and at places where either the transmitter or receiver are directly over the conductor (Telford et al., 1990). This enables the outline of a buried conductor to be mapped. The signal should rise to a positive peak on both sides and falls to a negative peak over the middle of the conductor when the spread of the transmitter and the receiver straddles the conductor (Telford et al., 1990; Lowrie, 2007). According to Telford et al.

(1990), the profiles over vertical conductors should be entirely symmetrical, that is, the traverse could be reversed without affecting the shape. However, in order to provide both qualitative and quantitative information about the subsurface resistivity structures EM data must be inverted to transform the frequency data into the true distribution of resistivity values with depth in the subsurface. The inversion process involves gathering depth, geometry and stratigraphy from datasets such as resistivity, conductivity, magnetic susceptibility, etc. For an inversion to successfully determine geophysical properties it requires a forward model. Forward modelling generally requires an input of parameters that can define a geological model. In multi-frequency EM forward modelling these parameters include the number of layers, layer resistivity, layer thickness and the weights in the modelling process (Letellier, 2012). The resulting model is used by the inversion program as a guide when processing the multi-frequency EM data. The inversion algorithm creates its own model based on the measured frequency EM data. The program seeks to improve the closeness of the inversion model and the forward model by iteration. The resultant model is deemed appropriate when the forward and inversion models are similar. In this study, an EMINV computer program was used to invert the multi-frequency dataset.

4 Electrical resistivity imaging on embankment dams

The main aim for electrical resistivity imaging on embankment dams is to check the integrity and safety of the dam (Sjödahl, 2006). This is done by investigating potential weak zones, anomalous seepages or internal erosion processes. In this section, some fundamental principles concerning embankment dam inspection are discussed, a brief review of how the resistivity method has been used in dam investigations, a discussion on resistivity variations in dams is also given and lastly, the fundamental basis for evaluation of investigation data is discussed.

4.1 Monitoring and inspection

Embankment dams investigations using resistivity measurements can be achieved in two different ways. Firstly, there are surveys conducted at one occasion or on a limited number of occasions over a limited time frame. Secondly, there is a long-term monitoring with permanently installed electrodes. One-time investigation is the most common approach of inspecting dams, but it is not sufficient when intended to answer the crucial questions about the safety and integrity of the dam being examined. The main focus in this thesis is on repeated measurements on regular basis over a period of twelve (12) months. This approach is based on the time variation of resistivity data due to factors such as seasonal variation in temperature and reservoir levels (Sjödahl, 2006). Once the normal resistivity variation in the dam is established, any deviations from normal resistivity variation are considered to indicate anomalous conditions in the dam.

4.2 Previous work

Time-lapse resistivity measurements have been performed to check the integrity of embankments or to detect anomalous seepage from the dam embankment or the foundation. The resistivity method has been used by Osazuwa & Chi (2010) around the periphery of an artificial lake in the Precambrian basement complex to investigate the subsurface seepage conditions and weak zones. The findings of their study suggested possible seepage conduits for water flow in the zones identified to be intensely weathered.

The resistivity method has similarly been used to map bedrock channels and subsurface pipes (e.g., Chen et al., 1996; Ramage et al., 1998; Gilson et al., 2000; Vickey & Hobbs, 2002). In most cases, the resistivity method has been used together with other geophysical techniques. Butler & Llopis (1990) and Johansson (1997) emphasized on the significance of using integrated geophysical investigations and also recommended the use of repeated measurements to monitor dams, where geophysical anomalies can be identified as a function of time. Such repeated measurements have also been performed by Johansson & Dahlin (1996) to monitor seepage in an earthen embankment dam, and the results from their measurements indicated a seasonal resistivity variation due to the seepage flow through the dam. Lin et al. (2013) acquired periodic resistivity measurements on the downstream of an earth fill dam to investigate abnormal seepage, which had appeared after the dam was reconstructed to raise the maximum reservoir water level. The results of the three 2D ERT survey deployed revealed possible underground pathways of anomalous seepage. Additionally, seasonal resistivity variations related to the ongoing internal erosion process inside two Swedish embankment dams investigated by Sjö Dahl et al. (2008) were observed, through daily resistivity measurements.

4.3 Resistivity variation in embankment dams

Applications of geophysical methods in dam seepage and safety assessment are two-fold. There are methods which are directly sensitive to seepage, and are therefore, used as primary methods. Some methods are indirect, and may be sensitive to either a phenomenon that is a result of seepage or sensitive to a phenomenon that is a circumstance that initiates seepage, and are therefore referred to as secondary methods. The resistivity method is considered to be in both primary and secondary (Sjö Dahl, 2006), as it is directly sensitive to flowing water and may also indirectly detect seepage by detecting seepage channels regardless of the presence or absence of water flow.

The use of resistivity method to directly detect seepage is based on the fact that seepage water introduces a seasonal resistivity variation which may be recorded by repeated measurements, whereas the changing electrical properties of the construction materials caused by internal erosion is the basis of the indirect detection capability of the resistivity method.

4.4 Internal erosion and resistivity properties of soils

The construction materials in embankment dams can be expected to have different resistivities. Fresh metamorphic basement rock should generally have very high resistivity values of around 1000 Ωm or greater, but can have significantly lower resistivity values in fractured, weathered or mineralized zones (Sjödahl, 2006). The clay core should have relatively low resistivity values, below 100 Ωm in most cases due its finer particles. The filters of the dam, flanking the core, should have slightly higher resistivity values than the core if not water saturated. If saturated, however, the resistivity of the filter depends on that of water. The influence of the filter zone on the resistivity measurements on embankment dams is small, given its small volume in between the core and the fill. The support fill is usually made of rock-fill, therefore should have high resistivity values of approximately 1000 Ωm , or greater, on the downstream side of the dam. However, the upstream support fill should have much reduced resistivity if saturated by the reservoir water. The extent of the resistivity decrease depends on the porosity of the rock fill and the resistivity of the reservoir water.

Resistivity values of the commonly used embankment dam construction materials are given in Table 4.1. The geoelectrical situation at a dam site is determined mainly by the reservoir water resistivity. Therefore, if one of the construction materials is in the upper part of the resistivity range in Table 4.1, it is most likely that the other materials at the same dam site will also be in the upper part of their intervals, hence keeping the relative difference on a similar level (Sjödahl, 2006).

Table 4.1. Typical ranges of electrical resistivity properties of common embankment dam construction materials based on various publications as referenced in the text.

Dam zone	Construction material	Resistivity
Core	Clay	10-100
Filter	Sand	100-5000
Upstream fill	Rock fill (wet)	100-5000
Downstream fill	Rock fill (dry)	1000-50000
Foundation	Bedrock (metamorphic)	1000-50000
Reservoir	Water	10-1000

The resistivity of the reservoir water has a greater influence on the construction materials inside the dam embankment, especially in coarse grained zones as it governs the electrical conduction in such zones (Sjödahl, 2006). It is, therefore necessary to know about the site conditions before conducting resistivity measurements. Usually, variations in electrical resistivity values along the dam embankment are examined and not paying much attention to the actual resistivity values in dam embankment. Time-lapse measurements make it even easier as in this case the actual resistivity values are less important and changes in resistivity properties of the construction materials over time are analyzed.

Weak zones in embankment dams can take the form of high resistivity anomalies due to internal erosion (Sjödahl, 2006). Internal erosion washes out fine particles of the core material, thereby affecting the resistivity in two ways. Firstly, as finer particles within the core are washed out, the porosity of the core increases. The increase in porosity leads to a decrease in resistivity of the core due to higher water content. Secondly, the loss of fines from the core increases the resistivity. In theory, it is therefore difficult to predict the effect of internal erosion on the resistivity of the dam core and may differ from one dam to another depending on construction materials and the reservoir water resistivity.

Bergström (1998) performed a laboratory test on some Swedish glacial tills used for sealing layers on waste deposits which indicated a significant increase in resistivity when fine particles are washed out. Bergström (1998)'s findings have further been supported by recent research based on theoretical and practical considerations which

concluded that particle sizes up to 0.2 mm are readily transported to the filter face as the leak initiates (Sjödahl, 2006). If the leakage increases, soil particles as large as 5 mm could be washed away by seepage flows (Foster & Fell, 2001). However, the removal of soil particles larger than 0.2 mm does not significantly increase resistivity. Also, in laboratory tests on a clay specimen that is exposed to piping and internal erosion, performed by Burns et al. (2006) using a miniature resistivity setup, the growth of developing pipe was mapped as a high resistive zone, hence proving to be even useful in large scale embankments monitoring.

5 Study site

5.1 Location and physiography

The Lotsane dam (Fig. 5.1) is located along a reach of the meandering Lotsane River about 2 km upstream of Maunatlala village, south-east Botswana (SMEC, 2012). The Lotsane River is a tributary of the Limpopo River which forms the border between Botswana and South Africa (SMEC, 2012). The Lotsane Dam is bounded to the south by steeply sloping Tswapong Hills, which form a prominent range of east trending hills (Carney et al., 1994). From the base of Tswapong Hills, the floodplains of the Lotsane River slope gently northwards, towards the river channel (Geoflux, 2001). A number of small washes and gullies emerging from the Tswapong Hills cut across the floodplains into the Lotsane River, and form coherent drainage channels in the vicinity of the dam (Timberlake, 1980).

The Tswapong Hills are the dominant landform in the area and contrast with an otherwise uneven topography (Geoflux, 2001). The relief in the region originates from Mokgware Hills in the southwest with an average elevation of 1300 m above sea level (asl), Mabeleapodi Hills in the northwest with an average of 1250 m asl and Tswapong Hills at an average of 915 m asl. The Morupule River from the north, the Kamotaka River from the south and the Maitshokwane River in the center form the drainage basin of the western part of the study area and the three rivers confluence just before Palapye to form Lotsane River (Fig. 5.2). Thus, downstream from Palapye, the Lotsane River forms the main drainage (Geoflux, 2001). Between Palapye and Maunatlala the principal tributary of the Lotsane River is the Dikabeya River from the north. Downstream of Lotsane dam the main tributaries are the Tshokana River from the north and Sesulefa River from the south (Geoflux, 2001).

5.2 General geology of the catchment area

The main geological units of the Lotsane catchment are the Basement complex, Waterberg Supergroup, the Karoo Supergroup and Kalahari Beds. According to Carney et al. (1994) the rocks comprising these units vary in age from the Achaean (Basement complex) through the mid to Late Proterozoic (Waterberg Supergroup) and the

Triassic (Karoo Supergroup) and up to the Cretaceous to Recent (Kalahari Beds). Figure 5.2 shows the generalized geology of the Lotsane catchment based on Republic of Botswana Hydrogeological Reconnaissance map sheet 8 (SMEC et al., 2012).

The basement rocks include the granites or granitic gneisses and amphibolites (Key & Jones, 1978). These rocks generally have poor permeability and thus yield water only along fracture systems (Arup Botswana et al., 1991). In the western area of the Lotsane catchment younger rocks and the Kalahari Beds deposits overlie the basement rock, while the meta-sedimentary rocks of the Palapye Group overlie the Basement Complex rocks in the eastern part of the catchment area (Geoflux, 2001). The Palapye Group of rocks form part of the Tswapong Hills and the Ramokgonami-Selika Hills range to the south of Lotsane River and are comprised of mainly quartzites, shales, siltstones and sandstones. The Karoo Supergroup rocks cover most of the central and western parts of the Lotsane catchment and are comprised of sedimentary rocks belonging to the Dwyka, Eccca, and Lebung Groups (Carney et al., 1994).

5.3 Hydrology

The Lotsane River is a sixth order stream with irregular flow which drains a dry, moderately sloping catchment. The Lotsane River is classified as an irregular meandering river (Geoflux, 2001). The catchment lies between 26°18' and 28°12' east longitude and 22°04' and 22°52' south latitude and extends for almost 200 km from west to east and roughly 88 km from north to south (SMEC et al., 2012). The catchment area at the dam site is 6760 km², and the elevation ranges from 1260 m to 838 m. Substantial runoff occurs from the Tswapong Hills, of which about 400 km² drains into the Lotsane River from the south through small steep tributaries between Palapye and Maunatlala. In the central part of the Lotsane catchment, the Maitshokwane River drains from the western portion of the Mokgware Hills, and from the slopes between the Mokgware Hills and Serowe.

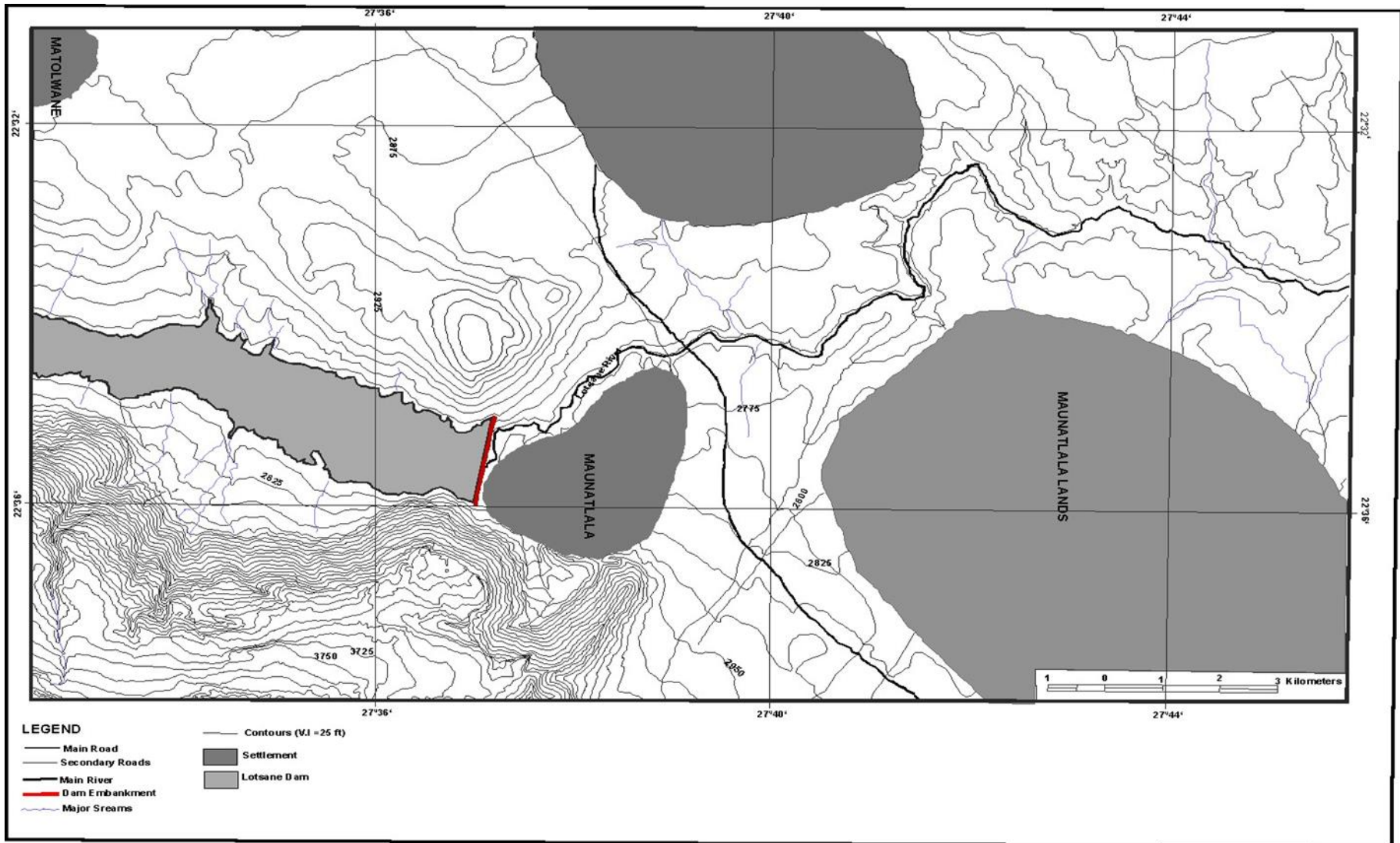


Fig. 5.1: A map showing the topography and the Lotsane embankment dam and settlement areas proximal to the dam. Insert shows the geographic location of the study area (Modified from SMEC et al., 2012).

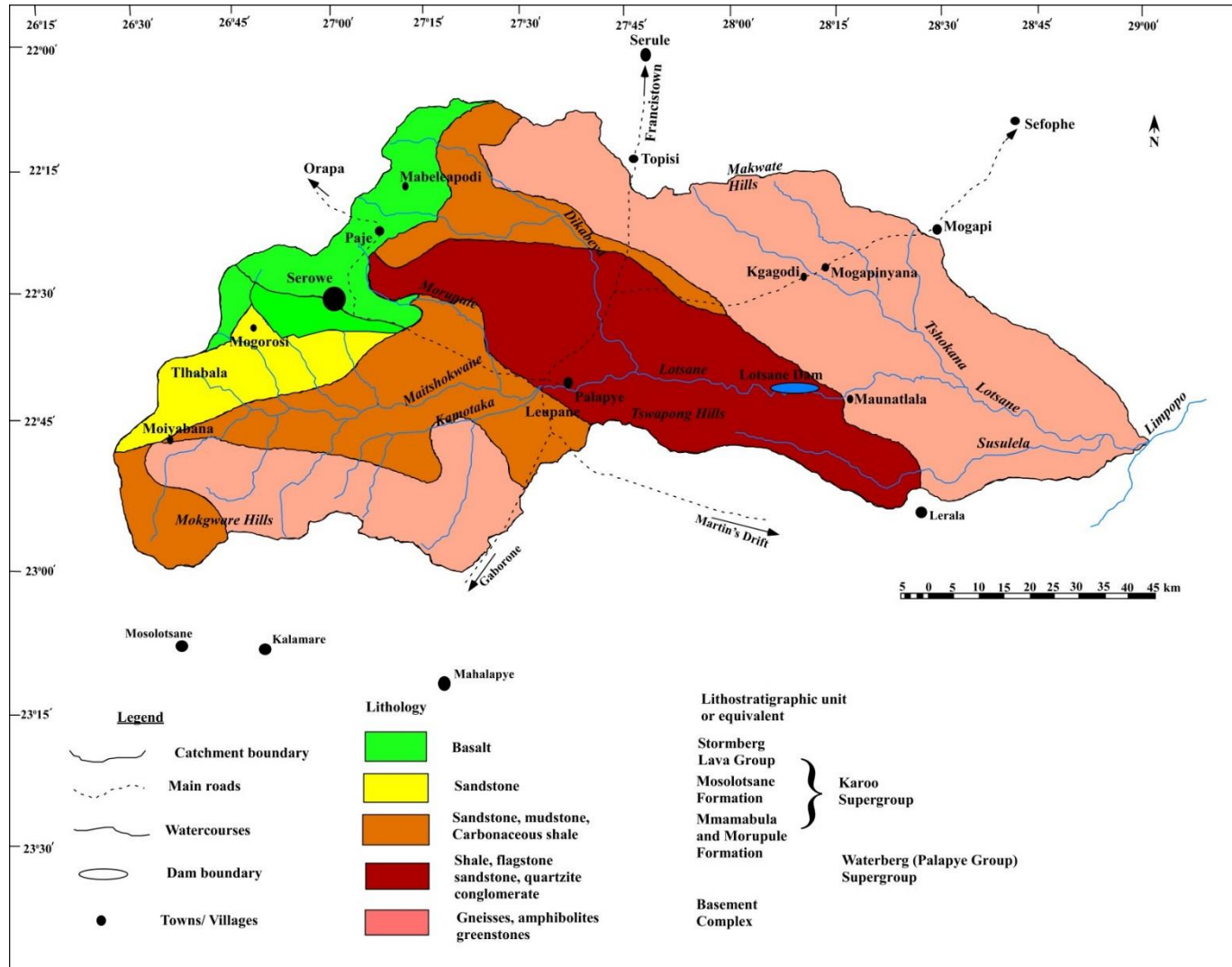


Fig. 5.2: The generalized geology of the Lotsane catchment based on the Republic of Botswana Hydrogeological Reconnaissance map sheet 8 (Modified from SMEC et al., 2012).

5.4 Hydrogeology

The area around Lotsane Dam has the potential of groundwater occurring in discrete fissures that may or may not be interconnected sufficiently to constitute an aquifer (Arup Botswana et al., 1991). Recharge to this aquifer system is by fracture continuity to the surface and is dominant in zones where surface runoff is concentrated, especially in channel sands of the Lotsane River. Recharge to fissures is also provided by runoff from the Tswapong Hills infiltrating towards the valley. Some of the recharge to the fissures is revealed in the form of springs and seepages in clayey alluvium deposits.

5.5 Description of embankment

The entire Lotsane Dam embankment is built on bedrock consisting mainly of gneiss but also of layers and bands of amphibolite. These metamorphic rocks are probably of sedimentary origin but a band of amphibolite to the right of the spillway crest structure is possibly of intrusive origin (SMEC et al., 2012). The bedrock surface is generally highly weathered and the weathering extends to depths in excess of 25 m before either unweathered gneiss or amphibolite is encountered (SMEC et al., 2012). The depth to the moderately weathered rock varies between about 5 m on the upper left flank in the spillway area to 11 m elsewhere on the left flank, about 10 m in the river channel and between 10 m and in excess of 32 m on the upper right flank of the embankment (SMEC et al., 2012).

The deep zone of weathering appears to be associated with faulting, as evidenced by the presence of brecciated faulted rock in some of the boreholes at the dam site during design investigations (SMEC et al., 2012). The entire valley is considered as a fault zone (Fig. 5.3) as indicated on the regional map as the Lechana Fault Zone. Besides the faulting and brecciating the bedrock is generally very closely fractured (SMEC et al., 2012).

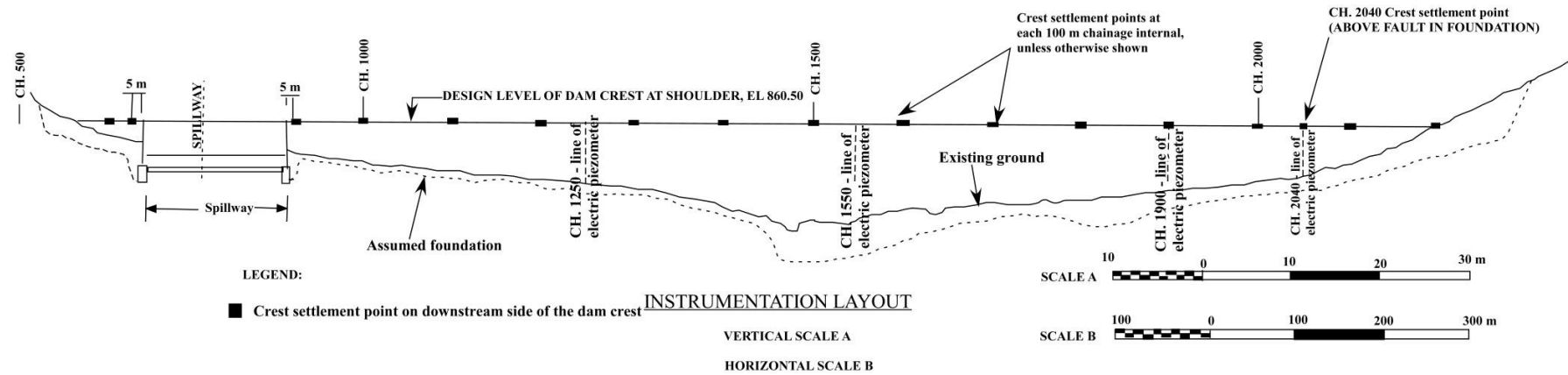


Fig. 5.3: Crest settlement points on the downstream side of the dam embankment installed at 100 m intervals. Also shown is the ground that existed before excavation and removal of the weathered top part of the basement rock to leave behind the fresher basement rock, which forms the foundation of Lotsane Dam. The spillway is located between chainage point 500 m and chainage point 1000 m. Locations of electric piezometers are shown, with the electric piezometer at chainage 2040 m situated directly above the fault zone in the foundation. Chainage refers to the length along the dam in meters. Scale A is meant for depth/ vertical axis whereas scale B is for the horizontal axis (Adopted from SMEC et al., 2012).

5.5.1 Embankment materials

The embankment is made of naturally occurring materials in the form of an impervious clay core, excavated from borrow pits of low organic contents and low liquid limit from an alluvial terrace upstream of the dam. Materials used for the impervious clay core are dispersive in nature (SMEC et al., 2012). Therefore, considerable design efforts were spent on safeguarding the core materials against erosion by adding gypsum to the clay material at the rock foundation interface and by providing a filter zone on the upstream and downstream side of the core, designed to prevent erosion of the core material into the coarser zones of the dam. The shoulder fill was obtained from the excavation of the spillway channel. The embankment also has a grout curtain constructed under the core of the dam to protect the dam from excessive seepage through the foundation, which would otherwise lead to piping and collapse of the dam structure. General arrangement of the embankment sections are shown in Figure 5.4.

5.5.2 Internal zones of the dam embankment

The Lotsane Dam embankment is constructed from the following material zones:

Zone 1A- earth fill core;

Zone 2A- fine filter chimney and blanket;

Zone 2B- coarse filter chimney and

blanket; Zone 2C- riprap bedding;

Zone 2D- drainage material, consisting of fresh and slightly weathered rock uniformly graded between 20 mm and 140 mm;

Zone 2E- riprap and downstream protection filter;

Zone 3A- upstream slope protection, which is riprap consisting of fresh and partly weathered rock less than 1200 mm size;

Zone 3B- downstream slope protection consisting of fresh and slightly weathered rock of variable size;

Zone 4A- random fill consisting of moderately weathered rock and

Zone 4B- random fill, consisting of highly weathered rock or better (granite gneiss).

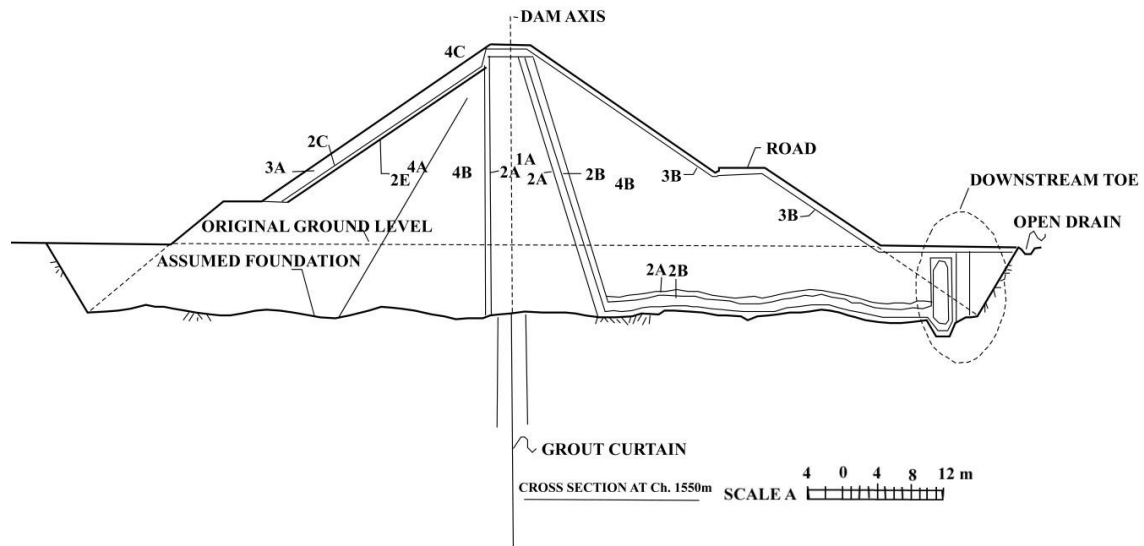


Fig. 5.4: A schematic of the cross section at chainage 1550 m (Fig. 5.3) and the general arrangement of the dam embankment zones, with a vertical upstream side of the slope and a slightly inclined downstream side (Modified from SMEC et al., 2012).

5.5.3 Design and layout of the core zone and filters

The core was designed as a central vertical core of earth fill. The shape of the core in cross-section is such that the width of the core at any elevation is not less than 90% of the reservoir head, taken at full supply level, and was designed in this way to reduce hydraulic gradients, especially in the highly weathered foundation (SMEC et al., 2012). The top of the core is set at an elevation of about 859.2 m and has a width of 3 m. The upstream slope of the core is vertical and the downstream of the core is slightly inclined. Highly weathered random fill material, essentially sand with up to 15% fines occurs on top of the core mainly to help minimize drying cracks in the top part of the core (SMEC et al., 2012). However, this random fill does not provide a highly permeable seepage path over the top of the core as opposed to the finer filter material. The Zone 4B random fill was designed to be sufficiently fine grained to prevent erosion of the Zone 2A filter into the random fill. The coarse filter material in Zone 2B was designed in accordance to the recommendations given by the United States Soil Conservation Service (USSCS) to be compatible with the fine limit of the Zone 2A material. The maximum particle size of the Zone 2B material is 4.75 mm (SMEC et al., 2012).

5.5.4 Lotsane dam instrumentation

Crest settlement and horizontal movement points are provided at 100 m intervals along the crest of the dam and also immediately adjacent to spillway walls to monitor the crest settlement over the long term. Surface movements are monitored at 15 installed survey monitoring points (SMPs) located on top of the parapet wall and at the downstream edge of the crest. A total of 32 electric vibrating wire piezometers are installed throughout the fill and foundation on chainages 1250 m, 1550 m, 1900 m and 2040 m to enable pore water pressure measurements for long-term monitoring of the dam and foundations. Terminal boxes are installed at different location for reading of the electrical piezometers. A total of 20 standpipe piezometers are located in the foundation downstream of the dam embankment, and were installed midway between foundation relief wells to check the water pressure head between the relief wells.

Eighteen foundation relief wells were drilled at 50 m spacing into the rock downstream of the embankment to reduce pore pressures and exit hydraulic gradients in the foundation. There is also a seepage measuring weir constructed at the downstream toe of the dam. A zone 1A cut-off traps seepage water and allows it to be channeled into the measuring chamber. A toe drain collects seepage throughout the length of the dam foundation and channels it towards the measuring chamber. There are also additional measuring points at the downstream end of the left and right spillway walls, where seepage emerges from pipes to enable a record of flow through the core. A drainage system is also placed behind the left and right spillway walls to collect seepage. Figure 5.5 shows some of the instrumentation sets installed in Lotsane Dam for dam condition monitoring.

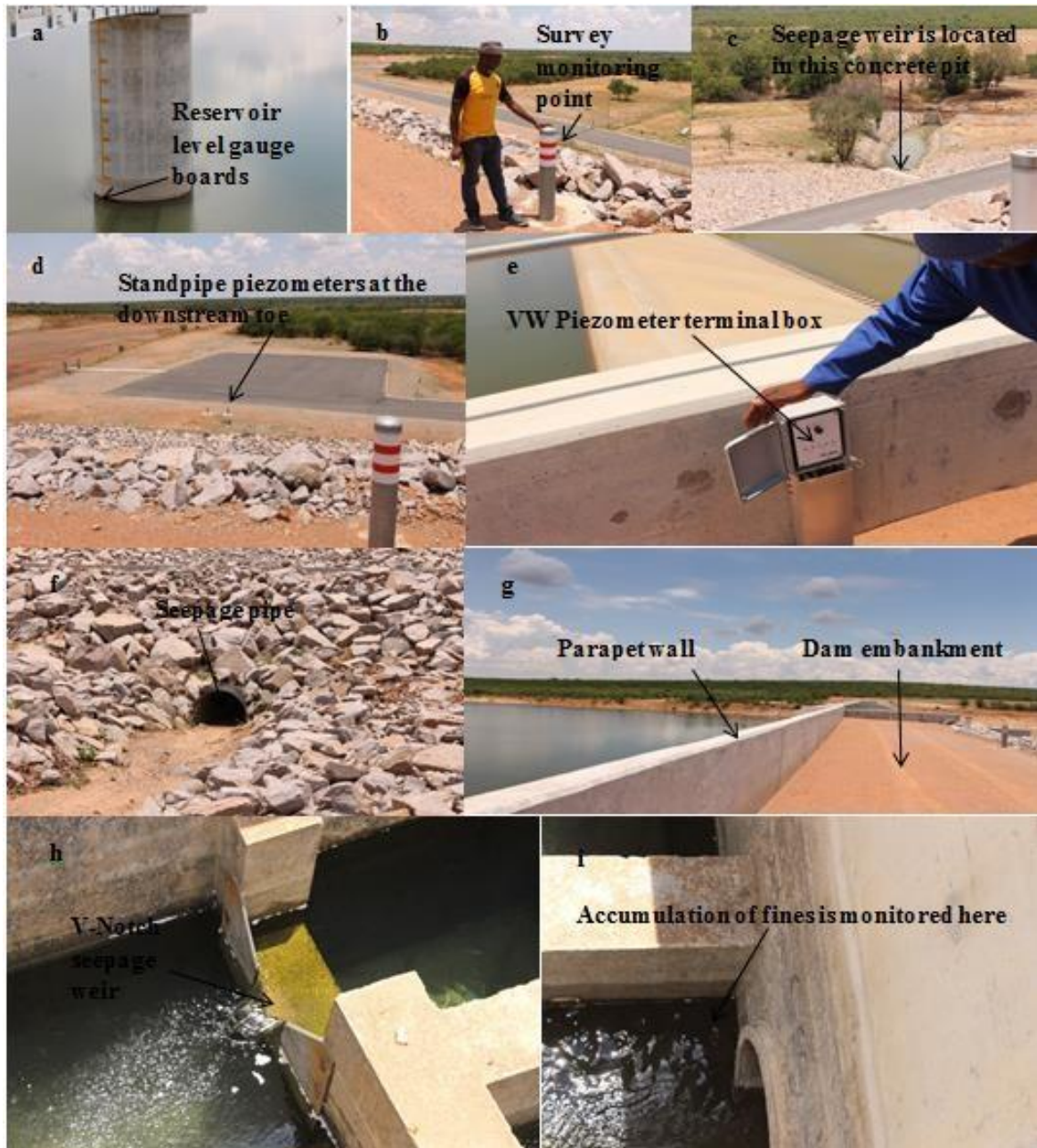


Fig. 5.5: Photographs of the Lotsane Dam showing instrumentation installed during its construction for long term monitoring of the dam conditions: (a) reservoir level gauge installed for reservoir water level monitoring and can be read from the dam crest using a pair of binoculars, (b) survey monitoring point located at the downstream edge of the embankment, (c) location of the seepage weir in a concrete pit, (d) view of standpipe piezometers located at the downstream toe of the dam, (e) vibrating wire (VW) piezometers, (f) seepage pipe to monitor the flow rate and evidence of particle (soil) migration, (g) the dam embankment and the parapet wall, (h) view of the concrete pit where the V-Notch seepage weir is located and (i) the compartment in the seepage weir where the accumulation of fines are being monitored.

6 Data and methods

6.1 Datasets

6.1.1 Electrical resistivity imaging data

During the field survey, we established one resistivity profile on the embankment of Lotsane Dam (Fig. 6.1) and used an array of 48 stainless steel electrodes of 50 cm lengths and 1.3 cm diameters that were planted 10 cm into the ground for good contact. For data acquisition, an Iris Syscal Pro unit was used. The protocol files for the dipole-dipole array were utilized. This electrode geometry is sensitive to horizontal changes in resistivity, hence suitable for imaging vertical structures such as cavities within the subsurface. The dipole-dipole sequence for multi-channel acquisition was optimized by allowing gap filler quadripoles so as to use all the ten acquisition channels and increase the number of data points. A transmitter-current injection time window (T_n) of 500 ms was chosen and 3 to 6 stacks performed with a quality factor (i.e. the standard deviation of the stacked signal) of 3 %.



Fig. 6.1: Photographs showing a 2D resistivity data acquisition setup with 48 stainless steel electrodes planted into the ground (Lotsane Dam embankment) along a straight line, attached to a multi-core cable.

The four imaging cables with 10 m spacing between the electrodes were used for spread array length of 480 m. The data acquisition process is entirely controlled by software. After electrode cables have been hooked up to the electrodes, the program then checks that all electrodes are connected and properly grounded before the actual measurement starts. Thereafter, if adequate contact between the electrodes and the

ground is attained, the software scans through the measurement protocol selected by the user. With the 10 m electrode spacing and a total spread length of 480 m, the maximum depth of investigation (referred to as Max in Fig. 6.2) using the dipole-dipole array is $0.2L$ (96 m) with L being the total length of the spread.

A roll-along technique involving a two segment cable (a and b) was used to cover an embankment length of 1.35 km, whereby one segment (two cables) of 24 electrodes each was moved past the end of the line and this was repeated until the total desired line length was achieved. With this roll along technique, a first sequence of readings was taken with the equipment located in the middle of the segments a and b at station 1 and the second set of readings was then taken with the equipment moved to station 2 using the segments b and a. The maximum depth reached which ensures a continuity of the bottom part of the image is $\frac{1}{2}$ Max (e.g., 48 m). We acquired five data sets over a period of twelve (12) months to monitor changes in the subsurface resistivities using the same measurement protocols. Electrode positions on the embankment were maintained whenever measurements were acquired to minimize errors associated with misplacement of electrodes over time.

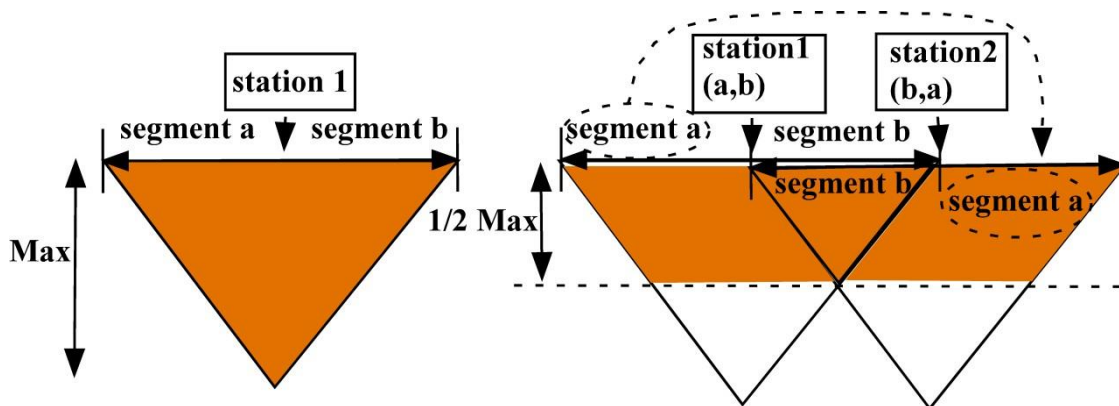


Fig. 6.2: Schematics showing an arrangement of the two segments and the station positions in multi-electrode resistivity measurements for a simple (standard) configuration (left) and a roll-along configuration (right) (Modified from Bernard et al., 2006). The maximum depth reached which ensures a continuity of the bottom part of the image in a roll-along configuration is half the maximum depth of investigation in a standard configuration.

6.1.2 Frequency domain EM data acquisition

Frequency domain EM data was collected using an Iris instrument (the Promis IP), which is a Slingram horizontal loop EM system consisting of a transmitter (Tx) loop, a receiver (Rx) sensor (Fig. 6.3) which measures three in-phase and three out-of-phase components of the secondary field. The Promis system uses ten-frequencies from 110 Hz to 56 kHz, but only seven were used in this study. Measurements were acquired using a 100 m Tx-Rx reference cable, at 10 m station spacing along the dam embankment length (1180 m) for the seven selected frequencies. When traversing, the Tx-Rx spread such that the receiver was ahead of the transmitter along the embankment. The survey was conducted from north to south. The coil was horizontal coplanar and oriented to detect the vertical component. Horizontal loop measures the ratio of vertical secondary to vertical primary magnetic fields at the receiver for the in-phase and quadrature components. Readings are plotted at the Tx-Rx midpoint.

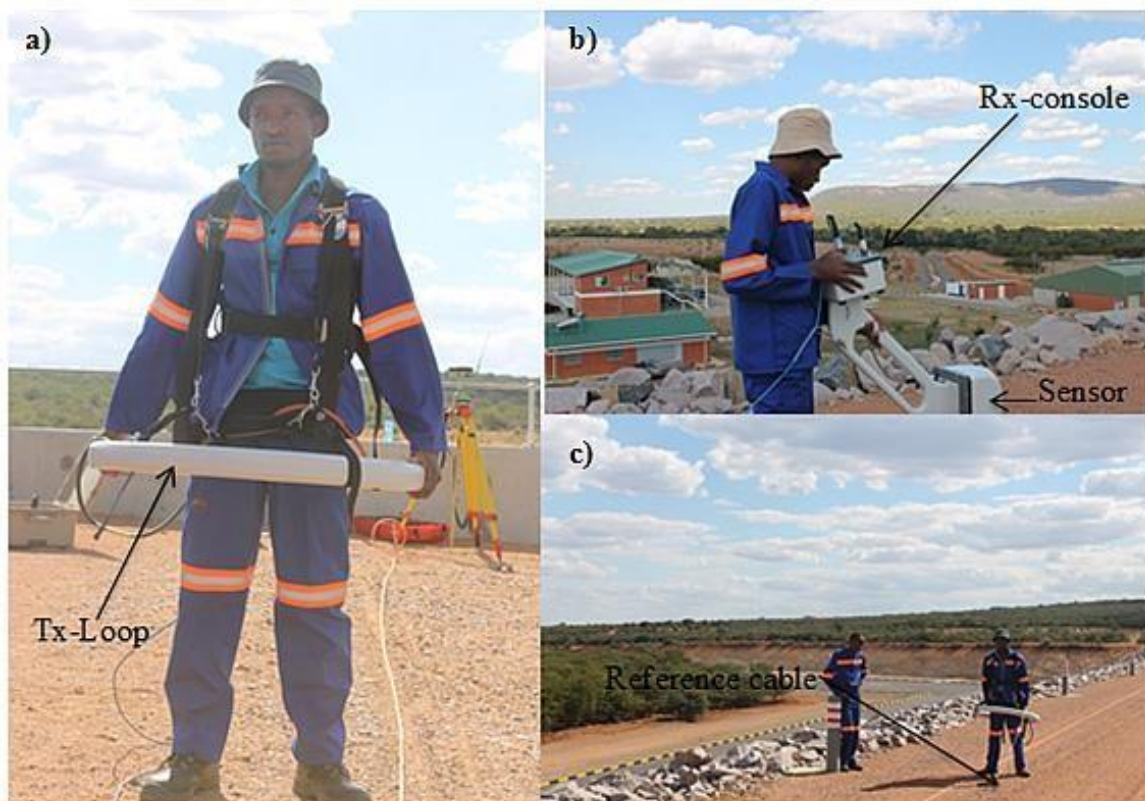


Fig. 6.3: Photos showing the frequency domain electromagnetic equipment set: the Promis IP system consisting of (a) the transmitter loop/coil (b) the receiver console plus the sensor (c) the reference cable or the Tx-Rx link. During data acquisition, the spread was such that the receiver was ahead of the transmitter.

6.1.3 High resolution aeromagnetic data acquisition

Aeromagnetic data were acquired in 1996 by the Botswana Geological Surveys (BGS) Department. The flight elevation of the aeromagnetic data was 80 m along north-south survey lines with line spacing of 250 m (Kinabo, 2007). The tie lines were east-west and spaced at 1.25 km apart. The international geomagnetic reference field model of the core field was subtracted from the observed total field to get the residual total field and the data were gridded (Fig. 6.4) using the minimum curvature technique (Briggs, 1974) with a grid cell size was 62.5 m. Minimum curvature is accomplished by fitting a smoothest possible surface to the data values. Upon request of the data from BGS for use in this thesis, the grid was windowed interactively to remain with a small manageable section covering Lotsane Dam area.

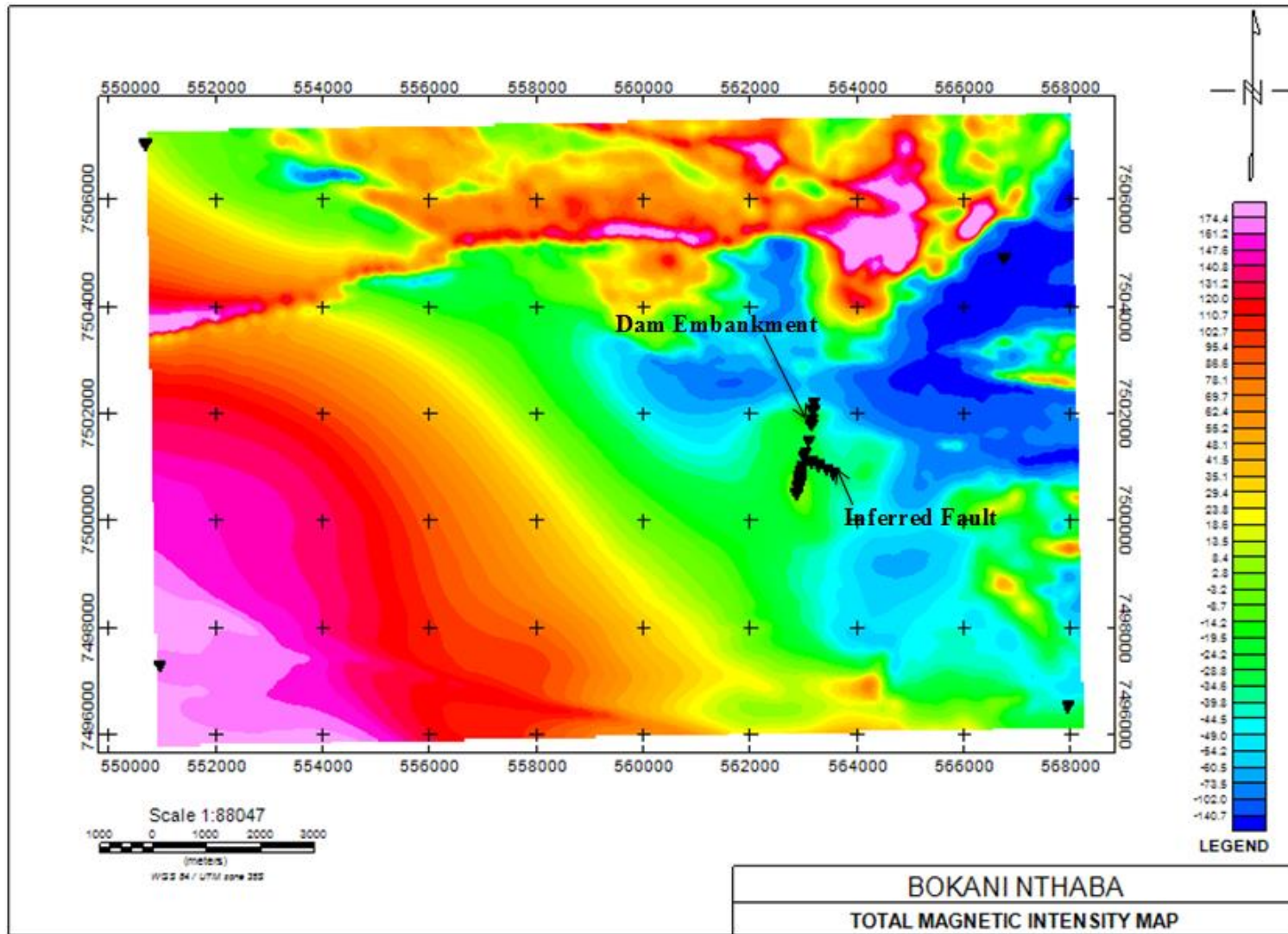


Fig. 6.4: The total magnetic intensity (TMI) distribution map of Lotsane Dam area. Also shown on this map are the dam embankment and a fault line which I inferred from Google Earth satellite images.

6.2 Data processing and analysis

6.2.1 Resistivity data processing and analysis

6.2.1.1 Resistivity data processing

The electrical resistivity data were transformed using the Prosys II software to allow further assessment and editing. The raw data files (*.pro) were read in Prosys II and the first steps of quality assurance were performed. Spurious data points were excluded from the dataset and the topographical data for the profile was added. The raw data file was converted to a *.dat format. Inversion of the data collected in this study was carried out using commercially available Geotomo software; the Res2dinv program developed by Loke & Barker (1995). The measurements taken on the embankment along a line were imported into the Res2dinv program and examined to detect and remove spurious data spikes that would have been missed with the Prosys II software. The measured electrical resistivity values were then inverted, yielding a contoured distribution of apparent resistivity values for the subsurface (Fig. 6.5).

The apparent resistivity measurements were converted to true resistivity values using an iterative numerical inversion that determines a least squares fit to the measured data (de GrootHedlin & Constable, 1990; Loke, 2001). The iteration inversion process was continued until additional iterations did not reduce the error between the actual and synthetic results more than a threshold value or convergence limit, which was set at 1%. A measure of this difference is given as the root-mean-squared (RMS) error. The topography was also taken into account for the mesh construction, but the difference in elevation in the profile was very small, about 0.5 m. We used a robust (L_1 -norm) constraint to calculate the data misfit and the RMS value generally obtained was between 7 % and 10 % with Res2dinv program.

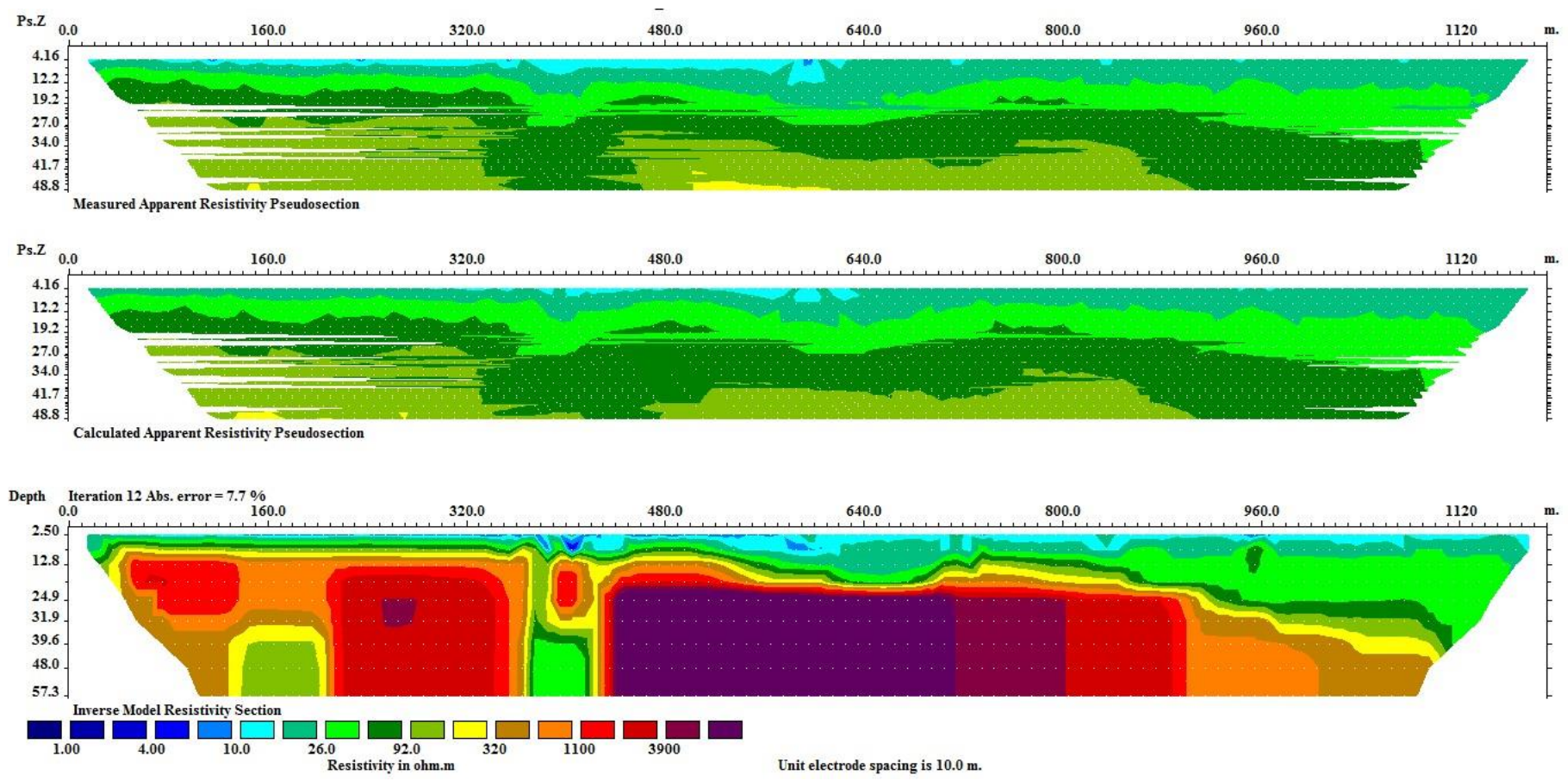


Fig. 6.5: The subsurface resistivity inversion results of the field data for the Lotsane Dam, showing the measured and the calculated pseudo sections plus the resistivity inverse model, with an absolute error of 7.7 %. The y-axis show elevation/depth and the x-axis give the distance along the profile, all in meters.

6.2.1.2 Time-lapse resistivity data inversion

The different datasets (acquired at different times) of the same profile were combined in Res2dinv software. The combination of datasets was such that each data file had two datasets in it, thus allowing for the evaluation of the temporal changes in electrical resistivity. In this study, we employed a simultaneous time-lapse inversion approach of resistivity data inversion on the five datasets (Fig.6.6 to Fig. 6.10) acquired, with a smoothness- constrained least-squares inversion method (deGroot-Hedlin & Constable, 1990). Unlike the independent time-lapse inversion (Appendix A), the inversion of the initial dataset and the inversion of the subsequent datasets were performed simultaneously and constraints of smoothness and closeness to a reference model were applied to the difference image produced at each iteration, with the constraints being updated at each iteration (Haley et al., 2011). This approach has in many cases given satisfactory results (Loke, 1999).

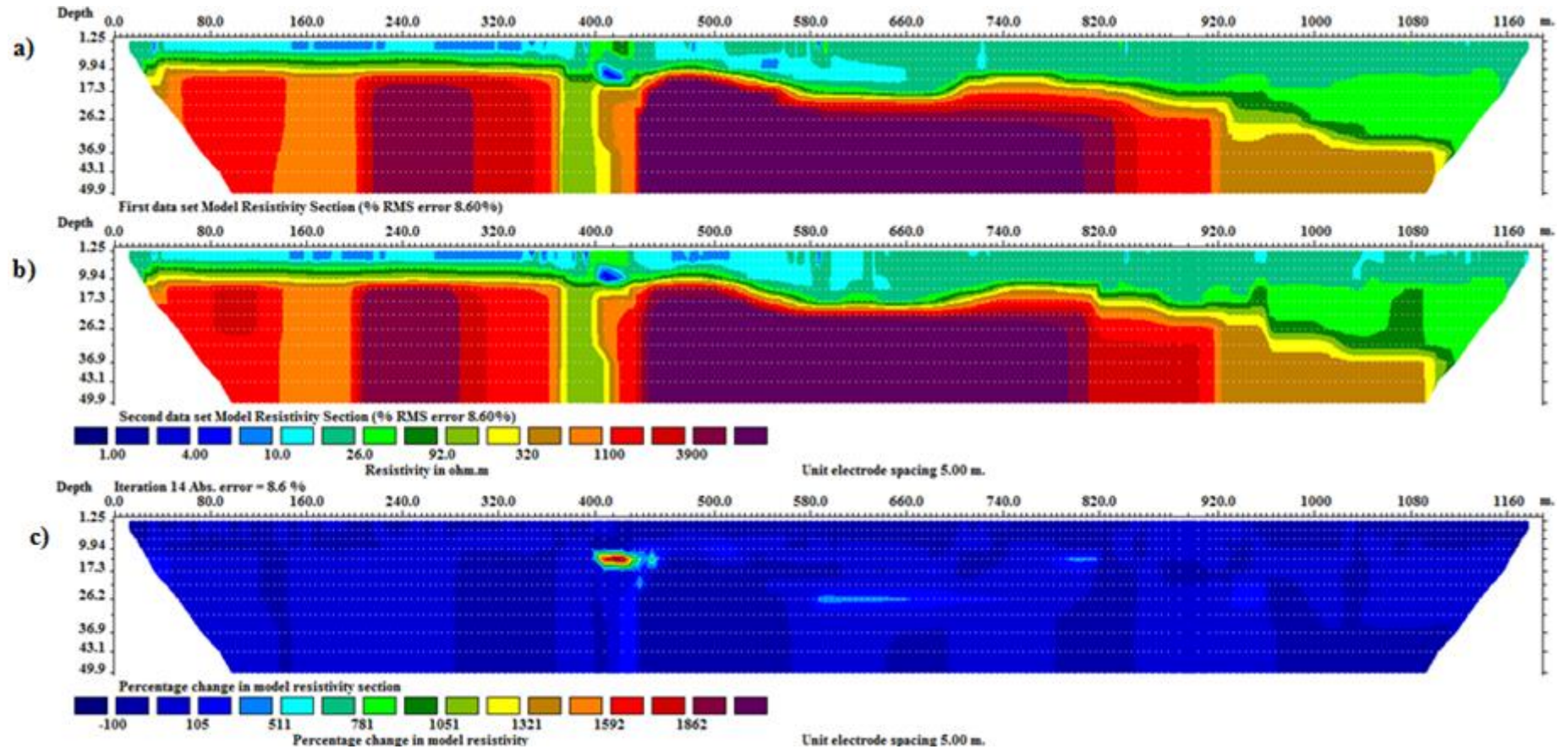


Fig. 6.6: (a) An inverse resistivity model from the initial dataset, acquired on the 27th October 2015 (b) the inverse resistivity model from the second dataset acquired on the 15th December 2015 (c) the difference model from the two datasets, showing the percentage change in model resistivity sections with an absolute error of 8.6%.

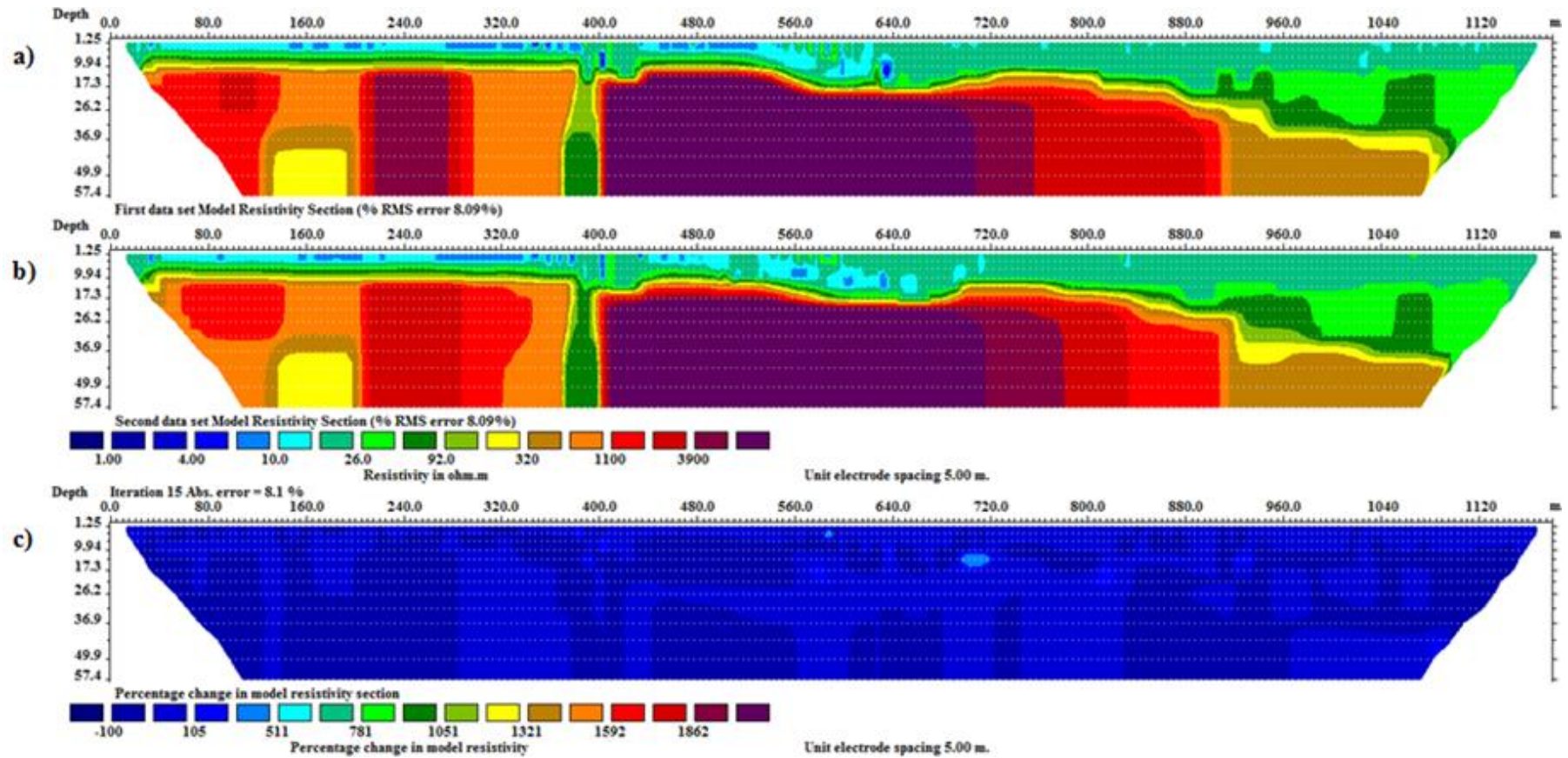


Fig. 6.7: (a) Inverse resistivity model second dataset, acquired on the 15th December 2015, (b) the inverse resistivity model of the third dataset, acquired on the 5th March 2016, (c) the percentage change in model resistivity sections with an absolute error of 8.1 %. The resistivity models shown are based on a dipole-dipole array.

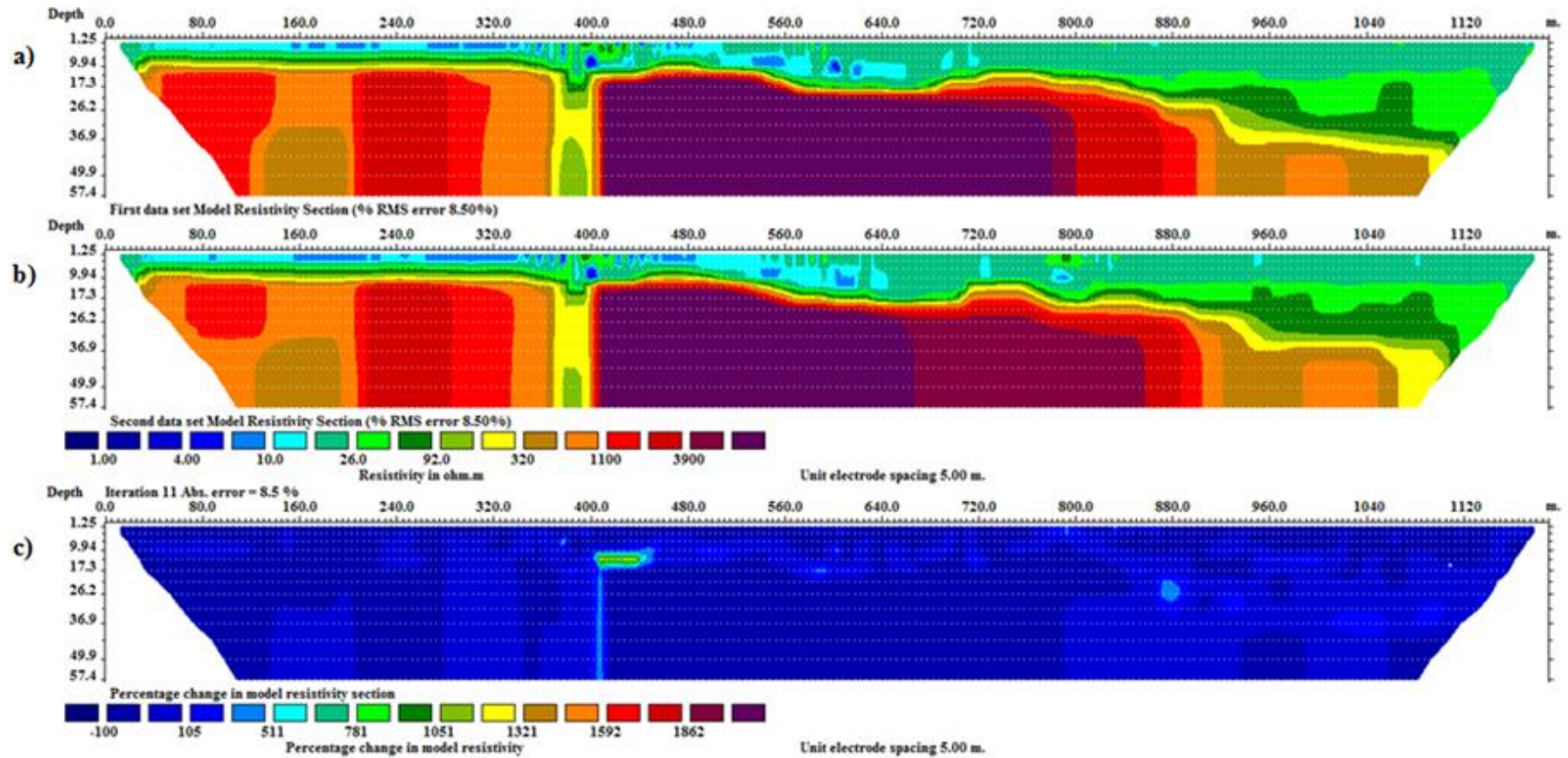


Fig. 6.8: (a) Inverse resistivity model third dataset, acquired on the 5th March 2016, (b) the inverse resistivity model of the fourth dataset, acquired on the 25th May 2016, (c) the percentage change in model resistivity sections with an absolute error of 8.5 %. The resistivity models shown are based on a dipole- dipole array.

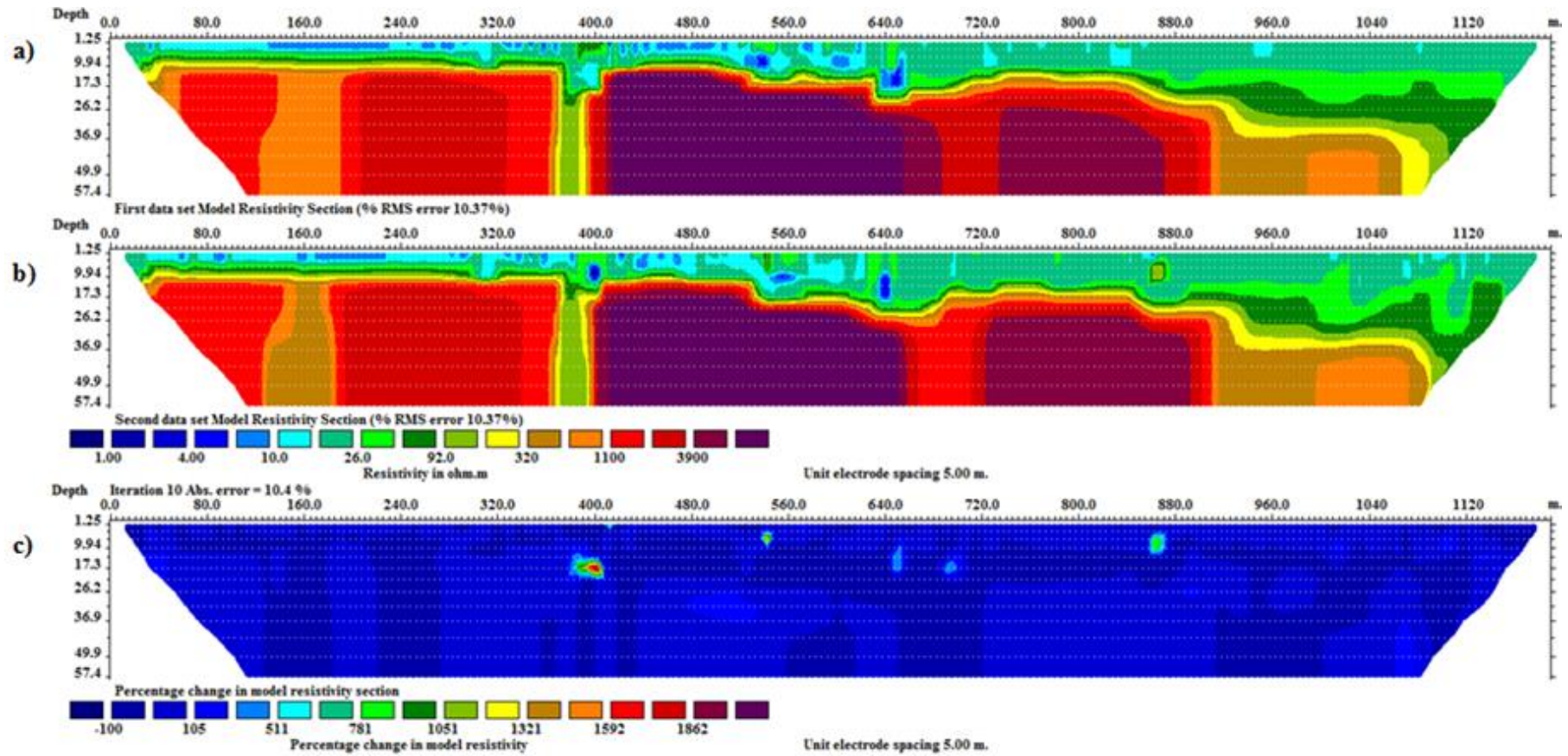


Fig. 6.9: (a) Inverse resistivity model of the fourth dataset, acquired on the 25th May 2016, (b) the inverse resistivity model of the fifth dataset, acquired on the 19th August 2016, (c) the percentage change in model resistivity sections with an absolute error of 10.4 %. The resistivity models shown are based on a dipole-dipole array.

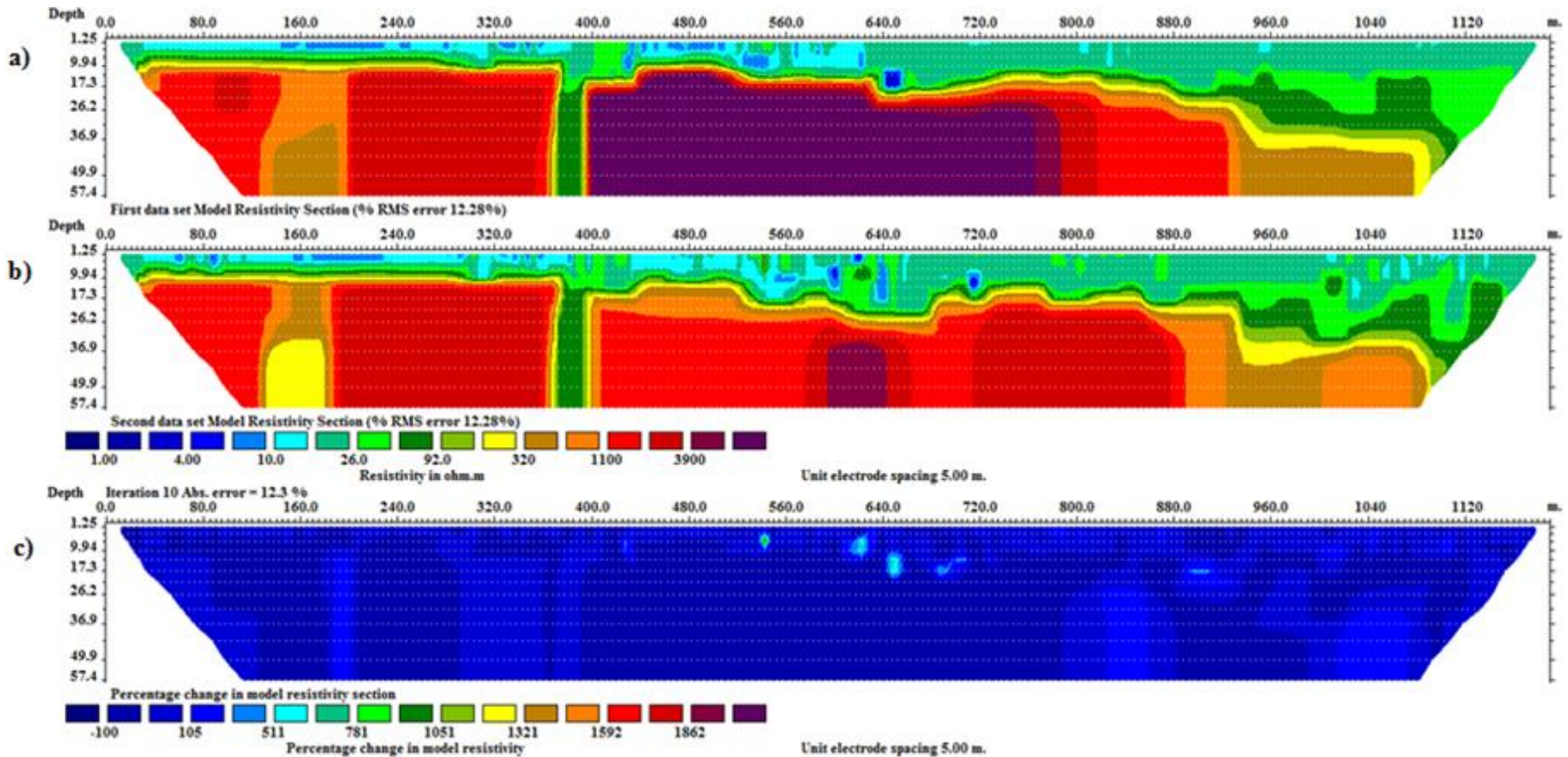


Fig. 6.10: (a) Inverse resistivity model of the fourth dataset, acquired on the 25th May 2016, (b) the inverse resistivity model of the fifth dataset, acquired on the 19th August 2016, (c) the percentage change in model resistivity sections with an absolute error of 12.3 %. The resistivity models shown are based on a dipole-dipole array. The fifth dataset appears to be more contaminated with noise compared to the rest of the datasets, hence the observed more rugged conductive (low resistivity zone)-resistive layer interface. However, there was no significant percentage change in model resistivity values between the initial (dataset 1) and last dataset (dataset 5), except in anomalous zones of about 500 ohm.m located between 500 m and 720 m between 9 m and 20 m depth.

6.2.1.3 Resistivity data analysis

6.2.1.3.1 Forward modeling

A layout of 48 electrodes is modeled using a dipole-dipole array and an electrode spacing of 10 m to simulate the actual survey. The Res2Dmod forward modeling program was used to compute synthetic data. The subsurface model was created with three different layers (Fig. 6.11). The upper layer was assigned a resistivity value of about 50 Ωm , representing the riprap material that overlies the dam core, with a thickness of 3 m. The second layer was assigned even lower resistivity values, about 8 Ωm . This second layer represents a conductive clay core, and was designed to have varying thicknesses ranging from 3 m to 30 m. Contrary to the low resistivity values assigned to the top two layers, the bottom layer was assigned very high resistivity values of about 10 000 Ωm representing the foundation made up of fresh metamorphic basement rocks. From the forward model, synthetic apparent resistivities were calculated and their inversions were done using Res2dinv software then compared with the measured data set model for equivalency.

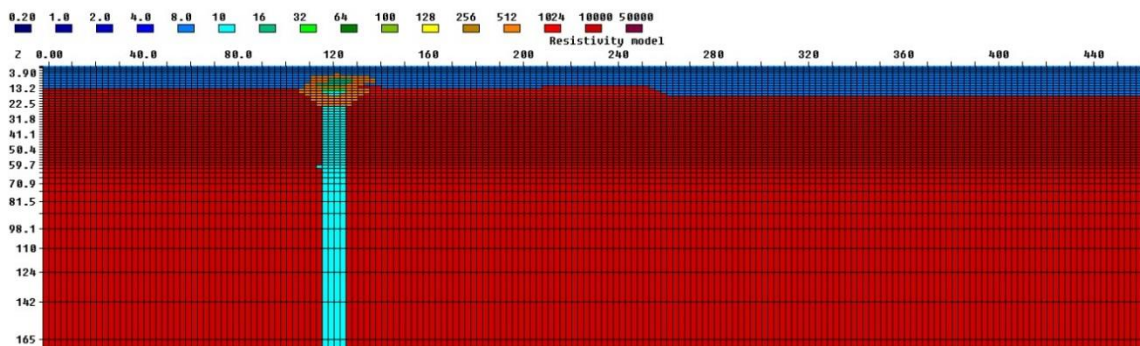


Fig. 6.11: Forward model of the dam embankment. This model is made up of three layers of varying thicknesses and resistivity. The top layer represents riprap material, the middle layer represents the dam core and the bottom and thickest layer represents the basement rock (the dam foundation).

In the forward model (Fig. 6.11), a conductive vertical structure was inserted to simulate a fracture that originates from the embankment-foundation interface with a sharp contrast in electrical resistivity with the material flanking it (basement rock). This is based on the assumption that the fracture is wide enough to be resolved by the ERI method (~20 m). In such cases, the air-filled fracture would be more resistive. However, the

embankment material that lies directly above the fracture was simulated to have lost its stability and falling into the fracture and in the process lowered the resistivity of the fracture. The loss of stability in the embankment material increases the air pockets in it and leads to resistivity increase in the embankment material affected if not water saturated.

In constructing the model (Fig. 6.12a), finite-element computational method was used to calculate the apparent resistivity values. The model has 52 grid rows/layers, corresponding to a total depth of 165 m. An acquisition sequence based on a dipole-dipole array with 48 electrodes spaced by 10 m was simulated. This resulted in a data set of 2160 apparent resistivity measurements. Before the inversion, 5 % of Gaussian noise was added to the data set because field data are never noise-free (Robert, 2012). The synthetic data set was then inverted to give the measured apparent resistivity pseudosection (Fig. 6.12b), the calculated apparent resistivity pseudosection (Fig. 6.12c) and the inverse model resistivity section (Fig. 6.12d).

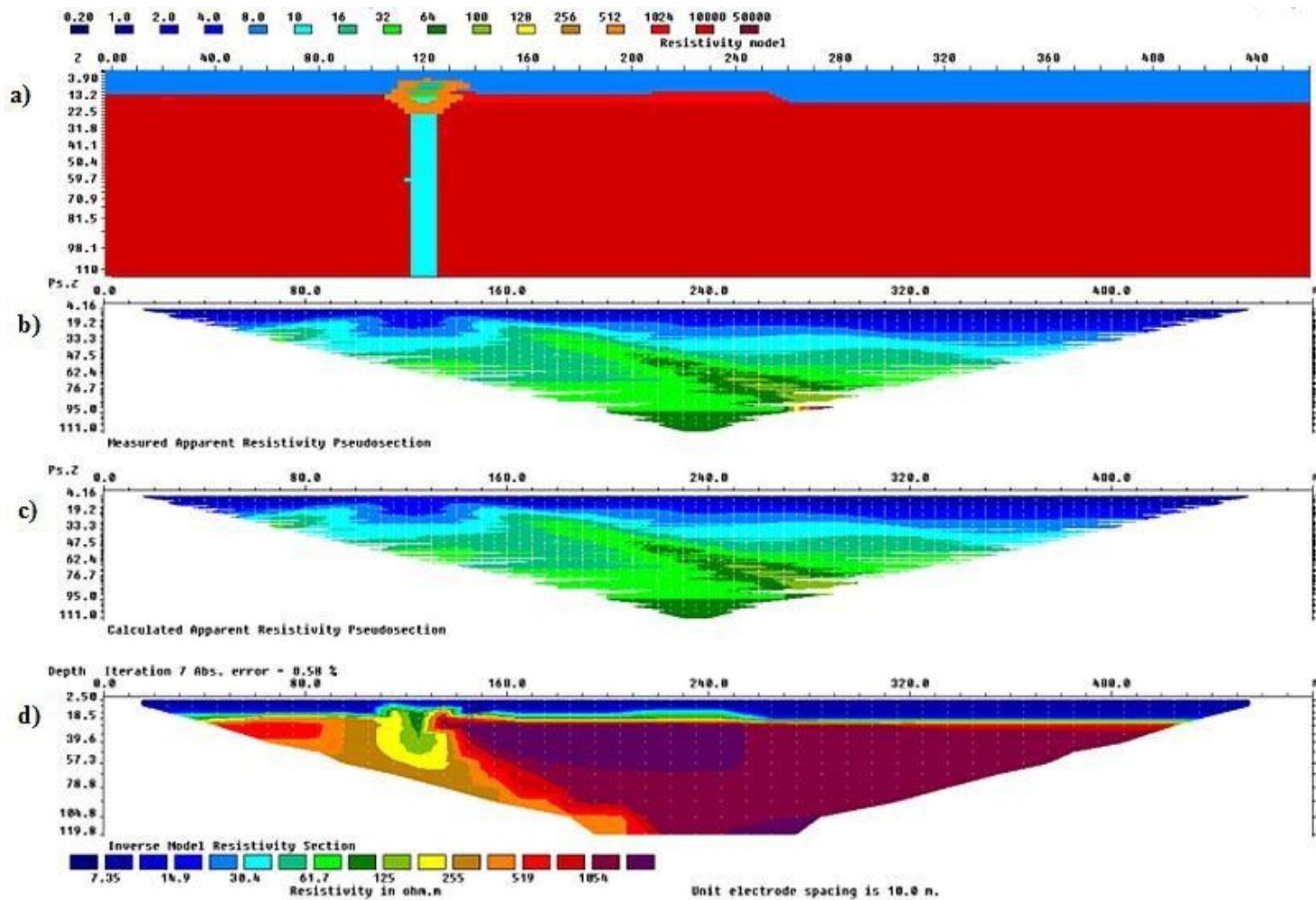


Fig. 6.12: Image of (a) the forward model of the idealized subsurface condition, (b) the measured apparent resistivity pseudosection, (c) the calculated apparent resistivity pseudosection, and (d) the inverse model resistivity section. The vertical structure inserted in the forward model simulates a fracture cutting across the basement rock, and responds well with the dipole-dipole array as observed in the final inverse model cutting across the basement rock.

6.2.2 Frequency domain EM data processing

Multi-frequency domain EM data are usually interpreted qualitatively by plotting profiles of the quadrature and the in-phase components of the secondary field against profile distance. In such cases, interpretations are based on the presence of peaks and troughs along profiles, with their sizes and orientation having direct implication on the nature of anomaly sources in the subsurface. However, vast progress has been made in qualitative and quantitative interpretation of EM induction surveys in the last two decades (Oskooi, 2004). The improvements include the new instrumentation coupled with new forward modeling and inversion approaches. In this study, an AEMINV (Pirttijärvi, 2011) program was used for the FDEM data inversion. AEMINV is a computer program for geophysical interpretation of frequency-domain airborne electromagnetic data using a one dimensional (1D) layered model. The model parameters in the inversion program include the electrical resistivity and thickness of the layers and the resistivity and magnetic susceptibility of the basement layer.

The inversions were done independently for each frequency using a 1D layered earth model. The starting initial model was optimized (an iterative linearized inversion) to update model parameters such that the data error (the difference between the measured and computed data) is minimized. Laterally constrained inversion of the data was achieved by minimizing the roughness of the model and smoothly varying resistivity thickness models were obtained (Fig. 6.13 to Fig. 6.22).

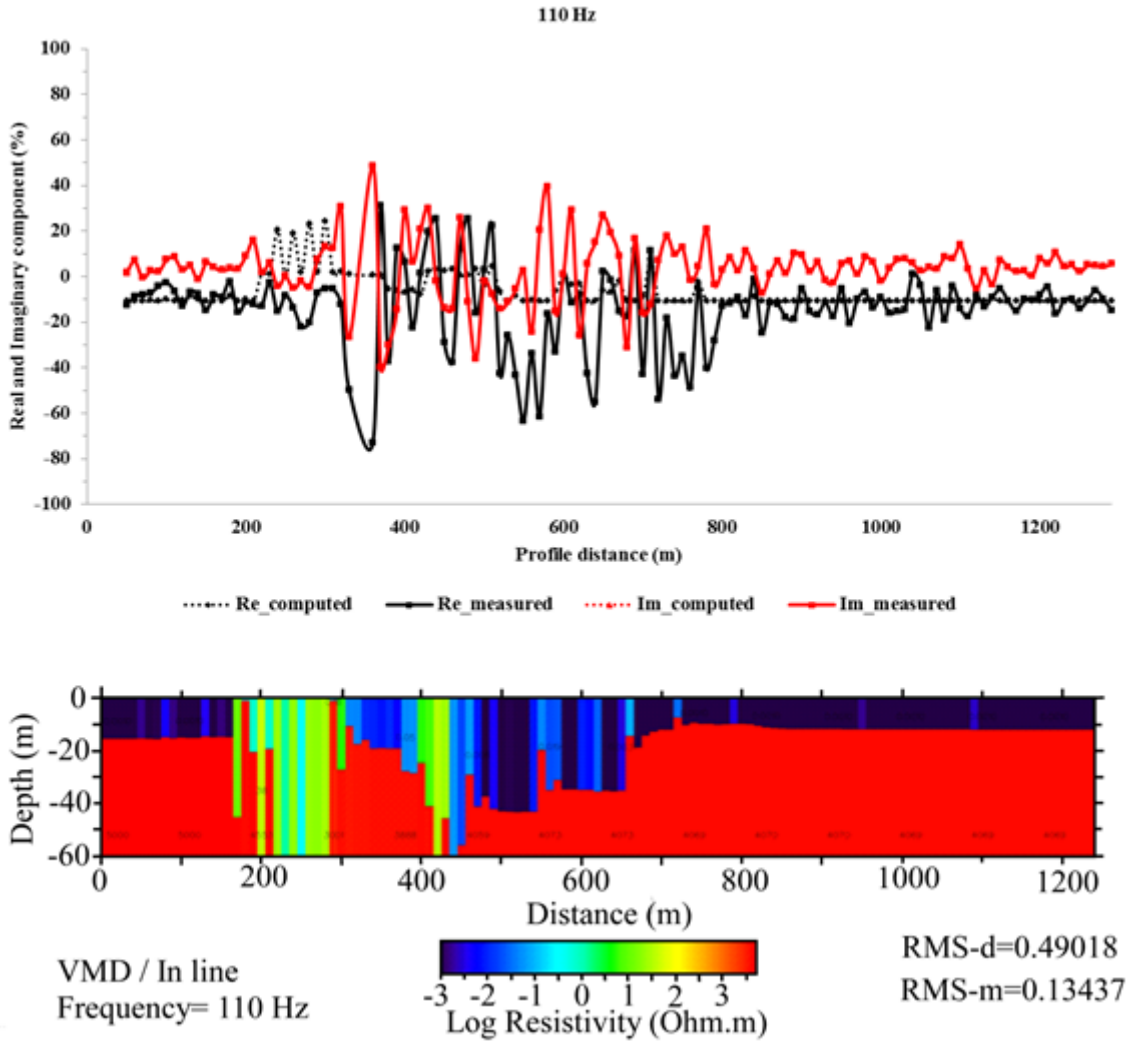


Fig. 6.13: (a) Profiles of the measured in-phase/real (solid black), computed in-phase (dotted black), measured quadrature/ imaginary (solid red) and the computed quadrature (dotted red) components of the secondary electromagnetic field expressed as percentage of the primary electromagnetic field (b) a two layered model showing resistivity distribution to a depth 60 m. A large negative anomaly is evident at approximately 370 m, followed by large amplitude responses between 450 m and 800 m, on the measured real and quadrature component. Unlike the measured data, the computed real and quadrature profiles show minimal variation on the amplitudes except at 200 m to 250 m, where positive peaks are observed. The resistivity model shows two, a conductive layer of varying thickness from 10 m to approximately 38 m overlying a more resistive layer which extends to a depth of 60 m. The two model layers are cut vertically by two zones of moderate resistivities, the first between 200 m and 300 m with an average thickness approximately 60 m, and the second zone at the 400 m mark, with an average thickness of 30 m.

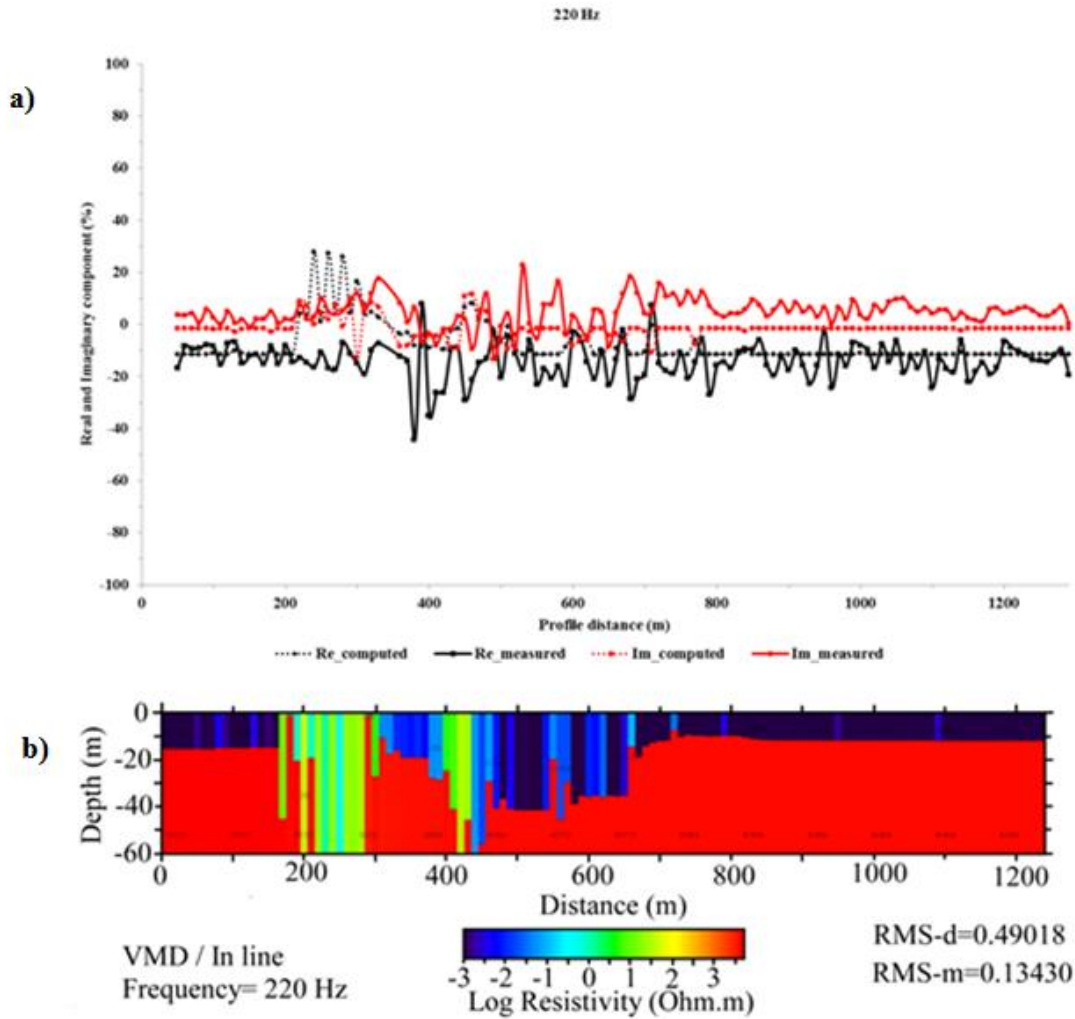


Fig. 6.14: (a) Profiles of the measured in-phase/real (solid black), computed in-phase (dotted black), measured quadrature/ imaginary (solid red) and the computed quadrature (dotted red) components of the secondary electromagnetic field expressed as percentage of the primary electromagnetic field (b) a two layered model showing resistivity distribution to a depth 60 m. A generally negative anomaly is observed on the measured data profiles between 400 m and roughly 500 m, and very minimal variation from 50 m towards 400 m, then 700 m to 1290 m. Positive peaks are observed between 200 m and 280 m on the computed real and quadrature components of the electromagnetic field. On the model, two layers are observed, a conductive layer of varying thickness from 10 m to approximately 38 m overlying a more resistive layer which extends to a depth of 60 m. The two model layers are cut vertically by two zones of moderate resistivities, the first between 200 m and 300 m with an average thickness approximately 60 m, and the second zone at the 400 m mark, with an average thickness of 30 m.

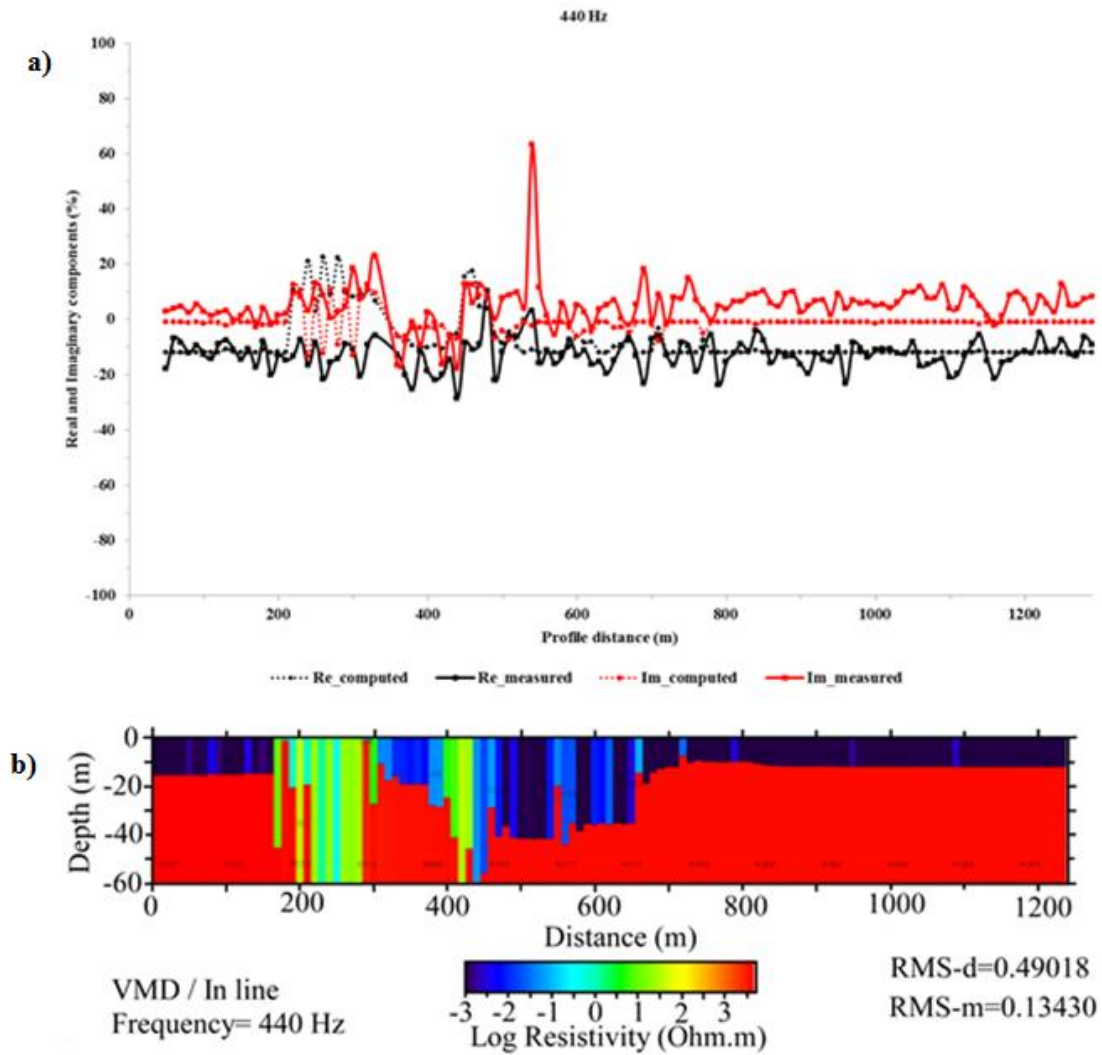


Fig. 6.15: (a) Profiles of the measured in-phase/real (solid black), computed in-phase (dotted black), measured quadrature/ imaginary (solid red) and the computed quadrature (dotted red) components of the secondary electromagnetic field expressed as percentage of the primary electromagnetic field (b) a two layered model showing resistivity distribution to a depth 60 m. A large negative anomaly is evident above 400 m for both real and quadrature components of the field and also an additional positive spike on the measured quadrature component profile at approximately 550 m. The computed real component of the field show positive peaks, while the computed quadrature component of the field at 200 m. The resistivity model shows two, a conductive layer of varying thickness from 10 m to approximately 38 m overlying a more resistive layer which extends to a depth of 60 m. The two model layers are cut vertically by two zones of moderate resistivities, the first between 200 m and 300 m with an average thickness approximately 60 m, and the second zone at the 400 m mark, with an average thickness of 30 m. The negative anomaly at 400 m on the measured real and quadrature components of the field coincide well with the anomalous zone at 400 m in the model, and only the computed real and quadrature components of the field show the responses coinciding to the anomaly at 200 m on the model.

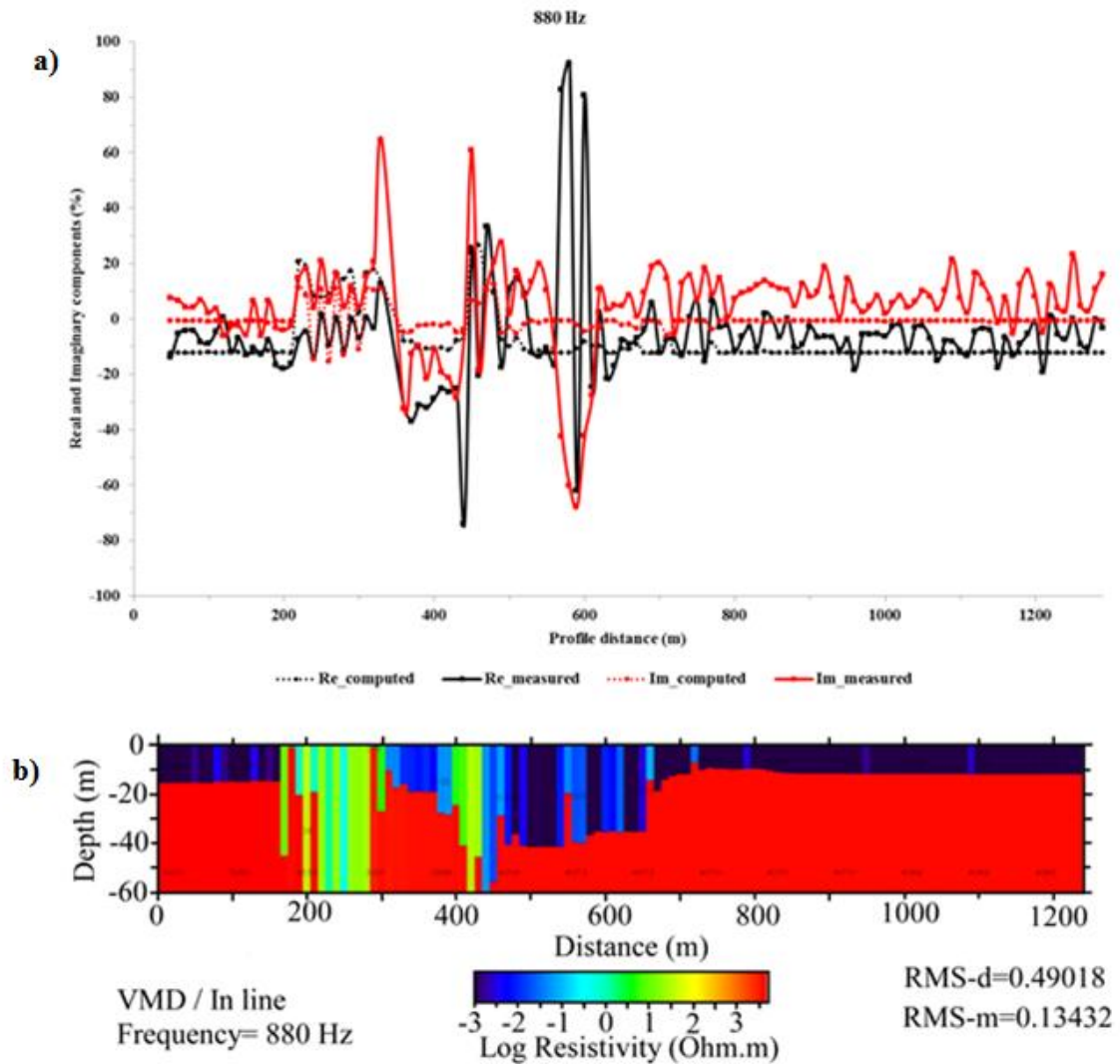


Fig. 6.16: (a) Profiles of the measured in-phase/real (solid black), computed in-phase (dotted black), measured quadrature/ imaginary (solid red) and the computed quadrature (dotted red) components of the secondary electromagnetic field expressed as percentage of the primary electromagnetic field (b) a two layered model showing resistivity distribution to a depth 60 m. A large negative anomaly is observed above 400 m for both measured and computed real and quadrature components of the field. An additional positive spike on the measured real component profile and negative spike on the measured quadrature is observed at 600 m. However, there is no indication of an anomalous zone at 600 m on the model that relates to the enlarged amplitudes on the profiles at 600 m. The negative anomaly observed on both computed and measured components coincide well with a moderately conductive zone on the model at 400 m. Computed real component of the field show positive peaks while the computed quadrature component of the field at 200 m. The resistivity model shows two, a conductive layer of varying thickness from 10 m to approximately 38 m overlying a more resistive layer which extends to a depth of 60 m.

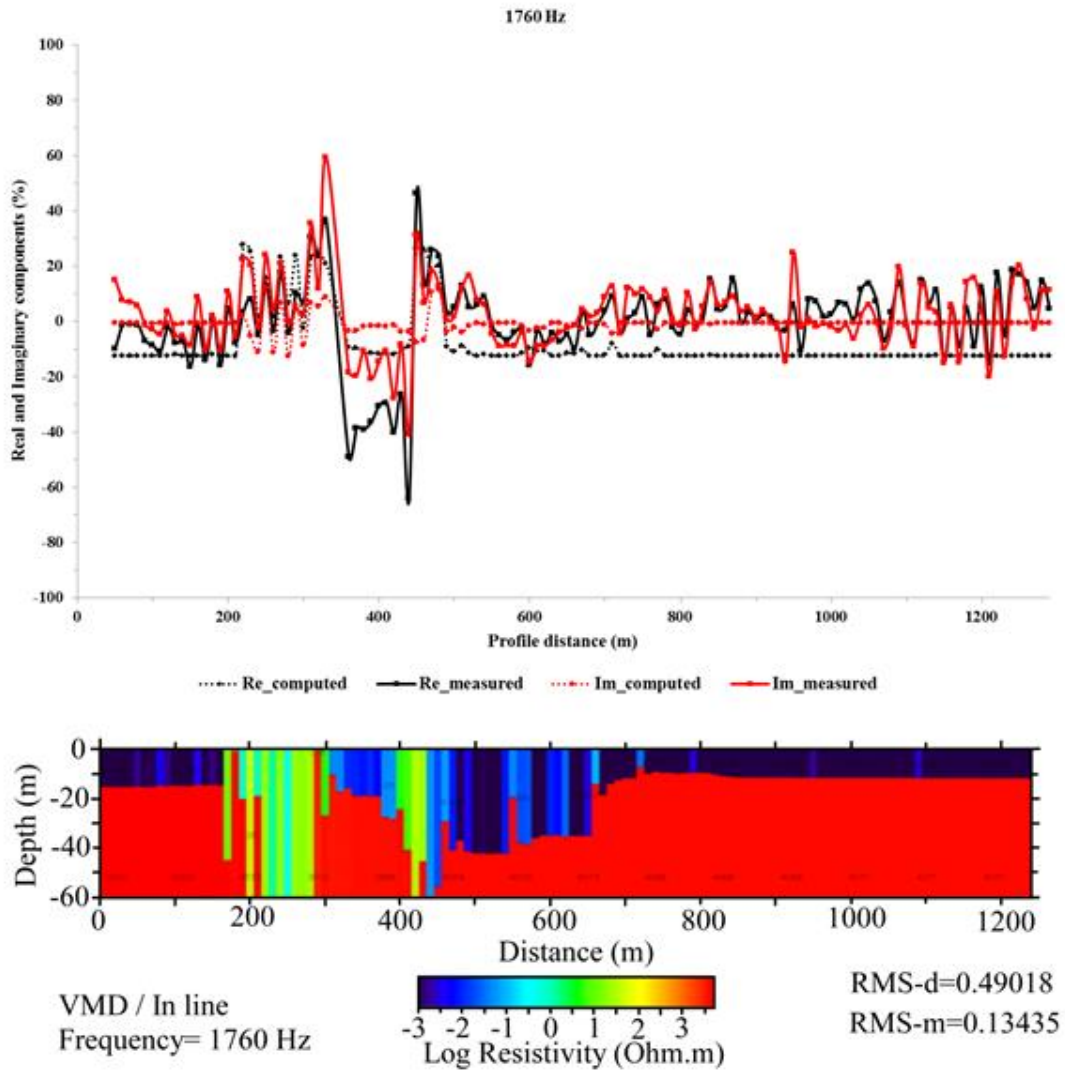


Fig. 6.17: (a) Profiles of the measured in-phase/real (solid black), computed in-phase (dotted black), measured quadrature/ imaginary (solid red) and the computed quadrature (dotted red) components of the secondary electromagnetic field expressed as percentage of the primary electromagnetic field (b) a two layered model showing resistivity distribution to a depth 60 m. A large negative anomaly is observed above 400 m for both measured and computed real and quadrature components of the field. It is evident from the profiles that the real components have larger amplitudes than quadrature components of the field. The negative anomaly observed on both computed and measured components coincide well with a moderately conductive zone on the model at 400 m. Also, there is a wide negative anomaly ranging from 500 m to 700 m, coinciding well with a thickened conductive layer between 450 m and 700 m on the layered model. Additionally, there are dominant spikes between 900 m and 1000 m on the measured components of the field.

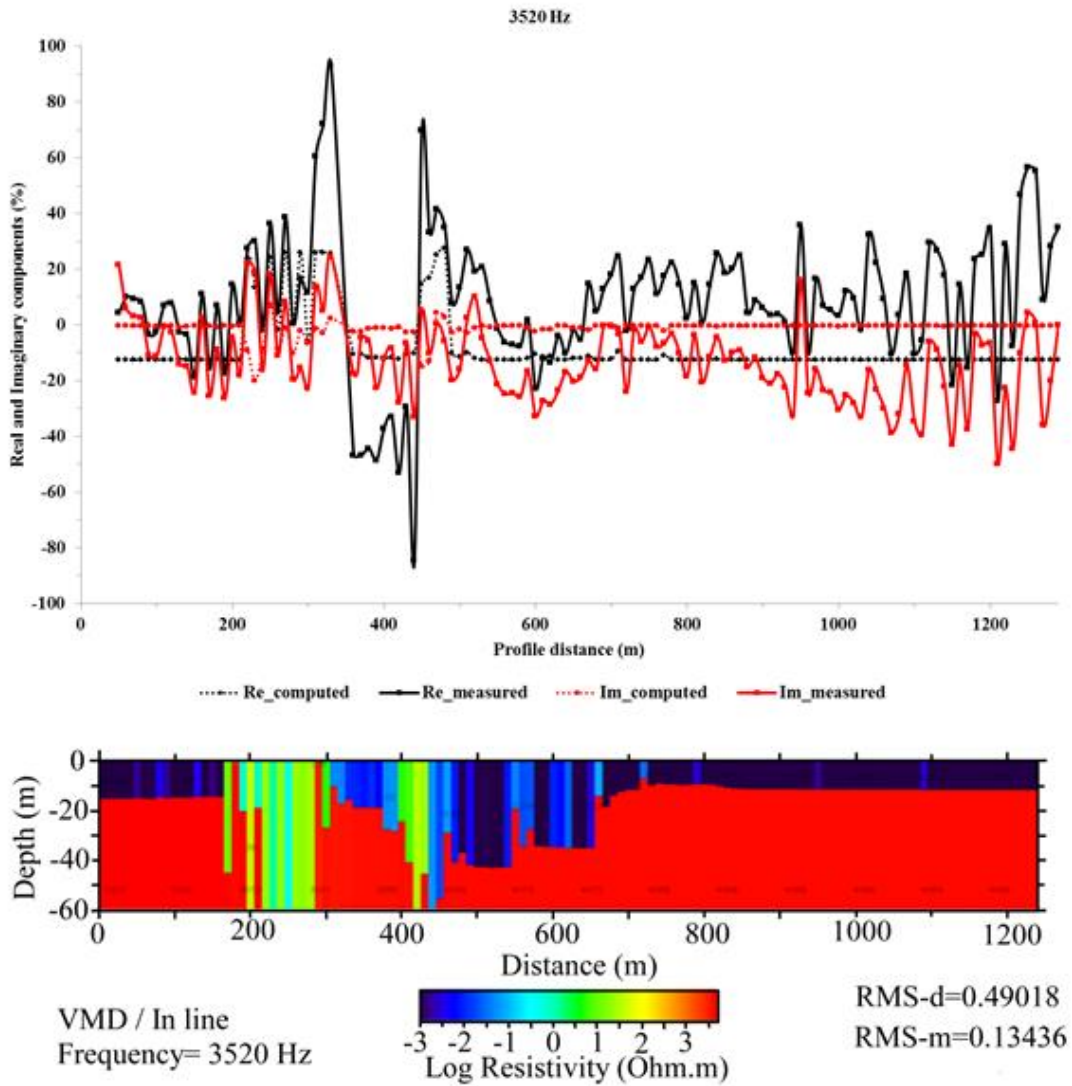


Fig. 6.18: (a) Profiles of the measured in-phase/real (solid black), computed in-phase (dotted black), measured quadrature/ imaginary (solid red) and the computed quadrature (dotted red) components of the secondary electromagnetic field expressed as percentage of the primary electromagnetic field (b) a two layered model showing resistivity distribution to a depth 60 m. A large negative anomaly is observed above 400 m for both measured and computed real and quadrature components of the field. It is evident from the profiles that the real components have larger amplitudes than quadrature components of the field. The negative anomaly observed on both computed and measured components coincide well with a moderately conductive zone on the model at 400 m. Also, there is a wide negative anomaly ranging from 500 m to 700 m, coinciding well with a thickened conductive layer between 450 m and 700 m on the layered model. Between 900 m and 1000 m, there is a positive spike on the measured real and quadrature profiles.

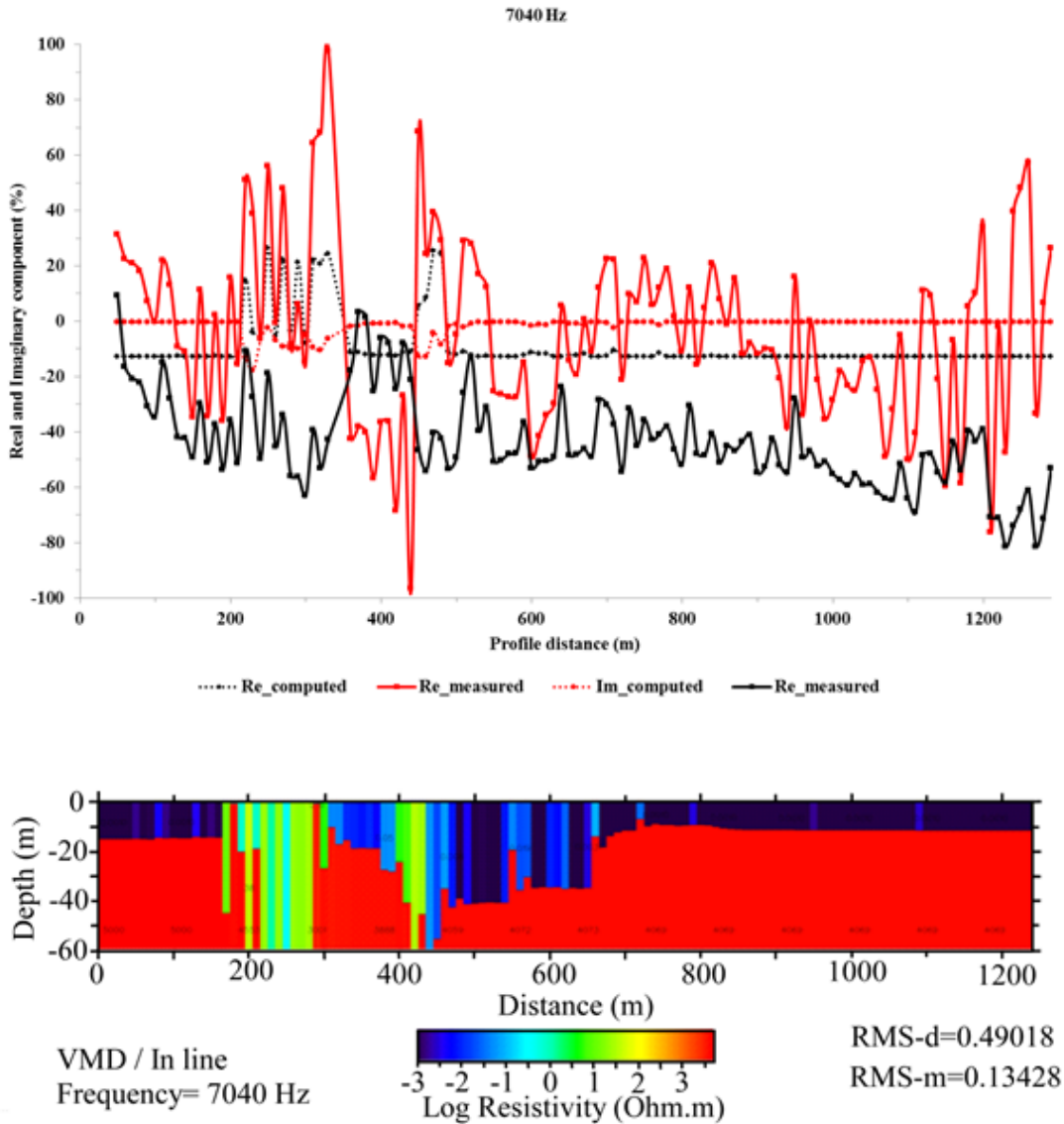


Fig. 6.19: (a) Profiles of the measured in-phase/real (solid black), computed in-phase (dotted black), measured quadrature/ imaginary (solid red) and the computed quadrature (dotted red) components of the secondary electromagnetic field expressed as percentage of the primary electromagnetic field (b) a two layered model showing resistivity distribution to a depth 60 m. A prominent negative anomaly is observed above 400 m on measured quadrature component of the field. On the measured real component, the anomaly at 400 m appears to be positive. The anomalies observed on both computed and measured components at 400 m coincide well with a moderately conductive zone on the model. Also, there is a wide negative anomaly with frequent variations in amplitude between 100 m and 250 m. At 600 m, only the measured quadrature shows a significant negative anomaly whereas the response is not conclusive with the real component of the field at the same location. Despite the large amplitude variations observed in the measured components of the field, a positive dominant spike is still evident between 900 m and 1000 m.

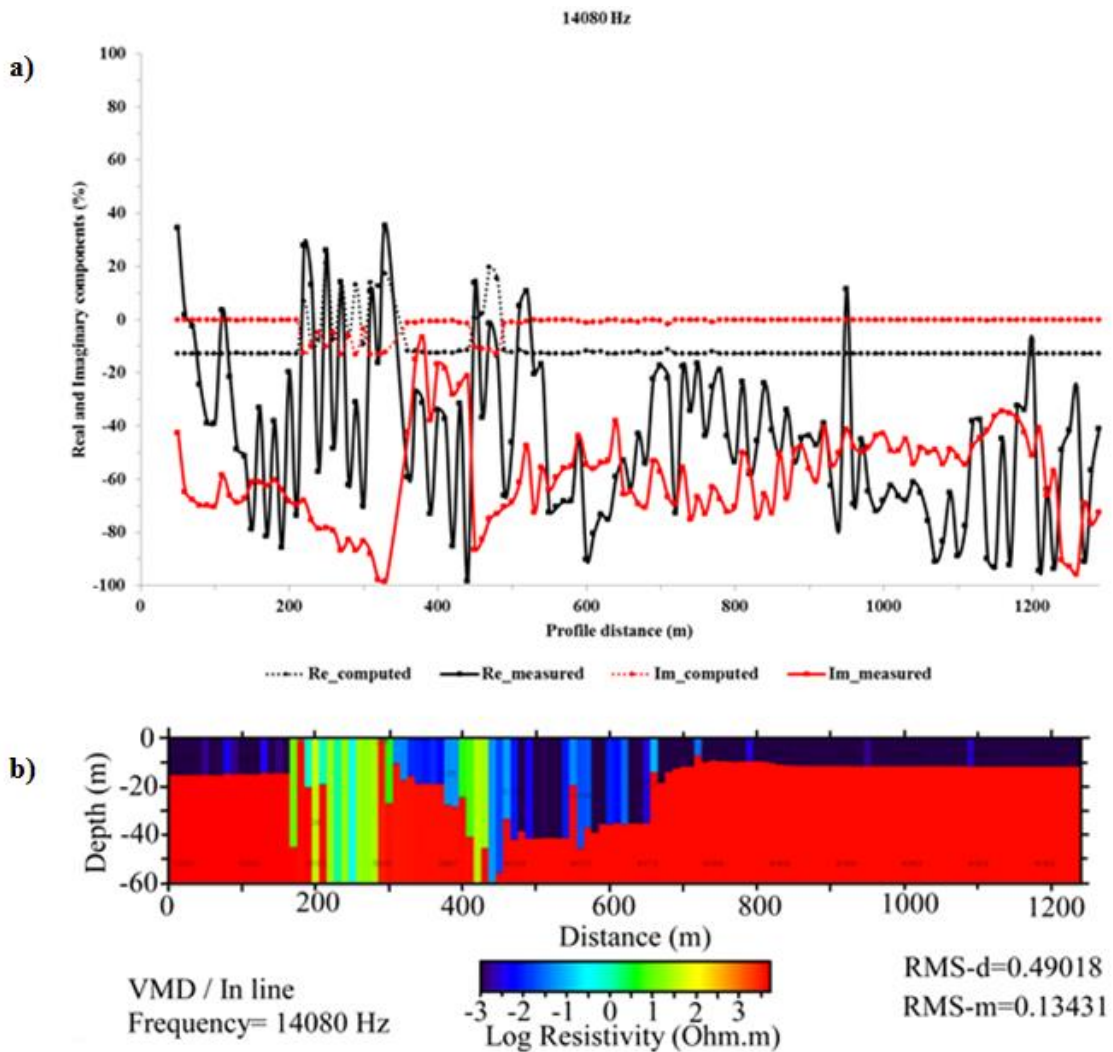


Fig. 6.20: (a) Profiles of the measured in-phase/real (solid black), computed in-phase (dotted black), measured quadrature/ imaginary (solid red) and the computed quadrature (dotted red) components of the secondary electromagnetic field expressed as percentage of the primary electromagnetic field (b) a two layered model showing resistivity distribution to a depth 60 m. A prominent positive anomaly is observed above 400 m on measured quadrature component of the field. On the measured real component, the anomaly at 400 m appears to be positive. The measured real component shows two distinctive negative anomalies at 200 m and 400 m coinciding well with the two anomalous zones at the same locations, and a positive anomaly at approximately 950 m. on the measured real component of the field, there is also a wide negative anomaly corresponding well with the thickened conductive layer on the model from 500 m to 700 m.

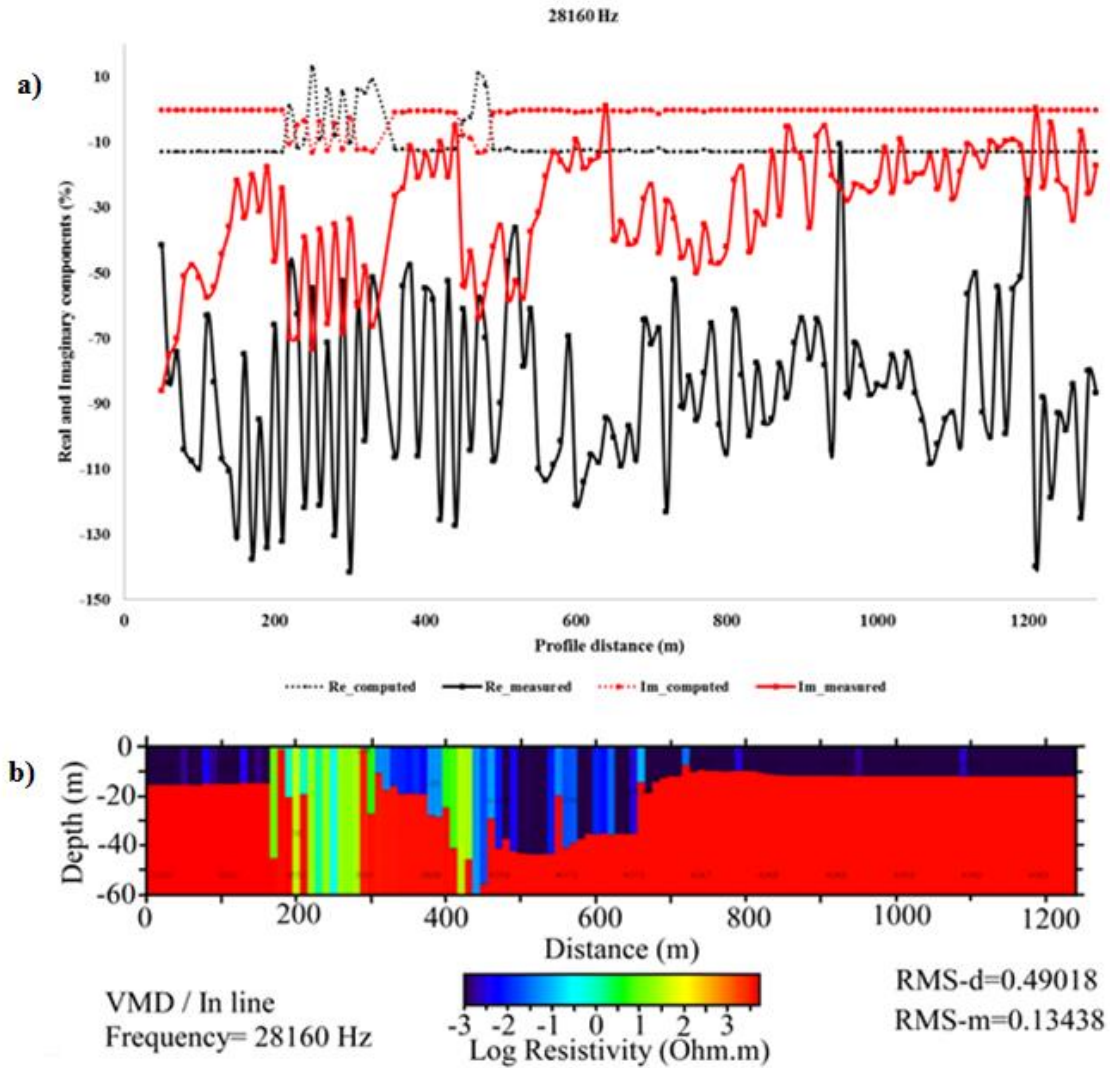


Fig. 6.21: (a) Profiles of the measured in-phase/real (solid black), computed in-phase (dotted black), measured quadrature/ imaginary (solid red) and the computed quadrature (dotted red) components of the secondary electromagnetic field expressed as percentage of the primary electromagnetic field (b) a two layered model showing resistivity distribution to a depth 60 m. There are no distinctive anomalies on the measured quadrature component of the field, but the single point negative spikes can be observed between 100 m and 200 m, at 300 m and at 420 m. Positive single point spikes are also observed at 940 m and at 1200 m. The computed real and quadrature components show opposite anomalies between 200 m and 300 m, and 400 m and 450 m.

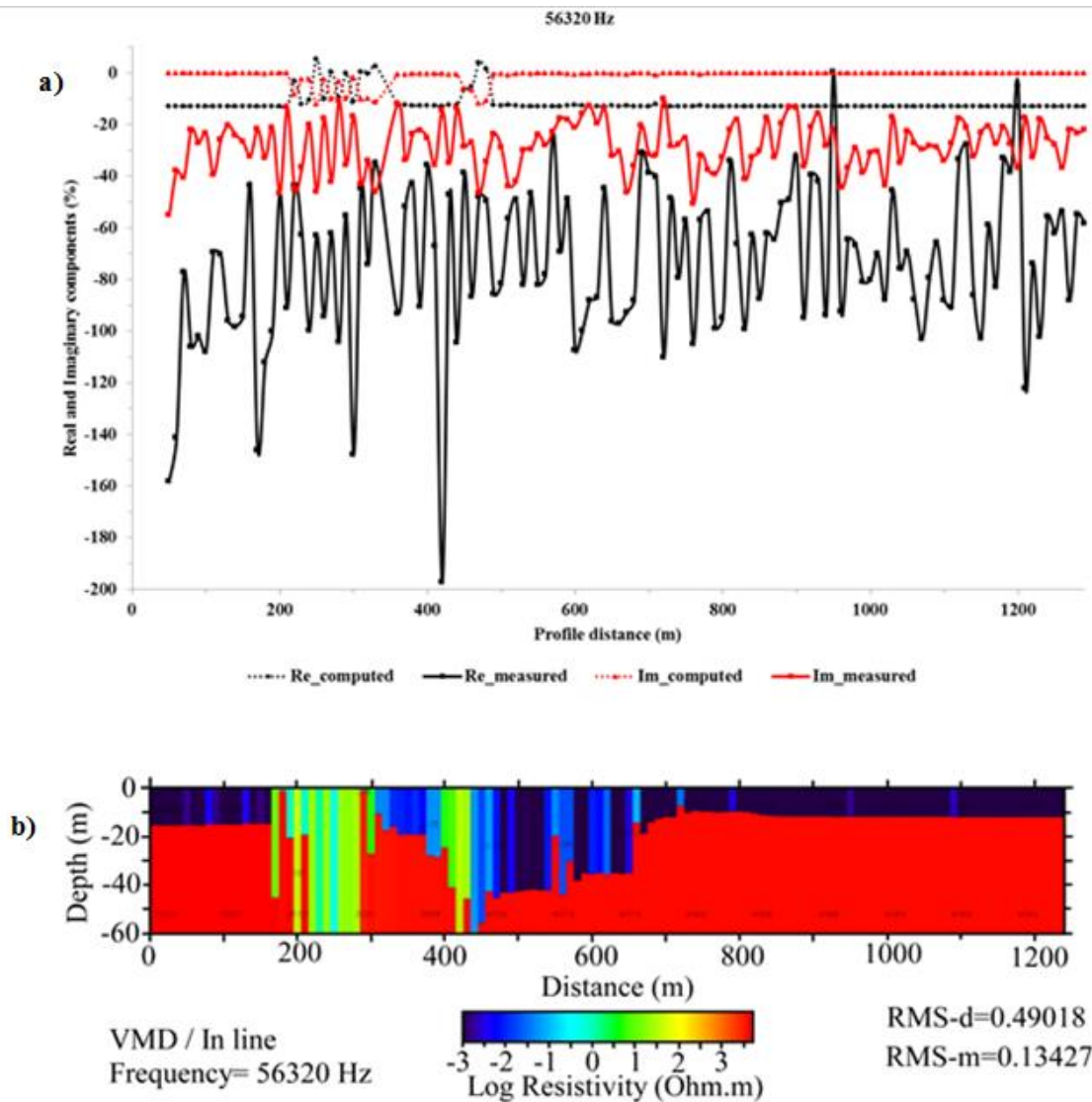


Fig. 6.22: (a) Profiles of the measured in-phase/real (solid black), computed in-phase component (dotted black), measured quadrature/ imaginary (solid red) and the computed quadrature (dotted red) components of the secondary electromagnetic field expressed as percentage of the primary electromagnetic field (b) a two layered model showing resistivity distribution to a depth 60 m. A large negative anomaly is evident at approximately 370 m, followed by large amplitude responses between 450 m and 800 m, on the measured real and quadrature component. Unlike the measured data, the computed real and quadrature profiles show minimal variation on the amplitudes except at 200 m to 250 m, where positive peaks are observed.

6.2.3 High resolution aeromagnetic data processing

Second vertical derivative filters were applied to the residual total magnetic field data in order to enhance anomalies of shallow seated features in the study area (Fig. 6.23), whereas, analytic signal map (Fig. 6.24) was useful in locating edges of the sources of magnetic bodies (Montaj, 2013). The analytic signal is the square of the square root of the sum of squares of derivatives in three orthogonal directions as shown in equation 6.1:

$$\text{Analytical Signal (AS)} = \sqrt{\left(\frac{d^2T}{dx^2} + \frac{d^2T}{dy^2} + \frac{d^2T}{dz^2}\right)} \dots\dots\dots (6.1)$$

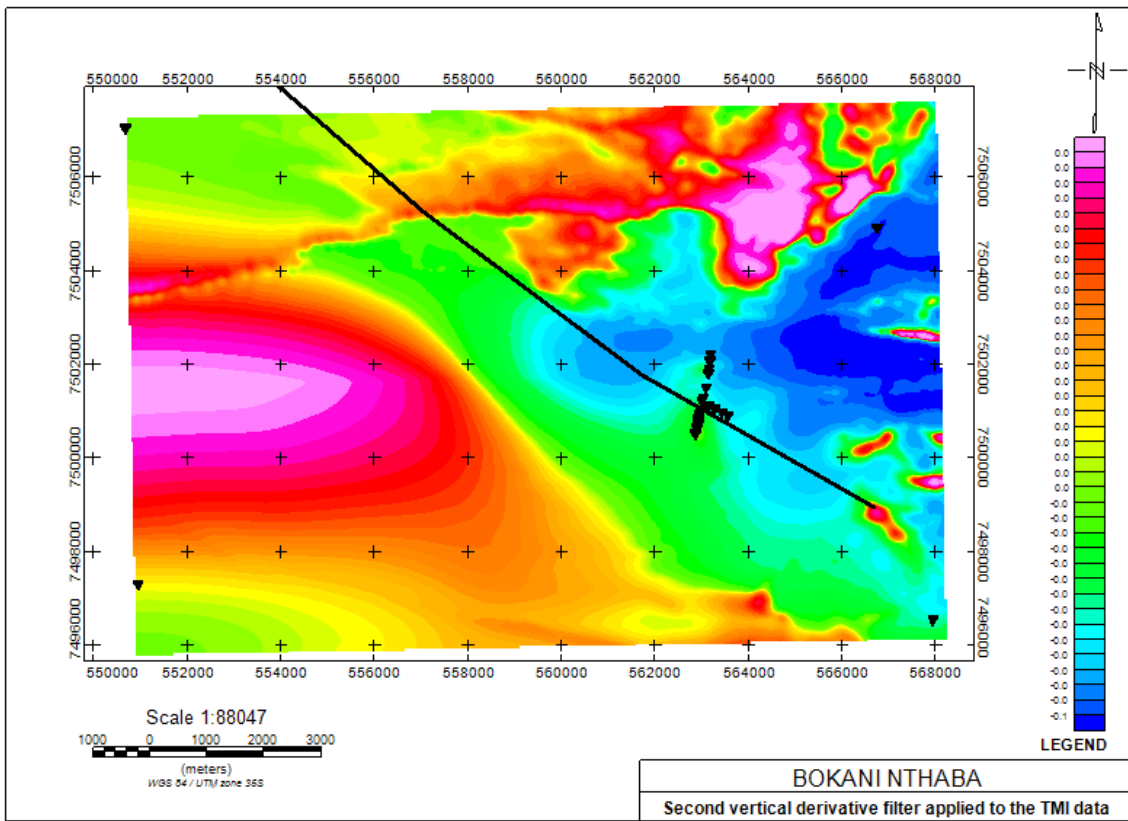


Fig. 6.23: A map showing the second vertical derivative filter applied to the residual aeromagnetic data (nT). An inserted line (solid black) represents a NW-SE trending Lechana Fault location cutting across the dam wall.

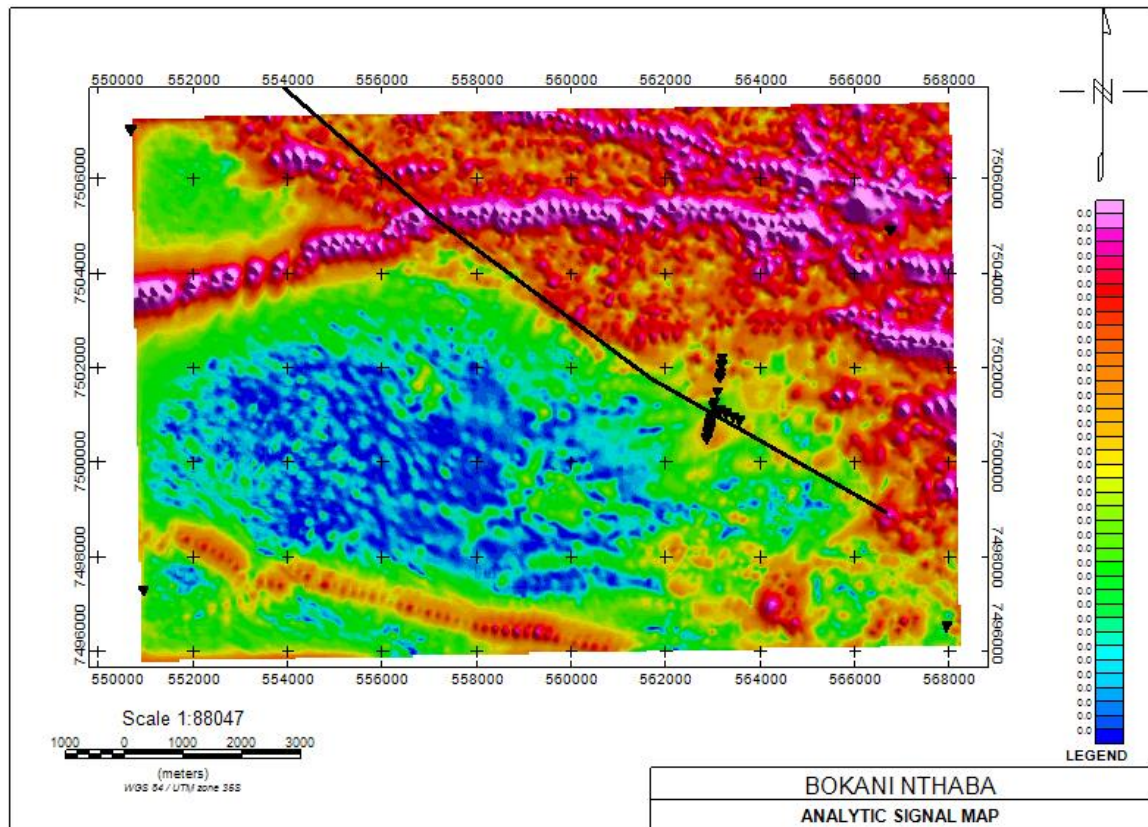


Fig. 6.24: A map showing an analytic signal map (nT). Also shown in this map is the NW-SE trending Lechana fault which cuts across the dam embankment section and indicated by a change from low AS to high AS values towards the north east direction on the map.

Ternary maps were prepared in order to enhance basement structural features such as dykes and faults. A ternary diagram is a map made by combining color attributes of three separate data sets and structural interpretation maps were made from these ternary maps by tracing lineaments and defining boundaries between domains of distinctly magnetic character; in this study, optimum enhancement of basement structures was obtained by plotting the total magnetic field intensity (TMI), vertical derivatives and the analytic signal data into one color map (Fig. 6.25).

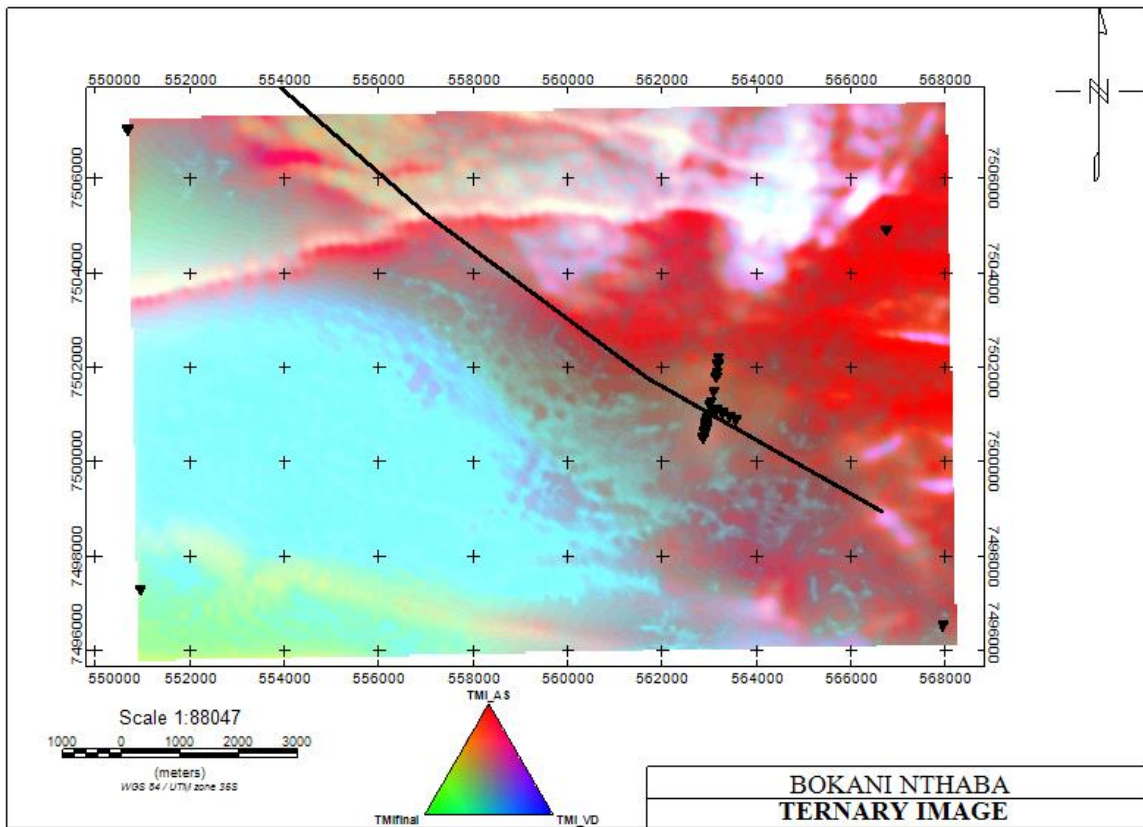


Fig. 6.25: A ternary image of the total magnetic intensity map, the second vertical derivative map and the analytic signal filtered map.

7 Data interpretation and discussion

To aid interpretation of the measured data, the inverted synthetic model section was compared with the field data resistivity inverse section (Fig. 7.1). There is minimal discrepancy observed between the resistivity model of the measured and the resistivity model of the synthetic data, with much emphasis on the conductive fracture in both models at 400 m on the measured data model and 120 m on the synthetic data model. In both datasets, the sharp electrical resistivity contrast between the layers is observed and the simulated fracture that cuts across the construction materials into the basement rock gives a close, if not similar response in the pseudosections and the inverse models. The similarity between the synthetic and measured data models gives confidence in interpreting the field data models.

In addition to the forward models, a vertical resistivity cross section model (Fig. 7.2) of the subsurface was generated and positioned in Google Earth. The logic behind generating the cross sectional model was to connect surface features with the underlying subsurface features and geology of the Lotsane dam embankment and also use it as an aid in interpretation. Figure 7.3 represents an interpretation of the inverse resistivity model.

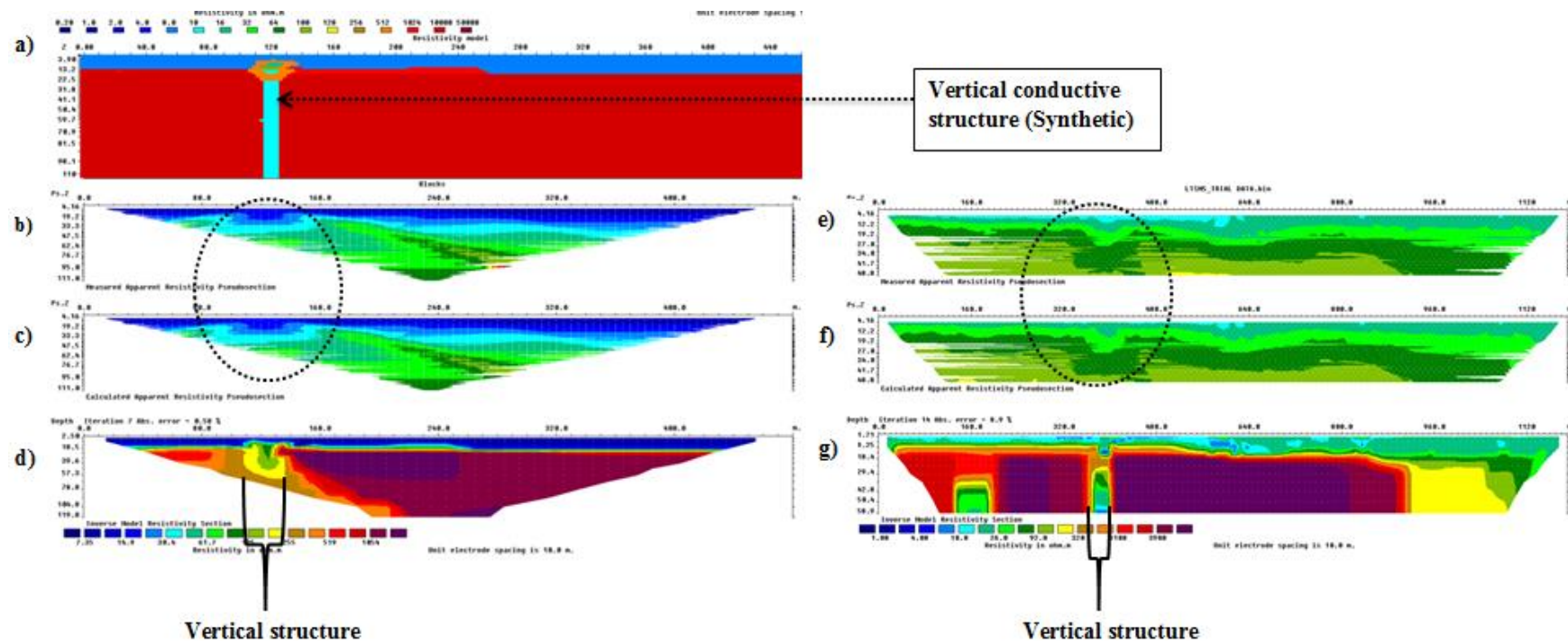


Fig. 7.1: Images comprising the synthetic and measured data set results: (a) the forward model depicting two major layers with a vertical conductive structure embedded in a highly resistive medium; (b) the measured apparent resistivity pseudosection of the synthetic data set, (c) the calculated apparent resistivity pseudosection of the synthetic data set, (d) the inverse model resistivity section of the synthetic data, (e) the measured apparent pseudosection of the measured data, (f) the calculated apparent resistivity pseudosection of the measured data, and (g) the inverse model resistivity section of the measured data. The dotted ovals in pseudosections of the synthetic and measured data indicate a typical response of the dipole-dipole array to vertical structures in the subsurface. Also evident in both inverse models is the low resistivity vertical zone within the highly resistive zone interpreted to be a fracture.



Fig. 7.2: The vertical resistivity cross section model on a satellite image of the dam embankment. Anomalous zone 1 and zone 2 in the resistivity model are situated over a water pipe line and water level gauge pipes, respectively.

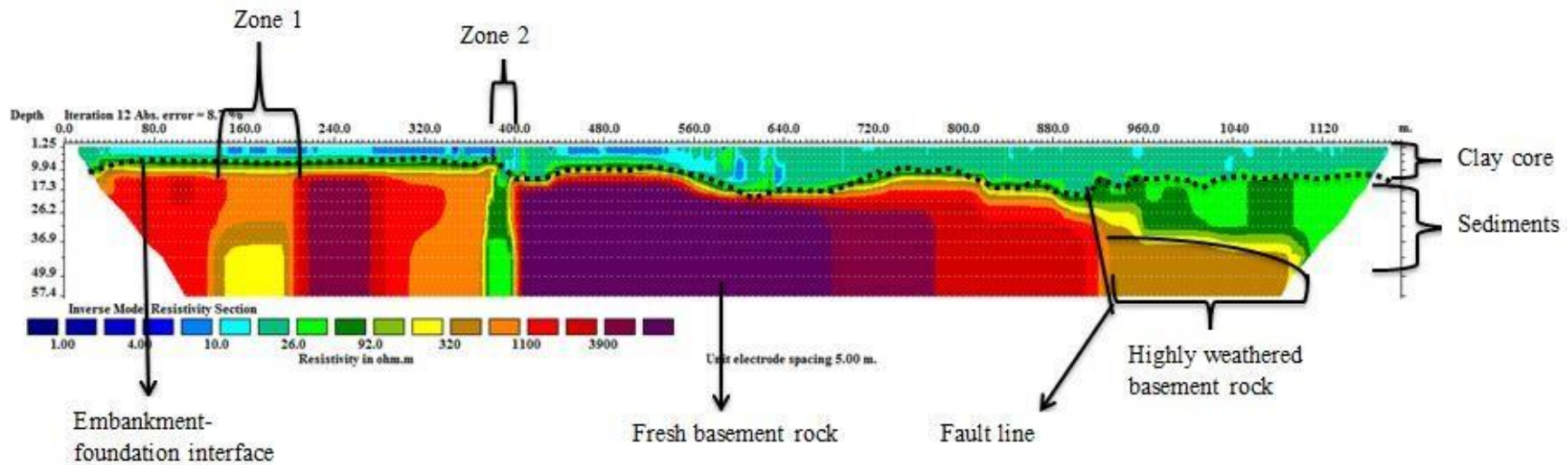


Fig. 7.3: Resistivity inverse model of the Lotsane Dam embankment. The upper most layer represents a conductive clay core of resistivity values < 26 ohm.m and layer thickness range of 10 m to about 25 m; the underlying layer represents a basement metamorphic rock of more than 1000 ohm.m resistivity values with a rugged surface. Zone 1 and zone 2 are fractures extending into the basement rock (dam foundation), which are about 60 m and 30 m wide, respectively. Material (sediments) of intermediate resistivity values (26-92 ohm.m) appears to have accumulated in zone 2, whereas zone 1 appears to be covered by the highly weathered basement rock fragments or concrete material of resistivity values ranging from (300-1000 ohm.m). This interpretation follows a report by SMEC et al. (2012), which suggested that the trenches were made before installing water pipes into the dam, and were subsequently sealed with concrete and loose fragments of moderately weathered basement rocks. Thin layers of varying resistivity values ranging from 92-320 ohm.m are also observed at the embankment-foundation interface. The variations/ undulations in resistivity at the interface are interpreted to be due to the highly weathered basement rock surface. At an embankment length of 900 m, the fresh basement rock appears to have been replaced by either the highly weathered basement rock or by accumulation of sediments (80-1000 ohm.m). The contact between the fresh basement rock and the sediments at the 900 m mark is interpreted to be a fault line, or an indication of the presence of a fault scarp. The sediments cover beyond the 900 m mark on the dam embankment sandwiched by the clay core and the highly weathered basement rock has a thickness range of about 20 m to about 33 m.

The purpose of time-lapse resistivity measurements is to track the changes in the subsurface that occur with time. Time-lapse analysis based on the differences between datasets acquired along the same profile, and interpretation was made using the difference models obtained. Changes in the lateral and depth extension were observed and quantified using the time-lapse inversion method. This data processing scheme revealed anomalous situations in the resistivity difference models. Time-lapse images enabled us to identify the increments ($> 0 \Omega\text{m}$) and reductions ($< 0 \Omega\text{m}$) that the calculated electrical resistivity values exhibit for temporal periods. Localized resistivity changes in dataset model shown in Figure 7.4(a) were observed below the 400 m mark along the profile mainly ranging from 10 m to 20 m, situated between 17.3 m and 26.2 m depths. This anomalous zone shows an increment in resistivity of more than 700 Ωm . These increments are interpreted to be caused by increase in pore spaces that are lacking in water, or whose water is clean (free from salinity) or due to loss of fine material that lies above the fracture by a process of suffusion, or a combination of these factors. In a suffusion process, fine grained particles migrate leaving behind coarser particles (e.g., sand). Aaltogen (2001), as cited in Samouëlian et al. (2006) reported that coarse-grained materials present a wider range in seasonal resistivity variation than clayey soil. It is also well understood that materials whose pore spaces lack water, or whose connate water is clean (free from salinity, even if water saturated) will show high resistivity values.

Figure 7.4(b) does not indicate increment or reduction in resistivity values below the 400 m mark along the profile, giving implications that dataset two and dataset three had almost similar resistivity values, except at a zone marked by the dotted red oval below the 720 m mark along the profile within a depth range of 9.94 m to 17.3 m, an increment of less than 700 Ωm in resistivity. Darker tone of blue color covers most parts of the difference model (generally $< 100 \Omega\text{m}$) and represents minimal reduction in electrical resistivity values. The minimal variation in resistivity and the observed small resistivity reductions in most parts of Figure 7.4(b) are interpreted to be due to the time period in which the two datasets were acquired (wet season), which was characterized by rain water infiltrations, which might have lowered the resistivity values of the two datasets compared to the initial dataset (Kaspar et al., 2016). A prominent anomaly is observed between 400 m and 440 m along the profile in Figure 7.4(c) between 9.94 m and 17.3 m in depth. The resistivity range of this anomaly is from 700 Ωm to 1000 Ωm .

In this model, it is observed that there is an extension of the anomaly with a 5 m width to the maximum investigated depth, with a resistivity increase of less than 500 Ωm . Compared to the Figures 7.4(a) and 7.4(b), the presence of the 5 m wide vertical extension was interpreted to represent a dried (or low moisture content) portion of the fracture, considering the period in which the fourth dataset was acquired in (dry season- in May). During this period the precipitation was very minimal (about 0 to 2.4 mm) and the temperature was low compared to the wet season (about 19°C). According to Samouëlian et al. (2006), the electrical resistivity increases when the temperature decreases, at any level of salinity. Samouëlian et al. (2006) also suggested that materials whose pore spaces lack water will show high resistivity.

Figure 7.4(d) also shows a prominent anomaly below the 400 m mark along the profile, but with smaller dimensions compared to the anomalous zone observed in Figure 7.4(c) at the same location. The resistivity increment observed in this zone is interpreted to be due to dry conditions of the subsurface and the increased pores (pores which lack water) due to suffusion. In all the difference models, anomalous zones other than the prominent one observed at the 400 m mark are interpreted to indicate poorly compacted embankment zones, or small porous zones (composed of sand or gravel) with changes in resistivity values attributed to changes in atmospheric conditions (air temperature and precipitation). The general observation is that there are large increments in resistivity values in the marked anomalous zones in cases where the difference model is obtained from simultaneous inversion of the datasets acquired in different seasons (wet and dry), for example, Figure 7.4(a) and Figure 7.4(d) are difference models resulting from simultaneous inversion of dataset one and dataset two acquired in October 2015 and December 2015; and in May 2016 and August 2016, respectively. Also, the lowest resistivity values were recorded from November to January, while the highest resistivity values were recorded from May to August.

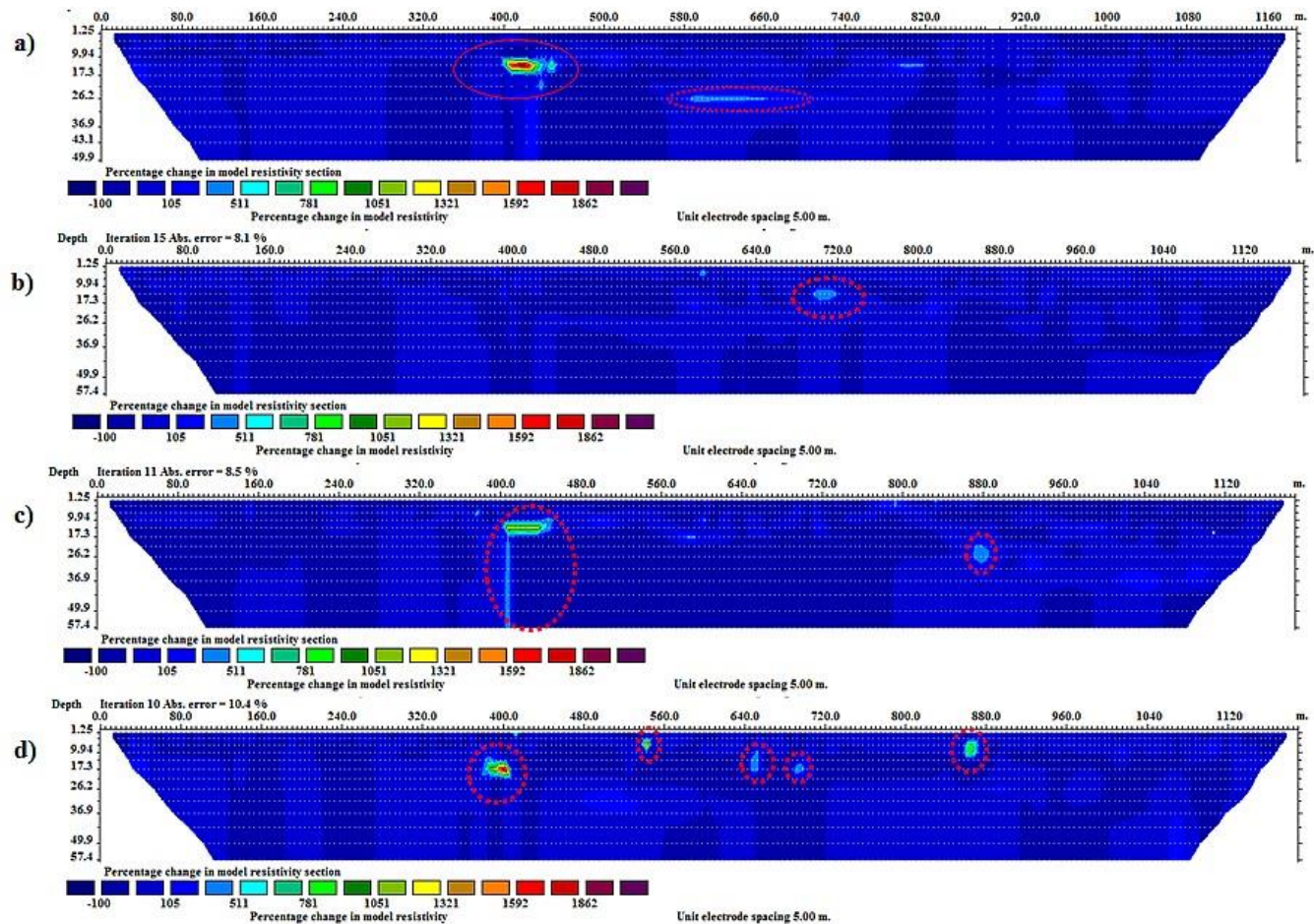


Fig. 7.4: The temporal differences in inverted resistivity models. (a) Difference between the first and the second datasets models with an absolute error of 8.6 %, (b) the difference between the second and third datasets with an absolute error of 8.1 %, (c) difference between the third and fourth datasets with an absolute error of 8.5 %, (d) difference model between the fourth and fifth datasets with an absolute error of 10.4 %. The results obtained are based on the use of a dipole-dipole array of acquisition. The dipole-dipole array is more sensitive to near surface variations, as such, a model with half the unit electrode.

The FDEM results correlate well with the electrical resistivity imaging results. Figure 7.5 show two main layers, the conductive top layer of varying thickness ranging from 10 m to about 38 m, and a more resistive layer extending to the model depth. It is clearly noticed that a vertical anomaly of intermediate resistivity values exist around the 200 m mark along the profile line. This anomaly appears to be about 60 m wide and extends to the base of the model. Another anomaly is observed between 400 m and 450 m, with an estimated width of about 30 m.

In addition to the inverse model, the in-phase profiles in Figure 7.6(a) show a negative symmetrical anomaly midway between the 200 m and 400 m along the profile, at approximately 350 m, for the 3520, 880, 1760, 3520 and 7040 Hz frequencies. A corresponding trough-shaped anomaly is evident in the out-of-phase data (Fig. 7.6(b)). The Out-of- phase response is a bit noisier, but gives the same anomaly observed, except at 3520 Hz. The character of this particular anomaly is typical of a vertical bedrock conductor. The reversal of this trough-shaped anomaly on the 14080 Hz profile at approximately 350 m is a result of the presence of a moderately conductive clay core material overlying the more resistive basement metamorphic rocks.

The FDEM results of this study are consistent with the findings presented by Palacky (1991), as cited in Reynolds (2011) in an investigation over a conductor buried beneath quaternary sediments in northern Ontario, Canada, using the HLEM (Fig. 7.7(a) and Fig.7.7(b)). In that particular investigation an Apex Max-Min I (eight-frequency) system with inter-coil separation of 100 m was used along a 1 km profile, in-phase and quadrature components measured at each frequency. At station 600, just like the quadrature data, the in-phase component goes negative. In addition, and in a similar manner to what we observe in the data used in this thesis, there is a reversal of the trough-shaped anomaly on the quadrature data at 14080 Hz as a result of the presence of a moderately conductive overburden of alternating clay-sand units of varying thicknesses. The results in this thesis do not only demonstrate the utility of FDEM profiling to locate fractures within the basement and beneath the sediments cover, but also support those provided by Palacky. Figure 7.6 and Figure 7.7 show a comparison of the two datasets acquired in different study sites but the same geological setting.

The vertical derivative magnetic anomaly map highlights the main structural elements of the study area. The analytic signal (Figure 6.24) and the ternary (Figure 6.25) maps were used to aid fault recognition, and the NW-SE trending topographic lineament in the aforementioned maps was interpreted as a fault scarp based on its correspondence with the location of a previously mapped fault by the BGS. The orientation and position of this fault scarp corresponds closely with the lineament in the aeromagnetic data set which was independently identified and interpreted as a trace of a fault cross-cutting the basement terrain. In addition, the orientation of this lineament in the aeromagnetic map and the topographic features indicate that the strike of the fault scarp is NW-SE. Just like the ERI and FDEM profiling, the results and interpretation of the transformed aeromagnetic data also suggest a fault line cutting across the dam embankment, hence validating the identification of the fault in both datasets. Beside the data collected in this study, location of the fault in the presented data models corresponds well with its location on the technical drawing (Fig. 5.3) of the Lotsane Dam by SMEC (2012).

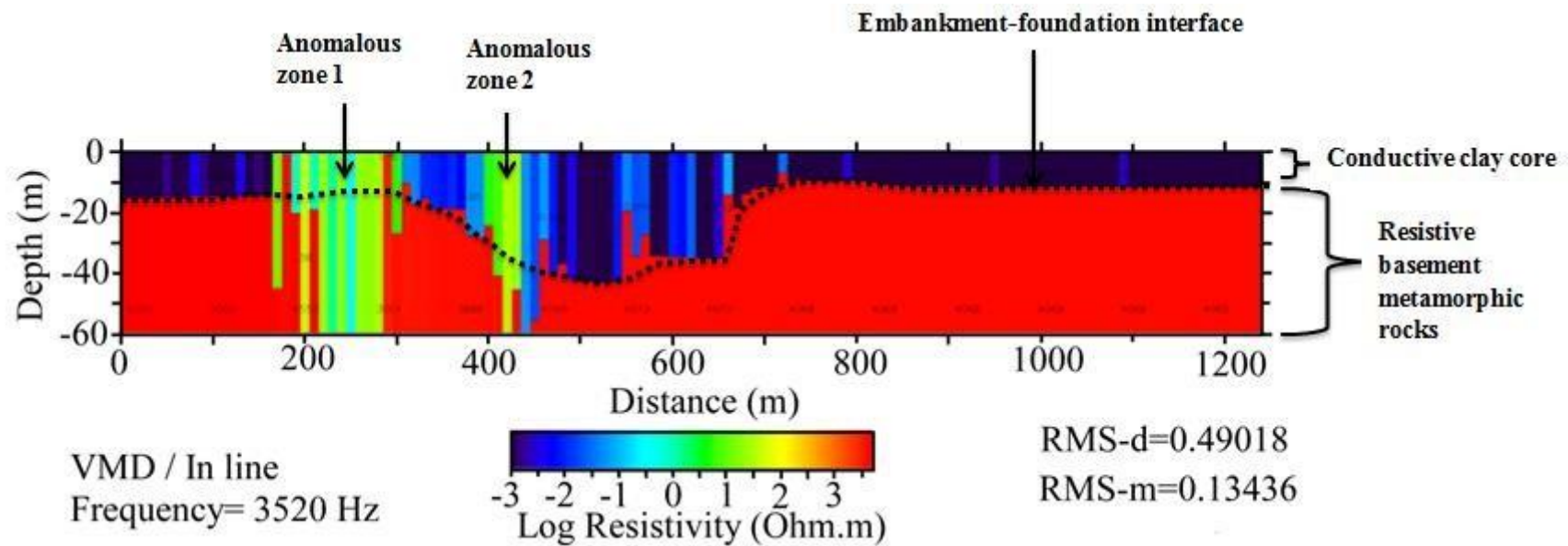


Fig. 7.5: An interpretation model of the FDEM data. The vertical axis show depth values and the horizontal axis represent the distance (in meters) along the profile. The scale is given in logarithm of resistivity, in Ohm.m. The top layer of darker tone of blue represents a conductive clay core layer of varying thickness ranging from 10 m to about 38 m. The underlying layer colored red represent highly resistive or very low conductivity values. Also shown on the model are two anomalous zones of intermediate resistivity values (relative to the conductive top layer and the resistive basement layer) cutting across the two identified resistivity layers, extending to the base of the model. The anomalous zones 1 and 2 are interpreted to represent fractures/ trenches filled with the loose material of the overlying conductive layer.

Figure 7.6(a) and Figure 7.6(b) display the in-phase and out-of-phase components of the EM field measurements from this study. These measurements are compared to those presented by Palacky [1991 (Figure 7.7(a) and Figure 7.7(b))]. The in-phase plots correspond very well with the quadrature/ out-of-phase plots in both datasets. Also shown in the Figure 7.6(a) and Figure 7.6(b) is a fracture at approximately 350 m along the profile covered by clayey material as well as zone interpreted to represent a fault line. Figure 7.7(a) and Figure 7.7(b) show a location of a bedrock conductor at station 600 m covered by Quaternary sediments. In-phase (left) and quadrature (right) data were acquired at the frequencies specified. Coil separation for both datasets is 100 m.

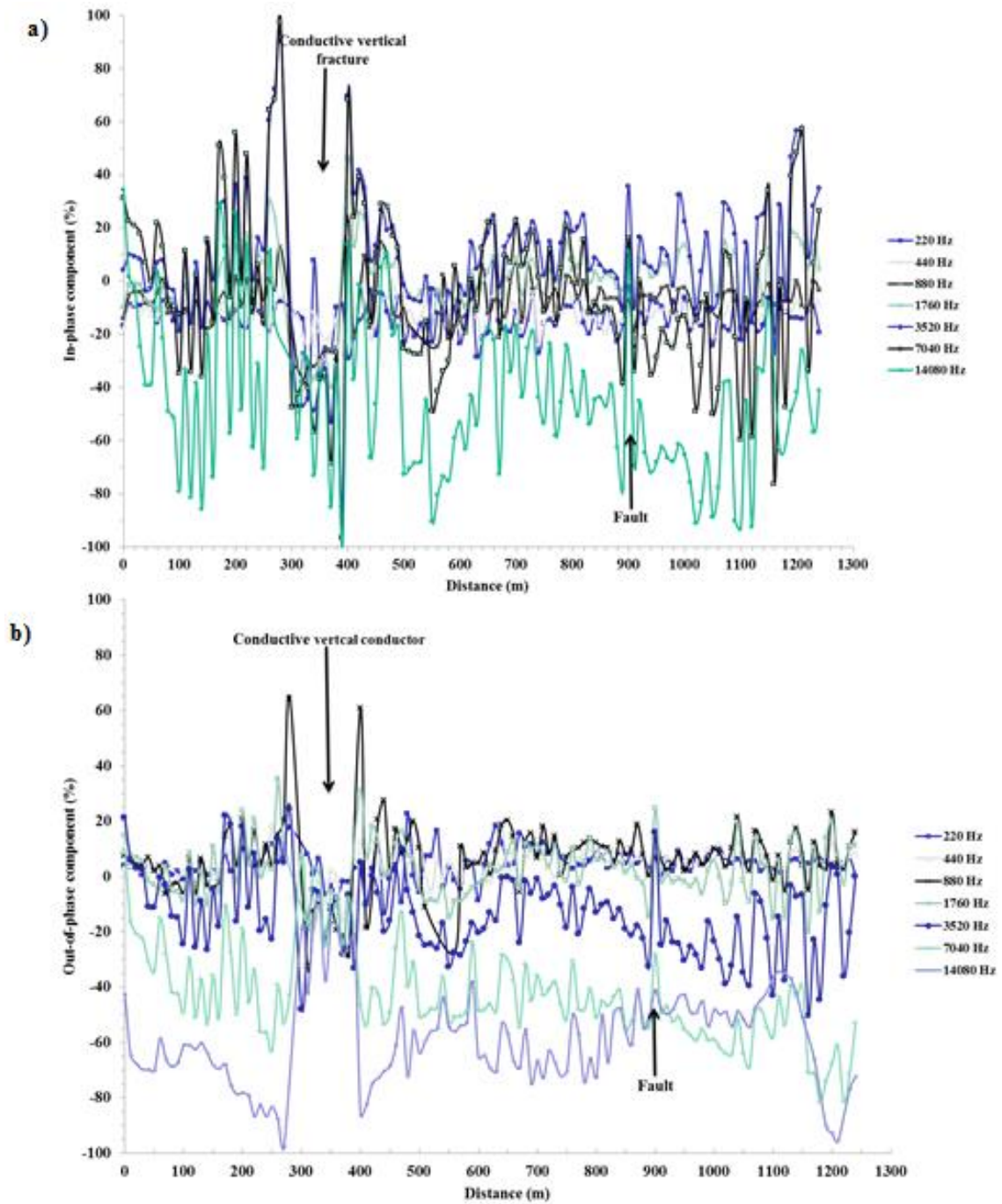


Fig. 7.6: (a) An in-phase component of the secondary EM field, (b) the out-of-phase component of the secondary EM field measurements. A fracture at approximately 350 m along the profile is observed, and a distinct spike at 900 m mark along the profile. Coil separation for both datasets is 100 m.

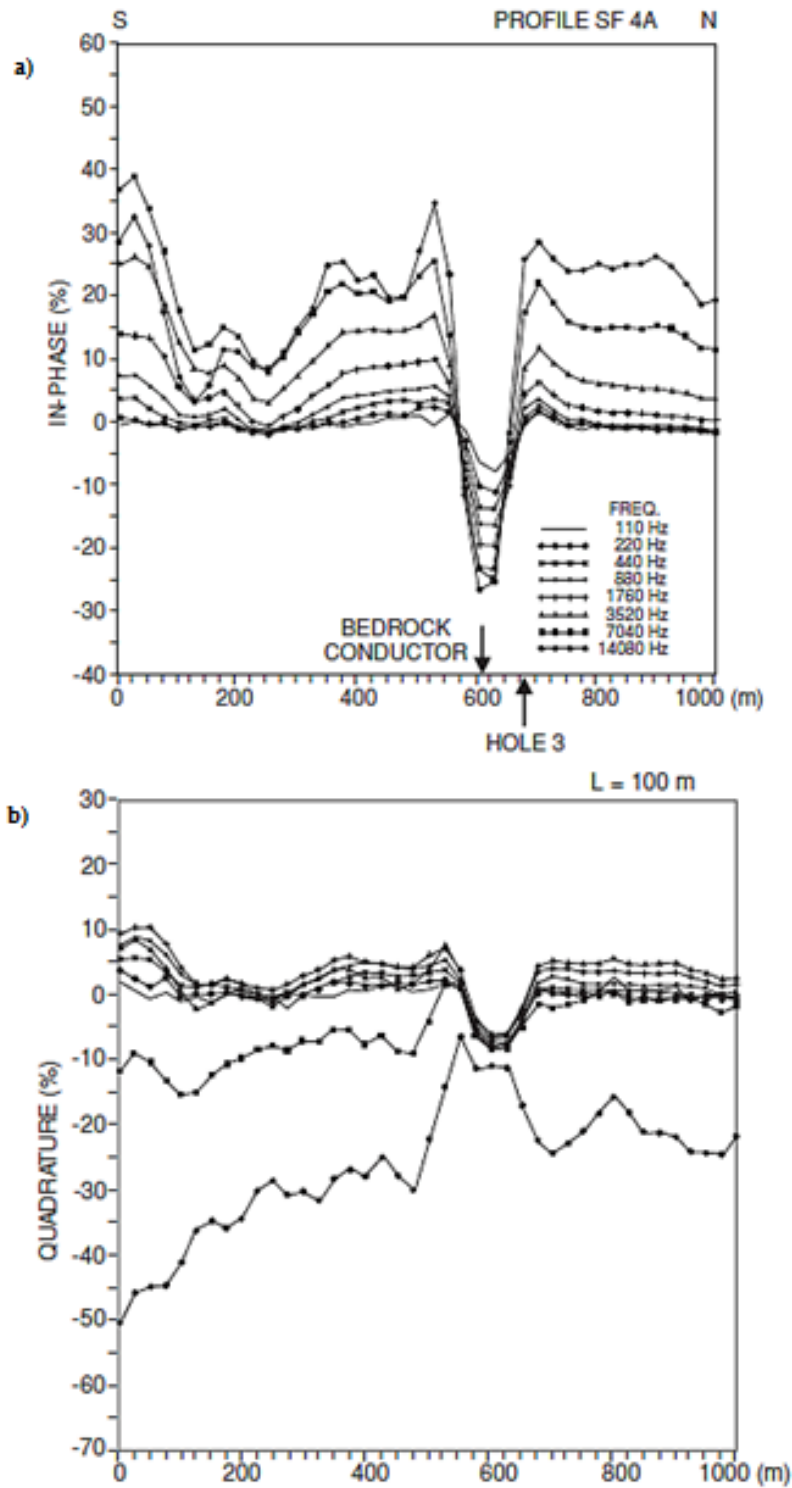


Fig. 7.7: (a) The in-phase plots (b) the out-of-phase plots (from Palacky, 1991, as cited in Reynolds, 2011). Location of a bedrock conductor at station 600 m covered by Quaternary sediments is indicated. In-phase and quadrature data were acquired at the frequencies specified. Coil separation for both datasets is 100 m.

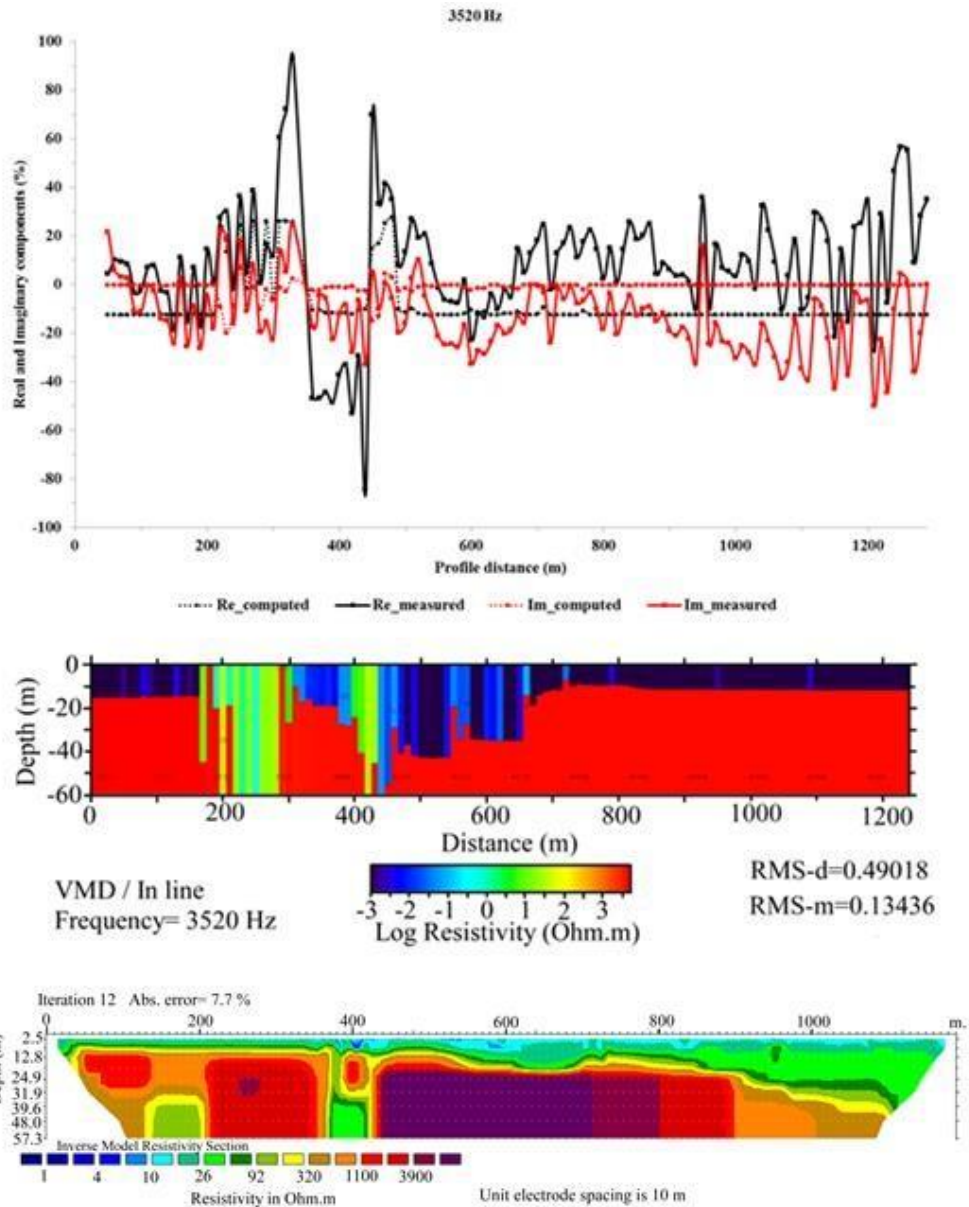


Fig. 7.8: A plot of images showing a comparison of results from (a) frequency domain electromagnetic data profiles, (b) frequency domain electromagnetic data model and (c) 2D dipole-dipole resistivity inverse model. There are coinciding anomalies in the two models, also evident in the profiles display at locations 200 m and 400 m. However, there is a clearly noticed discrepancy beyond the 800 m mark towards the end of the profile in both inverse models, a zone interpreted to represent a fault scarp or a fault line in the resistivity model. In the FDEM model (middle), the thickness of the top conductive layer is 10 m towards the end of the profile, whereas a zone of intermediate resistivity values (green color on the model, resistivity range from 26 to 92 Ωm) underlies the top most conductive layer of thickness not greater than 12.8 m in the resistivity data model (bottom). This zone has a depth extension of about 36 m, ranging from 12.8 m to 48 m. At this particular location on the resistivity model (beyond the 800 m mark), highly weathered basement rock material of resistivity range from 320 Ωm to 1000 Ωm is observed.

8 Conclusions and recommendations

There are existing conventional methods for monitoring seepage in dams; however, they do not always meet the requirements as they do not show the source zones of the likely abnormalous conditions recorded in case the integrity of the dam is compromised. The aim of this study was to identify defects within the dam embankment and its foundation, and to monitor their development over a period of twelve months if found. The following conclusions are drawn from the measurements:

- ❖ Two distinctive layers were identified: The conductive top layer of thickness ranging from 10 m to 25 m in the resistivity models, and thickness range from 10 m to 38 m in the FDEM model corresponding to the clay core, and the bottom layer corresponding to the basement rock.
- ❖ Two anomalous zones were identified in the ERI and FDEM data models, denoted zone 1 and zone 2 in ERI model; anomalous zone 1 and anomalous zone 2 in the FDEM model. Zone 1 in each of the model dataset set is situated about the 200 m whereas zone 2 is situated about the 400 m mark along the profile. These zones are interpreted to represent fractures or manmade trenches that host water pipes and backfilled with concrete or weathered basement rock fragments. Zone 1 appears to be entirely covered with the material initially used (concrete/ weathered basement rock fragments), unlike zone 2, which appears to be open at the embankment-foundation interface, in that the overlying material accumulated in or filled it. Backfilling the trenches/ fractures was intended to seal them such that the stability of the embankment material is not affected. However, the observations from this study suggest that the current status of zone 2 presents a threat to the stability of the overlying embankment material.
- ❖ A contact of the basement rock and the infilling sediments towards the far right end of the resistivity models was interpreted to mark the fault scarp. This result is consistent with the analytic signal filtered aeromagnetic map and previously reported by the BGS as the Lechana Fault and also presented in dam construction documents by SMEC et al. (2012). Faults pose a major hazard to the general condition of the dam, beside the fact that a fault is a channel through which water passes, the fault movement can result in relatively large vertical and horizontal displacements in the dam foundations and structure, with potential

severe consequences. Such consequences include uncontrolled leakage, disruption of drainage and filter elements, as well as distortion of the spillway gates (McMorran & Hull, n.d.).

- ❖ Time-lapse resistivity measurements were acquired to monitor the changes taking place within the dam embankment. Significant changes were identified at zone 2 (400 m mark on the models) and interpreted to be due to loss of fine material by suffusion, leading to increased pore spaces, and due to changes in moisture conditions across the wet and dry seasons.
- ❖ Further investigations need to be done on regular basis to monitor the identified anomalous zones to ensure dam safety and integrity as changes in these anomalous zones over time will be a good indicator that the embankment is failing.

9 References

- Abdelwahab, H. (2013). Comparison of 2D and 3D resistivity imaging methods in the study of shallow subsurface structures. *Greener J. Phys. Sci.*, 3(4), 149-158.
- Aizebeokhai, A. P. (2010). 2D and 3D geoelectrical resistivity imaging: Theory and field design. *Scientific Research and Essays*, 5(23), 3592-3605.
- Al-Saigh, N. H., Mohammed, Z. S., & Dahham, M. S. (1994). Detection of water leakage from dams by self-potential method. *Engineering Geology*, 37(2), 115-121.
- Alwan, I. A. K. (2013). Comparison between Conventional Arrays in 2D Electrical Resistivity Imaging Technique for Shallow Subsurface Structure Detection of the University of Technology. *Eng. &Tech. Journal*, Vol. 31, Part (A), No.10, 2013.
- Ambikaipahan, R. (2011). Failure of an Earth Dam: An analysis of earth dam break-Årbogen dam, Nedre Eiker Municipality, Norway.
- ARUP Botswana (1991). Lotsane Dam Feasibility Study, Final Report, Department of Water Affairs (Unpublished Report).
- Benson, R., Glaccum, R.A., & Noel, M.R. (1983). Geophysical techniques for sensing buried wastes and waste migration, 236p. 6375 Riverside Dr., Dublin OH 43107: National Ground Water Association.
- Bentley, L. R., & Gharibi, M. (2004). Two-and three-dimensional electrical resistivity imaging at a heterogeneous remediation site. *Geophysics*, 69(3), 674-680.
- Bergström, J. (1998). Geophysical methods for investigating and monitoring the integrity of sealing layers on mining waste deposits (Doctoral dissertation, Luleå tekniska universitet).
- Bernard, J. E. A. N. (2003). Short note on the depth of investigation of electrical methods. Unpublished Report.
- Bernard, J., Leite, O., Vermeersch, F., Instruments, I. R. I. S., & Orleans, F. (2006). Multi-electrode resistivity imaging for environmental and mining applications. IRIRS Instrument, Orleans, France.
- Bing, Z., & Greenhalgh, S. A. (1999). Explicit expressions and numerical calculations for the Frechet and second derivatives in 2.5 D Helmholtz equation inversion. *Geophysical Prospecting*, 47(4), 443-468.
- Bing, Z., & Greenhalgh, S. A. (2001). Finite element three dimensional direct current resistivity modelling: accuracy and efficiency considerations. *Geophysical Journal International*, 145(3), 679-688.

- Bolève, A., Revil, A., Janod, F., Mattiuzzo, J. L., & Fry, J. J. (2009). Preferential fluid flow pathways in embankment dams imaged by self-potential tomography. *Near Surface Geophysics*, 7(5-6), 447-462.
- Braithwaite, N. E. (2013). Laboratory modeling of erosion potential of seepage barrier material. Utah State University.
- Brosten, T. R., Llopis, J. L., & Kelley, J. R. (2005). Using geophysics to assess the condition of small embankment dams (No. ERDC/GSL-TR-05-17). Engineer Research and Development Center Vicksburg MS Geotechnical and Structures Lab.
- Burns, B., Barker, R., & Ghataora, G. S. (2006). Investigating internal erosion using a miniature resistivity array. *NDT & E International*, 39(2), 169-174.
- Buselli, G., & Lu, K. (2001). Groundwater contamination monitoring with multichannel electrical and electromagnetic methods. *Journal of Applied Geophysics*, 48(1), 11-23.
- Butler, D. K., & Llopis, J. L. (1990). Assessment of anomalous seepage conditions. *Geotechnical and environmental geophysics*, 2, 153-173.
- Carney, J. N., Aldiss, D. T., & Lock, N. P. (1994). The geology of Botswana, Geological Survey Department, Republic of Botswana, (Unpublished Report).
- Case, J. S. (2012). Inspection of earthen embankment dams using time lapse electrical resistivity tomography. roQuest Dissertations and Theses, 51-01, 124p.
- Chang, D. S., & Zhang, L. M. (2013). Extended internal stability criteria for soils under seepage. *Soils and Foundations*, 53(4), 569-583.
- Charles, J. A. (1993). Embankment dams and their foundations: safety evaluation for static loading. In *Dam Safety Evaluation. Proceedings of International Workshop (Vol. 4, pp. 47-75)*. Sutton, Surrey: Dam Engineering.
- Charles, J. A. (1996). Investigating embankment dams: a guide to the identification and repair of defects. Building Research Establishment.
- Chen, W., Xuanqing, Z., Naihua, H., & Yonghong, M. (1996). Compiling the map of shallow-buried palaeochannels on the North China Plain. *Geomorphology*, 18(1), 47-52.
- Claerbout, J. F., & Muir, F. (1973). Robust modeling with erratic data. *Geophysics*, 38(5), 826-844.
- Coggon, J. H. (1971). Electromagnetic and electrical modeling by the finite element method. *Geophysics*, 36(1), 132-155.
- Contreras, I. A., & Hernández, S. H. (2013). Techniques for prevention and detection of leakage in dams and reservoirs.

- Cyganiewicz, J. M., Engemoen, W. O., & Redlinger, C. G. (2007). Bureau of Reclamation experience with evaluating internal erosion of embankment dams. *Internal Erosion of dams and their foundations*, 55-64.
- Dahlin, T. (2001). The development of DC resistivity imaging techniques. *Computers & Geosciences*, 27(9), 1019-1029.
- Dahlin, T., & Johansson, S. (1995). Resistivity variations in an earth embankment dam in Sweden. In 1st EEGS Meeting.
- Daily, W., Ramirez, A., Binley, A., & LeBrecque, D. (2004). Electrical resistance tomography. *The Leading Edge*, 23(5), 438-442.
- Daily, W., Ramirez, A., LaBrecque, D., & Nitao, J. (1992). Electrical resistivity tomography of vadose water movement. *Water Resources Research*, 28(5), 1429-1442.
- de Lima, O. A., & Sharma, M. M. (1990). A grain conductivity approach to shaly sandstones. *Geophysics*, 55(10), 1347-1356.
- deGroot-Hedlin, C., & Constable, S. (1990). Occam's inversion to generate smooth, two-dimensional models from magnetotelluric data. *Geophysics*, 55(12), 1613-1624.
- Denchik, N., & Chapellier, D. (2005). 3D electrical resistivity monitoring during rainfalls. In *Proceeding of the Paper Presented at the 3rd Swiss Geoscience Meeting*.
- Dey, A., & Morrison, H. F. (1979a). Resistivity modelling for arbitrarily shaped two-dimensional structures. *Geophysical Prospecting*, 27(1), 106-136.
- Dey, A., & Morrison, H. F. (1979b). Resistivity modeling for arbitrarily shaped three-dimensional structures. *Geophysics*, 44(4), 753-780.
- Dunbar, J. B., Ballard, R. F., Murphy, W. L., McGill, T. E., Llopis, J. L., Peyman-Dove, L. D., & Bishop, M. J. (2003). Condition assessment of the US International Boundary and Water Commission, Lower Rio Grande Valley levees, south Texas. Vol I, Main Text and Appendices. ERDC TR-03-4. Vicksburg, MS: US Army Engineer Research and Development Center.
- Ersayın, D. (2006). Studying seepage in a body of earth-fill dam by (Artificial Neural Networks) ANNs (Master's thesis, İzmir Institute of Technology).
- Farooq, M., Park, S., Kim, J. H., Song, Y. S., Amjad Sabir, M., Umar, M., Tariq, M., & Muhammad, S. (2014). Time-lapse electrical resistivity investigations for imaging the grouting injection in shallow subsurface cavities. *The Scientific World Journal*, 2014.
- Farquharson, C. G., & Oldenburg, D. W. (1998). Non-linear inversion using general measures of data misfit and model structure. *Geophysical Journal International*, 134(1), 213-227.

Federal Energy Regulatory Commission. (2005). Dam Safety Performance Monitoring Program. Federal Energy Regulatory Commission, Washington, DC, USA.

Fell, R., Foster, M. A., Cyganiewicz, J., Sills, G., Vroman, N., & Davidson, R. (2008). Risk Analysis for Dam Safety: A Unified Method for Estimating Probabilities of Failure of Embankment Dams by Internal erosion and Piping. UNICIV Report No. R 446, Version: Delta, (2).

Fell, R., FOSTER, M., & Wan, C. F. (2005). A framework for assessing the likelihood of internal erosion and piping of embankment dams and their foundations. In Contribution to the Workshop of internal erosion and piping of dams and foundations. Aussoise, France, April (Vol. 5).

Fell, R., & Fry, J. J. (2007). Internal Erosion of Dams and Their Foundations: Selected and Reviewed Papers from the Workshop on Internal Erosion and Piping of Dams and Their Foundations, Aussois, France, 25–27 April 2005. Taylor & Francis Group.

Fell, R., MacGregor, P., & Stapledon, D. (1992). Geotechnical engineering of embankment dams. . ISBN 90 5410 128 8, Balkema, Rotterdam, pp 675

Fell, R., Wan, C. F., Cyganiewicz, J., & Foster, M. (2003). Time for development of internal erosion and piping in embankment dams. Journal of Geotechnical and Geoenvironmental Engineering, 129(4), 307-314.

FEMA (2005). Conduits through Embankment Dams: Best Practices for Design, Construction, Problem Identification and Evaluation, Inspection, Maintenance, Renovation and Repair, Federal Emergency Management Agency, Washington, DC.

Flores-Berrones, R., & Lopez-Acosta, N. P. (2011). Internal Erosion Due to Water Flow Through Earth Dams and Earth Structures. INTECH Open Access Publisher.

Foster, M. A., & Fell, R. (1999). Filter Testing for Dams—no erosion and continuing erosion boundaries. In Proc. 8th Australia New Zealand Conf. on Geomechanics. Hobart (Vol. 2, pp. 503-512).

Foster, M., & Fell, R. (2001). Assessing embankment dam filters that do not satisfy design criteria. Journal of Geotechnical and Geoenvironmental Engineering, 127(5), 398-407.

Foster, M. A., Fell, R., Davidson, R., & Wan, C. F. (2002). Estimation of the probability of failure of embankment dams by internal erosion and piping using event tree methods. ANCOLD Bulletin, 75-88.

Foster, M., Fell, R., & Spannagle, M. (2000a). The statistics of embankment dam failures and accidents. Canadian Geotechnical Journal, 37(5), 1000-1024.

Fox, R. C., Hohmann, G. W., Killpack, T. J., & Rijo, L. (1980). Topographic effects in resistivity and induced-polarization surveys. *Geophysics*, 45(1), 75-93.

Ganse, A. A. (2008). *A Geophysical Inverse Theory Primer*. University of Washington: Applied Physics Laboratory and Department of Earth and Space Sciences, Princeton: Princeton University Press.

Gardi, S. Q. S. (2014). 2D Electrical Resistivity Tomography Survey for Shallow Environmental Study at Wastewater Valley of Southwestern Erbil City, Iraqi Kurdistan Region. *Research Journal of Environmental and Earth Sciences*, 6 (5), 266-277.

Garner, S. J., & Fannin, R. J. (2010). Understanding internal erosion: a decade of research following a sinkhole event. *The International Journal on Hydropower & Dams*, 17(3), 93

Geoflux, (2001). *Environmental Impact Assessment for the Detailed Design of a Dam on the Lotsane River at Maunatlala: Final EIA Report, December 2001 for the Department of Water Affairs, Botswana Government Ministry of Minerals, Energy and water affairs Department of Water affairs.*

Gilson, E. W., Nimeck, G., Bauman, P. D., & Kellett, R. (2000, February). Groundwater exploration in prairie environments. In *Proceedings of the Symposium on the Application of Geophysics to Engineering and Environmental Problems: Wheat Ridge, Colorado*, Environmental and Engineering Geophysical Society (pp. 955-959).

Griffiths, D. H., & Barker, R. D. (1993). Two-dimensional resistivity imaging and modelling in areas of complex geology. *Journal of Applied Geophysics*, 29(3), 211-226.

Hayley, K., Pidlisecky, A., & Bentley, L. R. (2011). Simultaneous time-lapse electrical resistivity inversion. *Journal of Applied Geophysics*, 75(2), 401-411.

Higgins, P. (1983). Advances in leak detection systems. 2. *Pipe line Industry*, 58(4), 55.

Hoeg, K. (2002). Embankment-dam engineering, safety evaluation and upgrading. In *proceedings of the International conference on Soil Mechanics and Geotechnical Engineering (Vol. 4, pp. 2491-2504)*. AA Balkema Publishers.

Hunter, R. P. (2012). *Development of Transparent Soil Testing using Planar Laser Induced Fluorescence in the Study of Internal Erosion of Filters in Embankment Dams.*

Ibeneme, S. I., Ibe, K. K., Selemo, A. O., Nwagbara, J. O., Obioha, Y. E., Echendu, K. O., & Ubechu, B. O. (2013). Geoelectrical Investigation of a Proposed Dam Site in a Sedimentary Terrain: Case Study of Aba River at Amapu-Ideobia, Akanu Ngwa Southeastern Nigeria. *International Journal of Geosciences*, 2013.

ICOLD. (1987). *Dam safety guidelines*. International Commission on Large Dams, Bulletin no. 59, ISSN 0534-8293, p185

ICOLD. (1995). *Dam failures: statistical analysis*. International Commission on Large Dams, Bulletin no. 99.

Ikard, S. (2013). *Geoelectric monitoring of seepage in porous media with engineering applications to earthen dams*. Colorado School of Mines.

- Jansen, R. B. (Ed.). (1989). *Advanced dam engineering for design, construction, and rehabilitation*. Springer Science & Business Media.
- Jansen, R. B., Aldrich, H. P., & David, S. D. (1983). *Safety of existing dams: Evaluation and Improvement*. Washington DC. National Academy of Sciences.
- Jika, H. T., & Mamah, L. I. (2014). Application Of Electromagnetic Method And Electrical Resistivity Sounding In Hydrogeological Studies, A Case Study Of Vandeikya Area, Central Nigeria. *International Journal of Scientific and Technology Research*, 3(2), 179-190.
- Johansson, S. (1997). *Seepage monitoring in embankment dams* (Doctoral dissertation, Institutionen för anläggning och miljö).
- Johansson, S., Bartsch, M., Landin, O., Barmen, G., Dahlin, T., & Ulriksen, P. (1995). Nyare metoder för tillståndskontroll av fyllningsdammar. VASO dammkommittés rapport nr 21, 21.
- Johansson, S., & Dahlin, T. (1996). Seepage monitoring in an earth embankment dam by repeated resistivity measurements. *European Journal of Engineering and Environmental Geophysics*, 1(3), 229-247.
- Karaoulis, M. C., Kim, J. H., & Tsourlos, P. I. (2011). 4D active time constrained resistivity inversion. *Journal of Applied Geophysics*, 73(1), 25-34.
- Kaspar, F., Helmschrot, J., Mhanda, A., Butale, M., de Clercq, W., Kanyanga, J.K., Neto, F.O.S., Kruger, S., Castro Matsheka, M., Mucbe, G. and Hillmann, T. (2016). The SASSCAL contribution to climate observation, climate data management and data rescue in Southern Africa. *Advances in science and research*, 12, pp.171-177.
- Kaufmann, M. (2014). *Pseudo 2D inversion of multi-frequency coil-coil FDEM data* (Doctoral dissertation, Master's thesis, IDEA League, ETH Zurich).
- Ke, L., & Takahashi, A. (2012a). Strength reduction of cohesionless soil due to internal erosion induced by one-dimensional upward seepage flow. *Soils and Foundations*, 52(4), 698-711.
- Ke, L., & Takahashi, A. (2012b). Influence of internal erosion on deformation and strength of gap-graded non-cohesive soil. In *Proceedings of the Sixth International Conference on Scour and Erosion*, Paris (pp. 847-854).
- Kearey, P., Brooks, M., & Hill, I. (2002). *An introduction to geophysical exploration*. John Wiley & Sons.
- Keller, G. V. Frischknecht (1966). *Electrical methods in geophysical prospecting*. Pergamon Press, New York.
- Key, R.M. & Jones, M.T., (1978). The Palapye Group, central-eastern Botswana. *Transactions Geological Society of South Africa*, 81, 61-73

- Khalil, M. A., & Santos, F. A. M. (2009). Influence of degree of saturation in the electric resistivity–hydraulic conductivity relationship. *Surveys in geophysics*, 30 (6), 601-615.
- Kim, K. J., & Cho, I. K. (2011). Time-lapse inversion of 2D resistivity monitoring data with a spatially varying cross-model constraint. *Journal of Applied Geophysics*, 74(2), 114-122.
- Kim, H. S., Oh S. H., Park, H.G., Chung, H. J., Shon, H. W., Kim, K. S. & Lim, H. D. (2004). Electrical resistivity imaging for comprehensive evaluation of earth-rock dam seepage and safety. *Procs. International Commission on Large Dams (ICOLD), 72nd Annual Meeting*, 16-22. May 2004, Seoul, Korea: 123-134
- Kinabo, B. D. (2007). *Incipient continental rifting: insights from the Okavango Rift Zone, northwestern Botswana*. Missouri University of Science and Technology.
- LaBrecque, D. J., & Yang, X. (2001). Difference inversion of ERT data: A fast inversion method for 3-D in situ monitoring. *Journal of Environmental & Engineering Geophysics*, 6(2), 83-89.
- Lagerlund, J. (2009). *Remedial injection grouting of embankment dams with non-hardening grouts* (Doctoral dissertation, KTH).
- Letellier, M. (2012). *A practical assessment of frequency electromagnetic inversion in a near surface geological environment*. Dissertations in Geology at Lund University.
- Lin, C. P., Hung, Y. C., Yu, Z. H., & Wu, P. L. (2013). Investigation of abnormal seepages in an earth dam using resistivity tomography. *Journal of Geoengineering*, 8(2), 61-70.
- Lines, L. R., & Treitel, S. (1984). Tutorial: A review of least-squares inversion and its application to geophysical problems. *Geophysical prospecting*, 32(2), 159-186.
- Loke, M. H. (1994). *The inversion of two-dimensional resistivity data* (Doctoral dissertation, University of Birmingham).
- Loke, M. H. (1999). *Electrical imaging surveys for environmental and engineering studies: a practical guide to 2D and 3D surveys*. 5, Cangkat Minden Lorong 6, Minden Heights, 11700. Penang, Malaysia (mhoke@ pc. jaring. my).
- Loke, M. H. (2000). Topographic modelling in resistivity imaging inversion. In *62nd EAGE Conference & Technical Exhibition Extended Abstracts*, D-2.
- Loke, M. H. (2001). Constrained time-lapse resistivity imaging inversion. In *Symposium on the Application of Geophysics to Engineering and Environmental Problems 2001* (pp. EEM7-EEM7). Society of Exploration Geophysicists.

Loke, M. H. (2002). RES2DMOD Version 3.01. Rapid 2D resistivity forward modeling using the finite-difference and finite element methods. Software manual, www.geoelectrical.com.

Loke, M. H. (2004). User's Manual for RES2DINV Software. Geotomo Software, 128.

Loke, M. H. (2007). Rapid 2-D Resistivity and IP inversion using the least-squares method, Geoelectrical Imaging 2D and 3D. Geotomo Software, Malaysia.

Loke, M. H., Acworth, I., & Dahlin, T. (2003). A comparison of smooth and blocky inversion methods in 2D electrical imaging surveys. *Exploration Geophysics*, 34(3), 182-187.

Loke, M. H., & Barker, R. D. (1995). Least-squares deconvolution of apparent resistivity pseudo sections. *Geophysics*, 60(6), 1682-1690.

Loke, M. H., & Barker, R. D. (1996). Rapid least-squares inversion of apparent resistivity pseudo sections by a quasi-Newton method. *Geophysical prospecting*, 44(1), 131-152.

Loke, M.H., Chambers, J.E., & Kuras, O. (2011). "Instrumentation, electrical resistivity." In *Solid Earth Geophysics Encyclopedia* (2nd Edition), Electrical & Electromagnetic, Gupta, Harsh (Ed), 599–604. 2nd ed. Berlin: Springer.

Loke, M. H., Chambers, J. E., Rucker, D. F., Kuras, O., & Wilkinson, P. B. (2013). Recent developments in the direct-current geoelectrical imaging method. *Journal of Applied Geophysics*, 95, 135-156.

Loke, M. H., & Dahlin, T. (2002). A comparison of the Gauss–Newton and quasi-Newton methods in resistivity imaging inversion. *Journal of Applied Geophysics*, 49(3), 149-162.

Lowrie, W. (2007). *Fundamentals of geophysics*. Cambridge university press.

Maganti, D. (2008). *Subsurface investigations using high resolution resistivity*. ProQuest.

Marchetti, M., & Settimi, A. (2010). Integrated geophysical measurements on a test site for detection of buried steel drums. *ArXiv preprint arXiv: 1009.5555*.

Marot, D., Alexis, A., & Bendahmane, F. (2007). Internal erosion of dams and their foundations. A specific triaxial device for the study of internal erosion on cohesive soils, 159-165.

Masannat, Y. M. (1980). Development of piping erosion conditions in the Benson area, Arizona, USA. *Quarterly Journal of Engineering Geology and Hydrogeology*, 13(1), 53-61.

Mattsson, H., Hellström, J. G. I., & Lundström, T. S. (2008). On internal erosion in embankment dams. *Research Rep*.

- McMorran, T., & Hull, A. (n.d.) Fault rupture hazard assessments for dam foundations: examples from contrasting tectonic environments.
- Miller, C. R., Routh, P. S., Brosten, T. R., & McNamara, J. P. (2008). Application of time-lapse ERT imaging to watershed characterization. *Geophysics*, 73(3), G7-G17.
- Milson, J. (2003). *Field Geophysics, The geological field guide series*. University College London.
- Minsley, B. J., Smith, B. D., Hammack, R., Sams, J. I., & Veloski, G. (2012). Calibration and filtering strategies for frequency domain electromagnetic data. *Journal of Applied Geophysics*, 80, 56-66.
- Montaj, G. O. (2013). *Software for earth science mapping and processing*. Geosoft Incorporation Ltd.
- Mori, G. (2009). *The use of Ground Penetrating Radar and alternative geophysical techniques for assessing embankments and dykes safety (Doctoral dissertation, alma)*.
- Mufti, I. R. (1976). Finite-difference resistivity modeling for arbitrarily shaped two-dimensional structures. *Geophysics*, 41(1), 62-78.
- Narita, K. (2000). *Design and construction of embankment dams*. Dept. of Civil Eng., Aichi Institute of Technology.
- Nilsson, Å. (1995). *Beprövade metoder för tillståndskontroll av fyllningsdammar*. (In Swedish with English summary).
- Nilsson, Å., & Rönnqvist, H. (2004). Measures to strengthening embankment dams in order to stop or control a possible through-flow process. In *International Seminar, Stability and Breaching of Embankment Dams*, Oslo, Norway.
- Noel, M., & Xu, B. (1991). Archaeological investigation by electrical resistivity tomography: a preliminary study. *Geophysical Journal International*, 107(1), 95-102.
- Nordiana, M. M., Rosli, S., Mokhtar, S. M., Nawawi, N. M., & Azwin, I. N. (2012). Imaging Subsurface Characterization at Bukit Bunuh Using 2D Resistivity Method: The Effectiveness of Enhancing Horizontal Resolution (EHR) Technique. *International Journal of Environmental Science and Development*, 3(6), 569.
- Novák, P., Moffat, A. I. B., Nalluri, C., & Narayanan, R. (2007). *Hydraulic structures*. CRC Press.
- Ogungbe, A. S., Olowofela, J. A., Da-Silva, O. J., Alabi, A. A., & Onori, E. O. (2010). Subsurface Characterization using Electrical Resistivity (Dipole-Dipole) method at Lagos State University (LASU) Foundation School, Badagry. *Applied Science Research*, 1(1), 131-145.

- Oldenburg, D. W., & Li, Y. (1999). Estimating depth of investigation in DC resistivity and IP surveys. *Geophysics*, 64(2), 403-416.
- Oldenborger, G. A., Knoll, M. D., Routh, P. S., & LaBrecque, D. J. (2007). Time-lapse ERT monitoring of an injection/withdrawal experiment in a shallow unconfined aquifer. *Geophysics*, 72(4), F177-F187.
- Opeyemi, F. A. (2013). Integrated Geophysical Characterization of Subsurface conditions around Ilesha Dumpsite: Case of South-western Nigeria. *Asian Journal of Applied Science and Engineering*, 2(2), 84-95.
- Osazuwa, I. B., & Chii, E. C. (2010). Two-dimensional electrical resistivity survey around the periphery of an artificial lake in the Precambrian basement complex of northern Nigeria. *International Journal of Physical Sciences*, 5(3), 238-245.
- Osazuwa, I. B., & Chinedu, A. D. (2008). Seismic refraction tomography imaging of high- permeability zones beneath an earthen dam, in Zaria area, Nigeria. *Journal of Applied Geophysics*, 66(1), 44-58.
- Oskooi, B. (2004). A broad view on the interpretation of electromagnetic data (VLF, RMT, MT, CSTMT) (Doctoral dissertation, Acta Universitatis Upsaliensis).
- Oyedele, K. F., Oladele, S., & Adesanya, O. (2013). Identification of Competent Geologic Layers Using Geophysical and Geo-Engineering Methods at Okunmopo, Lagos, Nigeria. *International Journal of Advanced Scientific and Technical Research*, 4(3), 227-238.
- Panthulu, T. V., Krishnaiah, C., & Shirke, J. M. (2001). Detection of seepage paths in earth dams using self-potential and electrical resistivity methods. *Engineering Geology*, 59(3), 281-295.
- Parasnis, D. S. (1997). Principles of applied geophysics. ISBN 0-412-64080-5, Chapman & Hall, London, p 429.
- Pierce, K. S., Liechty, D. J., Rittgers, J. B. & Markiewicz, R. D. (2012). Geophysical Investigation. Electrical Resistivity Surveys. Managing water in the west. U.S Department of Seismotectonics and Geophysics group. Technical memorandum No. TM-86-68330-2012-23.
- Pirttijärvi, M. (2011). Laterally constrained 1-D inversion of EM profile data. Users guide to version 1.2. University of Oulu.
- Pridmore, D. F., Hohmann, G. W., Ward, S. H., & Sill, W. R. (1981). An investigation of finite-element modeling for electrical and electromagnetic data in three dimensions. *Geophysics*, 46(7), 1009-1024.
- Queralt, P., Pous, J., & Marcuello, A. (1991). 2-D resistivity modeling: An approach to arrays parallel to the strike direction. *Geophysics*, 56(7), 941-950.

- Ramage, J. M., Gardner, T. W., & Sasowsky, I. D. (1998). Early Pleistocene Glacial Lake Lesley, West Branch Susquehanna River valley, central Pennsylvania. *Geomorphology*, 22(1), 19-37.
- Reynolds, J. M. (2007). *An introduction to applied and environmental geophysics*. ISBN 0-471-95555-8, John Wiley & Sons, Chichester, p 796
- Reynolds, J. M. (2011). *An introduction to applied and environmental geophysics*. ISBN 978-0-471-48535-3, John Wiley & Sons.
- Robert, T., Caterina, D., Deceuster, J., Kaufmann, O., & Nguyen, F. (2012). A salt tracer test monitored with surface ERT to detect preferential flow and transport paths in fractured/karstified limestones. *Geophysics*, 77(2), B55-B67.
- Robinson, E. S. & Coruh, C. (1988). *Basic exploration geophysics*. ISBN 0-471-61279-0, Wiley, New York
- Rönnqvist, H. (2010). *Predicting surfacing internal erosion in moraine core dams (Doctoral dissertation, KTH)*.
- Rozycki, A., Fonticiella, J. R., & Cuadra, A. (2006). Detection and evaluation of horizontal fractures in earth dams using the self-potential method. *Engineering Geology*, 82(3), 145-153.
- Sakindi, G. (2012). *Analyzing the subsurface resistivity structure on two profiles across the Námafjall high-temperature geothermal field, NE-Iceland, through 1D joint inversion of TEM and MT data*.
- Samouëlian, A., Cousin, I., Tabbagh, A., Bruand, A., & Richard, G. (2005). Electrical resistivity survey in soil science: a review. *Soil and Tillage research*, 83(2), 173-193.
- Sasaki, Y. (1994). 3-D resistivity inversion using the finite-element method. *Geophysics*, 59(12), 1839-1848.
- Scheuermann, A., & Kiefer, J. (2010). Internal erosion of granular materials—Identification of erodible fine particles as a basis for numerical calculations. In 9th International Congress of the Hellenic Society of Theoretical and Applied Mechanics (HSTAM) (pp. 275-282). Hellenic Society for Theoretical & Applied Mechanics (HSTAM).
- Sheffer, M. R. (2002). *Response of the self-potential method to changing seepage conditions in embankment dams (Doctoral dissertation, University of British Columbia)*.
- Sherard, J. L. (1963). *Earth and earth-rock dams*. John Wiley and Sons, New York.
- Sherard, J. L. (1986). Hydraulic fracturing in embankment dams. *Journal of Geotechnical Engineering*, 112(10), 905-927.

- Sherard, J. L. (1992). Sinkholes in dams of coarse, broadly graded soils. *Geotechnical Special Publication*, (32), 324-335.
- Sherard, J. L., Dunnigan, L. P., & Talbot, J. R. (1984). Filters for silts and clays. *Journal of Geotechnical Engineering*, 110(6), 701-718.
- Silvester, P. P., & Ferrari, R. L. (1983). *Finite Element for Electrical Engineers*, Cambridge Uni. Press, Cambridge, UK.
- Sjödahl, P. (2006). Resistivity investigation and monitoring for detection of internal erosion and anomalous seepage in embankment dams. *Engineering Geology*, Lund University.
- Sjödahl, P., Dahlin, T., Johansson, S., & Loke, M. H. (2008). Resistivity monitoring for leakage and internal erosion detection at Hällby embankment dam. *Journal of Applied Geophysics*, 65(3), 155-164.
- Slater, L., Binley, A. M., Daily, W., & Johnson, R. (2000). Cross-hole electrical imaging of a controlled saline tracer injection. *Journal of applied geophysics*, 44(2), 85-102.
- SMEC, (2012). Tapping into Africa's Hydropower Potential, Department of Water Affairs, Botswana. (Unpublished Report).
- Smith, R. C., & Sjogren, D. B. (2006). An evaluation of electrical resistivity imaging (ERI) in Quaternary sediments, southern Alberta, Canada. *Geosphere*, 2 (6), 287-298.
- Song, S. H., Song, Y., & Kwon, B. D. (2005). Application of hydrogeological and geophysical methods to delineate leakage pathways in an earth fill dam. *Exploration Geophysics*, 36(1), 92-96.
- Telford, W. M., & Sheriff, R. E. (1990). *Applied geophysics (Vol. 1)*. Cambridge University Press.
- Terzaghi, K., Peck, R. B., & Mesri, G. (1996). *Soil mechanics in engineering practice*. John Wiley & Sons, New York.
- Timberlake, J. R. (1980). Vegetation map of south eastern Botswana. Gaborone: Ministry of Agriculture, Range Ecology Sec. IV, 83p.-maps.. En Includes plant list. *Maps. Geog.* 5.
- Tsourlos, P., Ogilvy, R., Meldrum, P., & Williams, G. (2003). Time-lapse monitoring in single boreholes using electrical resistivity tomography. *Journal of Environmental & Engineering Geophysics*, 8(1), 1-14.
- Vazquez Borragan, A. (2014). Modelling internal erosion within an embankment dam prior to breaching.

- Vickery, A. C., & Hobbs, B. A. (2002). The effect of subsurface pipes on apparent resistivity measurements. *Geophysical prospecting*, 50(1), 1-13.
- Wan, C. F., & Fell, R. (2004). Investigation of rate of erosion of soils in embankment dams. *Journal of Geotechnical and Geoenvironmental Engineering*, 130(4), 373-380.
- Ward, S. H. (1980). Electrical, electromagnetic, and magnetotelluric methods. *Geophysics*, 45(11), 1659-1666.
- Ward, S. H. (1990). Resistivity and induced polarization methods. *Geotechnical and environmental geophysics*, 1, 147-189.
- Wightman, W. E., Jalinoos, F., Sirles, P., & Hanna, K. (2003). Application of Geophysical Methods to Highway Related Problems. Federal Highway Administration, Central Federal Lands Highway Division, Lakewood, CO, Publication No. FHWA-IF-04-021.
- Zarroca, M., Linares, R., Velásquez-López, P. C., Roqué, C., & Rodríguez, R. (2015). Application of electrical resistivity imaging (ERI) to a tailings dam project for artisanal and small-scale gold mining in Zaruma-Portovelo, Ecuador. *Journal of Applied Geophysics*, 113, 103-113.

APPENDIX A

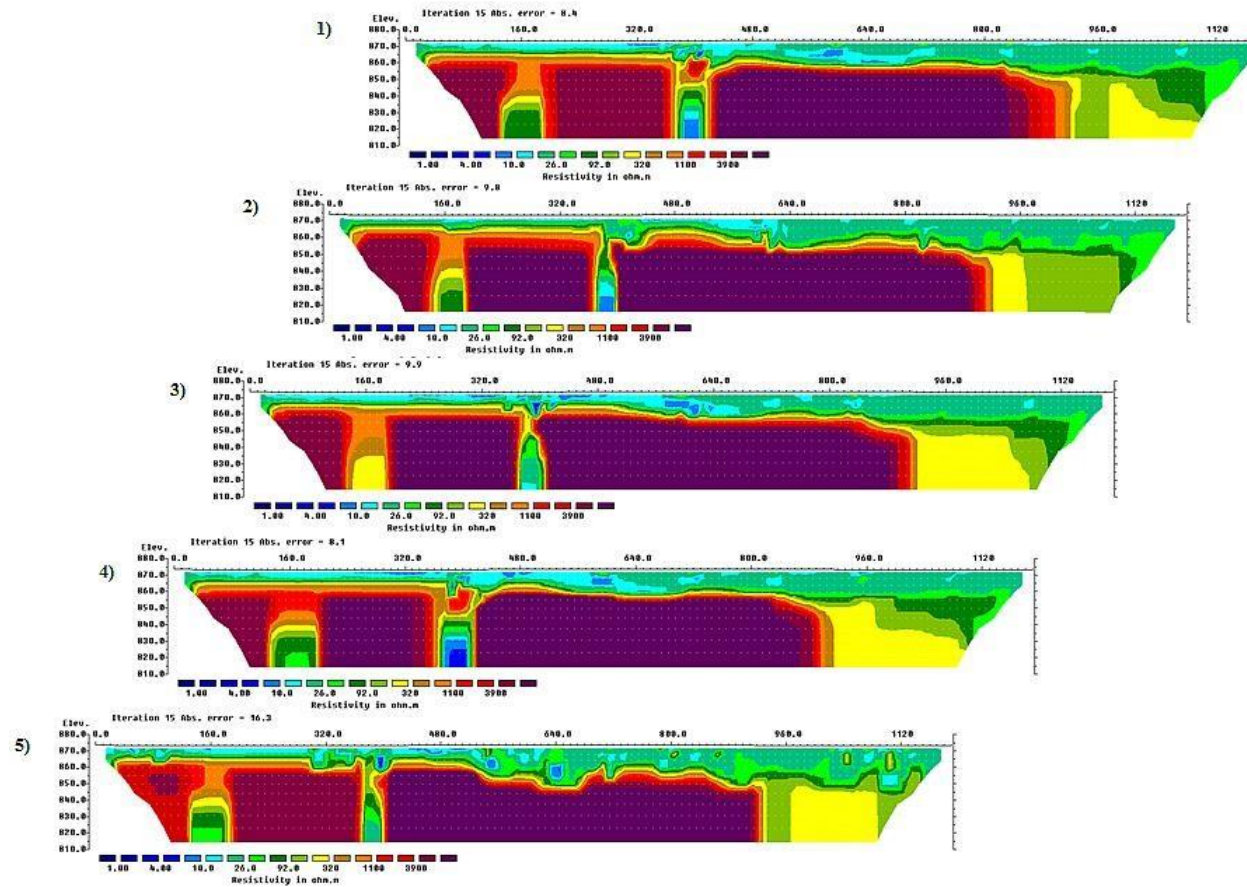


Figure showing independent time-lapse inverse models of the resistivity datasets acquired from October 2016 to October 2017. From these inversions, the changes in the subsurface resistivity values are determined by comparing the inversion model of an initial dataset and the subsequent datasets. Each inversion attempts to minimize the difference between the observed and calculated apparent resistivity values for each data set without taking into account the resistivity model obtained from the initial data set or a priori information. No significant changes are observed between the five datasets.